Analysis and Modeling of Force Sensing in Robotic Assisted Orthopedic Surgery

QI, Lin

A Thesis Submitted in Partial Fulfillment
of the Requirements for the Degree of
Doctor of Philosophy
in
Electronic Engineering

The Chinese University of Hong Kong
August 2013

Thesis/Assessment Committee

Professor Yung Pun To (Chair)

Professor Meng Qing Hu (Thesis Supervisor)

Professor Liu Yun-hui (Committee Member)

Professor Sun Dong (External Examiner)

論文評審委員會

榮本道 教授(主席)

孟慶虎 教授 (論文導師)

劉雲輝 教授 (委員)

孫東 教授 (校外委員)

ABSTRACT

In the past two decades, computer aided techniques and surgical robots are being widely used in different types of medical applications with accurate visualization, highly precise operation, minimal invasion and low radioactive damage to patients and surgeons. Therefore, computer aided and robotic assisted surgical system form a hot research topic for exploration.

In this research, for orthopedic surgical process, we proposed to set up and develop an integrate solution consisting of a navigation system and a robotic arm with hands-on capabilities. This system will assist the surgeon in the orthopedic surgery, with intramedullary nailing, bone milling and joint replacement operations among others.

In this system, Stäubli TX60, designed for use in super-clean environment, was adopted as the assistive robotic arm. We derived the kinematics and inverse kinematics of this robot for real-time control. The robot with surgical tool mounted can be considered as a smart tool that extends surgeon's ability to implement the surgery in cooperative mode with surgeon. In the cooperative control law, the concept of virtual fixture was used to refer to a task dependent aid that guides the user's motion along desired directions while preventing motion in undesired directions or regions of the workspace. This will reduce the tremor and mental load of the user, and increase the quality of the surgical task. When completing this type of task, in which robot works under the admittance mode, the instant velocity of the robot end-effector needs to be calculated in real-time. To comprise real-time capacity and reduce the effect when movement of robot arm encounters the singularity, singularity separation damped reciprocal (SSDR) algorithm is applied as to give better result than that of traditional damped least square (DLS) algorithm.

When drilling bone during orthopedic surgery, the force sensing between drill bit and bone is significant, by which surgeon can decide the depth of penetration into different tissue layers. In our system, ATI force/torque sensor was mounted on the end-effector of the robot arm. When drilling the bone, the force and torque signals were recorded. Applying the real-time wavelet transform, the break-through of different layers could be detected. *In vitro* porcine femur experiment, we tested different surgical drill bits with different parameters and shapes. Finite element simulation and analysis were introduced to evaluate the design of surgical tool and intra-operative bi-

ohazard. In previous finite element simulation research, the bone was considered as elastic material under tiny deformation, by which the simulation was a static deformation process. However, for drilling and other machining processes, the bone shows elasto-plastic characteristics against the elastic model for the static process. Using finite element method, simulation of bone drilling process could predict the biomechanical performance on the bone surface and different drill bits. The bone biomechanical parameters for elastic model consist of Young's modulus, Poisson's ratio, and thermal conductivity. For plastic model, the flow stress curve describes the biomechanics of the compact bone. In the simulation, the elasto-plastic curve of the bone was divided into elastic and plastic region according to the strain range. The stress distribution was calculated and displayed on the 3D model. To verify the results of FEA, drilling force and mean stress distribution were evaluated. *In vitro* experiment, force signal of drilling on fresh porcine femur was recorded for comparison with the results of FEA. The magnitude and variation tendency of drilling force from the FEA are in accordance with those of experimental results. The novel 3D dynamic visualization of drilling process could assist the surgeon by providing visual force feedback and prediction for the surgery process.

論文摘要

本論文提出一種開放式機器人輔助骨外科整形手術系統，該系統由工業機器人臂、光學定位系統、力反饋設備、力學傳感器和手術器械構成，籍此能夠為外科手術醫生提供直觀的視覺效果和手術器械追蹤，機器人臂的引入能夠極大提高手術操作的精度和減輕醫生的體力。傳統的外科手術如鑽骨植入、磨骨等操作完全需要醫生的手工操作，這增加了醫生的體力同時也降低了操作的精度，為改進傳統手術的缺點，本系統引入一種“協作式控制模式”，手術器械通過力學傳感器裝載在機器人執行器末端，由醫生操作手術器械，機器人通過力學傳感器感知醫生的操作意圖以便智能地輔助醫生精準地完成事先規劃好的的手術計畫。“虛擬夾具”的概念被應用於协作式控制模式，“虛擬夾具”是通過將醫生操作意圖投影到規劃好的手術路徑空間，一方面保證機器人按照醫生的意圖完成手術操作，另一方面減少由於醫生手抖產生的誤差。在本文中提出了一種利用力反饋設備仿真“虛擬夾具”的控制算法來驗證“虛擬夾具”的有效性。

在骨外科手術，如髖關節置換，植入髓內釘等中，鑽骨打孔是一種重要的操作。醫生往往通過感覺骨鑽的反作用力來感知鑽孔的過程，為了防止鑽頭穿透骨壁損傷軟組織，在本論文中一種基於實時小波變換的信號處理算法用來預測鑽頭穿透骨壁的時刻並控制機器人停機。

論文最後實現一種基於有限元素方法來仿真三維鑽頭打骨鑽孔過程，以往的有限元素方法往往研究骨模型的小形變靜態過程，骨模型被認為是線性的彈性材料，其生物力學的本征方程由楊氏模量和泊松率來描述。而在鑽骨打孔過程中，骨頭的形變是一種大形變過程，骨頭產生局部破裂和骨質分離，在鑽頭進給過程中骨切屑產生，骨頭的生物力學表現為非線性的塑性特徵，其生物力學的本征方程由流應力、應變和應變率來描述。本研究在有限元素建模中比較了塑性和彈-塑性兩種生物力學模型，應用麻花鑽頭和空心鑽頭兩種手术工具，給出了鑽骨過程中骨模型上應力的動態分佈，得出了兩種鑽頭鑽孔時反作用力隨時間的變化曲線。兩種真實的骨科鑽頭分別在豬股骨上進行鑽孔操作，測量的鑽孔反作用力的變化和幅值與有限元素仿真給出的結果具有很強的一致性。

CONTENTS

ABSTRACT ..... **I**

論文摘要 ..... **III**

CONTENTS ..... **V**

LIST OF TABLES ..... **VII**

LIST OF FIGURES ..... **IX**

LIST OF SYMBOLS AND ABBREVIATIONS ..... **XIII**

ACKNOWLEDGEMENTS ..... **XV**

DEDICATION ..... **XVI**

CHAPTER 1. INTRODUCTION 17
1.1 Motivation 17
1.2 Technique Challenges 20
1.3 Contributions in this Dissertation 20
1.4 Dissertation Organization 20
CHAPTER 2. BACKGROUND AND RESEARCH SURVEY 23
2.1 Overview of CAOS (Computer Assisted Orthopedics Surgery) 23
2.2 Overview of RAS (Robot Assisted System) 25
2.2.1 Classification of RAS 25
2.3 Previous Works 29
2.3.1 Passive Systems 30
2.3.2 Active Systems 31
2.3.3 Interactive Systems 34
2.3.4 Tele-operative Systems 37
CHAPTER 3. SYSTEM ARCHITECTURE 41
3.1 The Integrated System 41
3.1.1 Robot Control System 41
3.1.2 Optical Tracking System 42
3.1.3 Navigation System 43
3.1.4 Tele-operation and Haptic Control System 44
3.2 Motion Analysis of Surgical Robot 46
3.2.1 Forward Kinematics of TX60 47
3.2.2 Singularity Analysis 49
3.2.3 Damped Least Squares (DLS): 54
3.2.4 Singularity Separation Damped Reciprocal (SSDR): 57
3.2.5 Error Analysis 60
CHAPTER 4. COOPERATIVE CONTROL ALGORITHM DESIGN 67
4.1 Introduction 67
4.2 Mathematic Description of Virtual Fixtures 68
4.2.1 Virtual Fixture Control Law 68
4.2.2 Guidance Virtual Fixture (GVF) 69
4.2.3 Guidance Virtual Fixture Generation 71
4.3 Configuration of Simulation for GVF 71
4.3.1 Haptic Interface 71
4.3.2 Virtual Robot Modeling 72
4.3.3 Force Feedback with GVF 74
4.4 Results and Discussion on Simulation 74
4.4.1 Case 1: Move along a Line (One DoF) 75
4.4.2 Case 2: Move in Plane (Two DoF) 76
CHAPTER 5. FORCE SENSING AND FINITE ELEMENT ANALYSIS FOR BONE DRILLING PROCESS 79
5.1 Introduction 79
5.2 Force Profile of Bone Drilling 79

5.3 Force Sensing Experiment 84
5.4 Wavelet-based Real-time Detection of Drill Bit Break-through 84
5.4.1.1 Wavelet Transform 85
5.4.1.2 Real-time Wavelet Transform 88
5.4.1.3 Modulus Maxima of Wavelet coefficients 90
5.4.1.4 Break-through Detection Algorithm 92
5.4.1.5 Result and Discussion 93
5.5 3D Finite Element Analysis of Drilling Bone in Relation to Orthopedic Surgery 96
5.5.1 Motivation 96
5.5.2 Methods and Material 97
5.5.3 Results and Discussion 111
CHAPTER 6. CONCLUSION AND FUTURE WORK 122

APPENDICES 124

A. INVERSE KINEMATICS OF STÄUBLI TX60 ROBOT 124
Singularity Cases through Inverse Kinematics Solution 126
B. FORCE GUIDANCE 127
B.1 Type 1: Force Guidance in Base Frame 127
B.2 Type 2: Force Guidance in Sensor Frame 127

REFERENCES 130

LIST OF TABLES

This is the list of tables in the thesis.

Table 1–1. Comparison between traditional surgery versus computer and robot assisted surgery.....18

Table 2–1. Selected robotic projects according to the clinical area[1]. 28

Table 3–1.Modified DH parameters of TX60 47

Table 4–1. MDH parameters of TX60.....72

Table 5–1.Time delays of wavelet coefficients at different scales 89

Table 5–2. Elastic and thermal parameters of drill bit and human femur cortical bone. 102

Table 5–3. List of mechanical property of human, equine, bovine, and porcine femur cortical bone. . 109

LIST OF FIGURES

This is the list of figures in the thesis.

Figure 1.1 Orthopedic surgical robot arm developed at the Chinese University of Hong Kong. 19

Figure 2.1 CAOS system: (a) System platform, computer and localizer camera[9]. (b) Related orientation and position between camera, surgical tool and anatomy coordinates system[10].(c) Point-cloud registration for knee joint implants. (d) Tracker is attached to the surgical tool, with position shown real time on the monitor[9]. 24

Figure 2.2 Architecture of a surgical CAD/CAM system [11]. 25

Figure 2.3. Active robot executes the process while surgeon observes or supervises [3]. 26

Figure 2.4. Interactive robot shares control with surgeon [3]. 26

Figure 2.5. Tele-operated robot system consists of master and slave parts. Surgeon controls the robot in real-time through the interface, such as haptic device or joy stick (as master). Robot (as slave) faithfully replicates the surgeon's motions with the interface. 27

Figure 2.6. iBlock as the bone-mounted guide. 30

Figure 2.7. BRIGIT as a mechanical support and guidance for cutting[40]. 31

Figure 2.8. Architecture of the RoboDoc system[43]. 31

Figure 2.9. The RoboDoc system for orthopedic surgery. (a) Registration and surgical plan on Orthodoc. (b) Close-up of robotic milling of femur[44]. 32

Figure 2.10. (a) Total knee replacement by CASPAR[47]. (b) Tunnel drilling[47]. 33

Figure 2.11. (a) Efficient work space through gauge based registration. (b) Pig femur experiment. 34

Figure 2.12. (a) Acrobot for knee surgery. (b).Manipulation of the hands-on robot [50]. 35

Figure 2.13.(a) RIO robotic arm interactive orthopedic system (b)Joint motion of the RIO robotic arm. (c) CT based patient specific pre-operative planning[52] (d) Total Hip Arthroplasty performed by RIO. 36

Figure 2.14. (a) Neuromate for brain biospys (courtesy of Renishaw plc). (b) Neuromate with force sensor for skull surgery[54]. 37

Figure 2.15. Zeus tele-surgery system[55] 38

Figure 2.16. Configuration of Zeus system for Lindbergh Operation[58] 38

Figure 2.17. The da Vinci system. (a) Console part. (b) Surgeon's view and intuitive tele-manipulator (c) three robotic arms (d) comparison of EndoWrist and human wrist[55]. 40

Figure 3.1. Scenario of the CAOS system in operating room. (1) Robot control system. (2) Optical tracking system. (3) Navigation system. (4) Tele-operation and haptic control system. In addition, there are C-arm and other necessary devices in the operating room. 41

Figure 3.2. Architecture of proposed robot assisted surgery system. 45

Figure 3.3. (a) Six main parts of the robot arm are: the base (A), the shoulder (B), the arm (C), the elbow (D), the forearm (E) and the wrist (F). (b) Dimension of each part of the robot arm. 46

Figure 3.4. The modified Denavit-Hartenberg notation for link i-1 and link i [76]. 46

Figure 3.5. Mappings among different kinematic space. 49

Figure 3.6. Wrist frame of TX60 50

Figure 3.7. Boundary singularity case. 52

Figure 3.8. Interior singularity case. 53

Figure 3.9.Error comparison of DLS and SSDR method by translation along Y axis at 0.25 m/s. 63

Figure 3.10.Cartesian velocity and joint velocity of robot arm of DLS ((a) and (c)) and SSDR ((b) and (d)) methods with translation along Y axis at 0.25 m/s. 64

Figure 3.11. Error comparison of DLS and SSDR methods by rotation along X axis at 0.25 rad/s. 65

Figure 3.12.Cartesian velocity and joint velocity of robot arm of DLS((a) and (c)) and SSDR((b) and (d)) methods with rotation along X axis at 0.25 rad/s. 66

Figure 4.1. Demonstration of the human-machine collaborative system, 3 links robot is equipped with force/torque sensor which can be applied force and torque by user, the curve is the desired trajectory and T_{tar} is the target. 67

Figure 4.2. Haptic interface with robot model based on the Robotic Toolbox under MATLAB®. 71

Figure 4.3. (a): MATLAB graphics coordinate. (b):Phantom Desktop coordinate 73

Figure 4.4. Flow chart of programming the haptic interface with the MATLAB®. 74

Figure 4.5. (a) X, Y and Z position of end-effector in Cartesian space. (b) Position error compared with and without GVF 76

Figure 4.6.(a)X, Y and Z position of end-effector in Cartesian space. (b) Position error compared with and without GVF. 77

Figure 4.7. End-effector trajectory. Blue line is the ideal path; red circle is the movement without GVF, green line is the path applied GVF. 78

Figure 5.1. Femur shaft and slices. The interior of a typical long bone showing the growing proximal end with a growth plate and a distal end with the epiphysis fused to the metaphysis[95]. 80

Figure 5.2. (a) Twist drill geometry (b) Drilling process of twist drill bit in single material layer. 81

Figure 5.3. Process of drilling through a porcine femoral shaft. Stage 1 is drilling through the front cortical wall. Stage 2 is penetration into the yellow marrow. Stage 3 is drilling through the back cortical wall. 82

Figure 5.4. Profile of drilling force under different feed rate and fixed rotation speed. 83

Figure 5.5. Force sensing experiment setup based on the robotic assisted orthopedic surgery system. . 84

Figure 5.6. Mallat pyramid decomposition algorithm 87

Figure 5.7. Signal and signal decomposition. S is the original signal. a_j and d_j are approximation and detail of the signal at the $j\text{th}$ level. 88

Figure 5.8. Block diagram of real-time K-tap FIR filter. Previous N input samples and output sample are in stored. 88

Figure 5.9. Time delays of wavelet coefficients at different scales. (a) Original drilling force through two layers of porcine femur at v_f =12.5mm/s and w =600 rpm (b) Wavelet coefficients at scale = 2^1, (c) Wavelet coefficients at scale= 2^3, (d) Wavelet coefficients at scale= 2^5. Blue solid line is the real-time computation value. Red dash line is the theoretical value. 'Haar' wavelet was chosen. 89

Figure 5.10. Different types of singularities and modulus maxima with 'db2' wavelet at scales 2^1 and 2^2. Minima, maxima and zero-crossing indicate the 'step type' signal. 91

Figure 5.11. Different types of singularities and modulus maxima with 'haar' wavelet at scales 2^1 and 2^2. Minima, maxima and zero-crossing indicate the pulse type signal. 91

Figure 5.12. (a) $f(t)$ is force signal. (b) to (f) Blue solid lines are wavelet coefficients at different scales, red dash lines are the modulus maxima at different scales. 93

Figure 5.13. (a). Normalized force signal with found threshold position. The final PTh indicates the break-through point of back cortical wall. (b). Comparison of break-through stop and complete penetration on porcine femur. 94

Figure 5.14. Normal stress and shear stress on tetrahedral element of solid object. $F_1,\cdots,F_n$ are external forces on surface S_F, $U_1,\cdots,U_n$ are deformation velocity on surface S_U. dS and S are the internal surfaces. n is the normal vector on surface of S. V is the volume of solid object. 98

Figure 5.15. Solving process of finite element method 100

Figure 5.16. Strain-strain curve for a cortical bone sample in tension 101

Figure 5.17. Tensile stress(σ)–strain(ε) curves for human femoral cortical bone as a function of strain rate($\dot{\varepsilon}$)(reprinted from [123]). 102

Figure 5.18. Fitted curve and the reported experimental data in plastic region. Solid lines are fitted curve, dot lines are experimental data from[123]. 103

Figure 5.19. Stress-strain curves of rigid, elastic, plastic and elasto-plastic material in DEFORM-3D™. 104

Figure 5.20. (a) and (b) are hollow bit and twist bit. (c) and (d) are CAD models in SolidWorks®..... 105

Figure.21. Mechanism of orthogonal cutting. (a) is isotropic view and (b) is side view. Region 1 and 2 are the primary and second shear zone[129]. 106

Figure 5.22. Geometry model of porcine femur for plastic object as hollow cylinder. 106

Figure 5.23. Simplified femur bone as hollow cylinder with side view and isotropic view: length = 20mm, inner diameter = 7 mm, outer diameter = 10 mm, thickness = 2 mm. 107

Figure 5.24. Geometry model of femur bone for elasto-plastic object as thin cylinder..... 107

Figure 5.25. Bone is modeled as hollow cylinder with plastic material. (a) and (b) show the movement of twist- and hollow-bit tip and boundary configuration on distal end of bone model. 108

Figure 5.26. Bone is modeled as piece of cylinder with plastic material. (a) and (b) show the movement of twist- and hollow-bit and boundary configuration on circle edge of bone model. 108

Figure 5.27. Experiment setup for drilling porcine femur. 110

Figure 5.28. Chip generation and stress distribution of twist-bit tip drilling simulation from FEA. The feed rate is 12.5 mm/s and rotation speed is 600 rpm. 112

Figure 5.29. Comparison of recorded drilling force and FEA result with feed rate = 12.5 mm/s, rotation speed = 600 rpm. 114

Figure 5.30. Comparison of recorded drilling force and FEA result with feed rate = 1.25 mm/s, rotation speed = 600 rpm. 115

Figure 5.31. Chip generation and stress distribution of hollow-bit tip drilling in FEA with feed rate = 1.25 mm/s and rotation speed = 600 rpm. 116

Figure 5.32. Comparison of measured force and FEA result, feed rate = 12.5 mm/s, rotation speed = 600 rpm. 117

Figure 5.33. Chip generation and stress distribution of twist-bit tip drilling simulation from FEA with feed rate = 12.5 mm/s and rotation speed = 600 rpm. 119

Figure 5.34. Drilling force on twist-bit tip along Z axis from FEA. 119

Figure 5.35. Chip generation and stress distribution of hollow-bit tip drilling simulation from FEA with feed rate = 12.5 mm/s and rotation speed = 600 rpm. 121

Figure 5.36. Drilling force on hollow-bit tip along Z axis from FEA. 121

LIST OF SYMBOLS AND ABBREVIATIONS

2D	Two Dimension
3D	Three Dimension
CAD	Computer-aided Design
CAM	Computer-aided Manufacturing
CAOS	Computer Assisted Orthopedics Surgery
CAS	Computer Assisted Surgery
CWT	Continuous Wavelet Transform
CT	Computer Tomography
DLS	Damped Least Squares
DoF	Degree of Freedom
DSP	Digital Signal Processing
DWT	Discrete Wavelet Transform
FE	Finite Element
FEA	Finite Element Analysis
FEM	Finite Element Modeling
IGT	Image-guided Therapy
GVF	Guidance Virtual Fixture
MRI	Magnetic Resonance Imaging
OR	Operating Room
RAS	Robot Assisted System
SVD	Singular Value Decomposition
WT	Wavelet Transform

ACKNOWLEDGEMENTS

I offer my enduring gratitude to the faculty of the committee, staff at EE department, who have inspired me to continue my work in this field. I owe particular thanks to Prof. Meng Qing-Hu.Max, without his long-term support and encouragement, I cannot go forward during these years. Prof. Meng acts as not only the research supervisor but a spiritual guidance for my life.

I also thank Wang JiaoLe, Jimmy Chen, Dr. Wang XiaoNa, and Dr.Ren HongLiang for their academic suggestion and technical support. I am very grateful for Mr.Lok's and Mr. Liang YongPei's help for experimental instrument support.

Special thanks are owed to my parents, who have supported me throughout my years of education with the most patience.

DEDICATION

This is the Dedication.

Chapter 1. Introduction

1.1 Motivation

For the prime principles of ethics in medicine and providing the best health care to the patient, the dictum “Primum non nocere” (First, do no harm) and the dictum “Primum Succurrere” (First, hasten to help) indicate two cross development of practicing medicine. More multidisciplinary technologies are applied in the medicine area.

Computer Assisted Surgery (CAS) is the first combination of computer technology and medicine, applied for pre-operative planning, surgery guiding and conducting surgical interventions. CAS involves any computer-based technologies, such as 3D imaging, real-time sensing in the planning, execution and follow-up of surgical process, therefore it is known as image-guided surgery, surgical navigation and 3D computer surgery. CAS provides the surgeon with better visualization and targeting of sites as well as improved diagnostic and treatment capabilities. With over 100,000 successfully performed operations, CAS is believed as a significant step over traditional techniques on medicine.

In the early development of robots, most of the robotic technologies have been widely used in industrial manufacturing. Among these applications, the robotic systems work autonomously and are designed to replace human by implementing the difficult and complex tasks with high power output, accuracy and repeatability. Because robot has advanced mechanical performance, the concept of Robot Assisted Surgery (RAS) has been introduced in the medical area during the recent two decades. RAS requires specific surgical robot, which may be adopted from the industrial robot or specific developed robot. During the surgery process, not only does the robot act as a computerized system with a motorized construction capable of interacting with the environment but also as the dexterous extension of the surgeon. In the most common form, the surgical robots are equipped with multi-modal sensors, which provide dynamic information on the instantaneous status of robot, patient and operating room. The central control parts process all the information so that the next surgery action can be determined.

As the report of Medical Robotics Database (MERODA) in 2009[1], there are 456 ongoing medical robotic projects among different institutes and companies around the world. Some have been widely used for the commercial and clinical appli-

cation, some are still the under the development. Those medical robots are designed for various applications, such as disease diagnosis, surgery and rehabilitation in most medical area.

From clinical doctor's experience and engineer's viewpoints, Table 1–1 lists the advantages and disadvantages of traditional surgery versus computer and robot assisted surgery [2-4].

Table 1–1. Comparison between traditional surgery versus computer and robot assisted surgery

	Traditional surgery by human	Computer and Robot Assisted surgery
Advantages	Experienced surgeon's judgment Excellent trained hand-eye coordination High dexterity at natural human scale Easily to integrate and act on multiple information sources Easily trained Ubiquitous and Affordable	3D visualization from CT and MRI Minimal invasion Excellent geometric accuracy Improved dexterity and stability High degrees of freedom Able to scale different motions Elimination of physiologic tremors Resistant to radiation and Infection Operate surgical tools at different payload Integrate multiple sources of numerical and sensor data Tele-surgery for distant districts Ergonomic position
Disadvantages	Fatigue and inattention in long surgery Limited degrees of motion and compromised dexterity outside natural human's scale Loss of 3D visualization and insight in patient's body	Limited hand-eye coordination Lack of artificial intelligence Limited touch and haptic sensation High cost for patients Require surgeon more technologies

	Amplification of physiologic tremors Hard to keep sterile Exposed to the radiation	Hard to setup the system

For improving the performance of the Computer Assisted Surgery for orthopedics, a primitive robotic arm was developed at the Department of Orthopedics &Traumatology, the Chinese University of Hong Kong. The robotic arm (Figure 1.1) is a passive robotic arm without joint motors, fully under the manipulation by surgeon. The robotic system was featured with simple but versatile design, six DoF movements and instant locking system by either pedal control or hand switch. The robot arm uses stainless steel as housing material for ease of sterilization. Exchangeable optical trackers are mounted on end-effector for different navigation systems. The secured electrical and mechanical safety measurement are designed for critical surgical requirements[5].

Figure 1.1 Orthopedic surgical robot arm developed at the Chinese University of Hong Kong.

However, this robotic arm only serves surgical interns in the orthopedic surgery. Because it has no actuator, surgeon has to manually adjust joint by joint when moving the robotic arm position. During the surgical process, it simply assists the

surgeon to hold the surgical tool, typically bone drilling, and acts as the guidance support.

1.2 Technique Challenges

Bone drilling, milling and sawing are important processes during the orthopedic surgery. In traditional orthopedic surgery, these operations are conducted by surgeons under the fluoroscopy images, which cost surgeon long operation time and body energy without promising accurate positioning.

The minimally invasive penetrating way to get access to the target location can be through soft tissue, bony structure and the most critical issues are:

- Risk of damage to critical tissue, especially the nerves and blood vessel.
- limitation of human dexterity
- Surgeon fatigue.

On those considerations, we intend to develop an interactive robotic assisted system for orthopedic surgery with cooperative control and motion constraint algorithms based on force feedback.

1.3 Contributions in this Dissertation

As original work approached, we setup a platform including industrial robot, optical tracking device, navigation system and force sensing device for orthopedic surgery.

Cooperative control algorithm is proposed based on virtual fixture concept, which can guide the operator to move along the desired paths while preventing the motion in undesired directions/regions of the working space.

An algorithm, based on wavelet transform for predicting drill bit breakthrough while drilling bone, is proposed and tested with *in vitro* experiment.

3D simulation of drilling bone process with various surgical tools using finite element modeling and analysis is implemented. Finite element method provides a versatile way for surgical tool design and surgery process analysis. The simulation give the visualization of drilling process and mechanical performance of the bone. The FEA results are compared with *in vitro* experimental test.

1.4 Dissertation Organization

This dissertation is divided into six chapters. The brief contents of each chapter are below:

- Chapter 1: Introduction

Introduction to background and motivation about this research and approaches.

- Chapter 2: Research Survey

  Description on the basic concept and process of the computer and robot assisted orthopedic surgery. Survey and discussion on the classification and development of the robot assisted surgery.

- Chapter 3: System Architecture

  Overview of the architecture of the robot assisted surgery system, including the system operating process, hardware and software architecture. The singularities of robotic movement and inverse Jacobian kinematics are discussed.

- Chapter 4: Cooperative Control Algorithm Design

  Simulations for cooperative control algorithm based on haptic assisted system, which is conducted to study the kinematics and trajectory of the robot, which takes response to the manipulation command of the operator.

- Chapter 5: Force Sensing and Finite Element Analysis For Drilling Bone Process

  Discussion on features of force information while drilling femur bone. Wavelet based drill bit break-through algorithm is proposed. Simulation of drilling bone process based on finite element method with various surgical tools is implemented and compared with *in vitro* experiment.

- Chapter 6: Conclusion and Future Work

  Conclusion and comment on this research work and address the possible future work.

Chapter 2. Background and Research Survey

2.1 Overview of CAOS (Computer Assisted Orthopedics Surgery)

In the broad sense, orthopedic practice can be grouped according to the joints and bones into: upper limb (shoulder, elbow, and wrist), spine (neck and back), pelvis and hip, knee, and foot and ankle. From the views of orthopedic surgeons, clinical conditions consist of congenital disorders (e.g. scoliosis), the various arthritis, bone and soft tissue cancers, and trauma[6].

In practice of orthopedic surgery, it can be classified according to the types of processes commonly performed. On February 2007, MedTechInsight Consulting Group analyzed the 32.7 million processes implemented in all surgical specialties in the United State, 2006. They categorized the subset of orthopedic processes into five main groups[7]:

- Fracture repair (generally due to trauma)
- Total joint arthroplasty (knee and hip)
- Spine surgery
- Disc replacement (discectomy, laminectomy, spinal fusion, and vertebroplasty)
- Arthroscopy (knee, shoulder, and wrist)

Generally, the main procedures during CAOS can be divided into three steps[8]:

1. Data Acquisition: Before the surgery, patient's anatomy information can be acquired in three different ways, fluoroscopic, guided by CT or magnetic resonance imaging (MRI), or imageless systems. These data are then used for registration and tracking
2. Registration: Registration refers to the ability of binding multimodal images (e.g. X-rays, CT, MRI and patients' 3D anatomy images) with the anatomical position in the surgical field. Registration techniques may require the placement of pins or "fiducial markers" in the target bone. A surface-matching technique is used to map the shapes of the bone surface model generated from pre-operative images to surface data points collected during surgery(Figure 2.1 (b) and (c)).
3. Tracking: Tracking refers to that the sensors and measurement devices can provide the relevant orientation and position of tools to surgical objects during surgery (Figure 2.1 (d)).

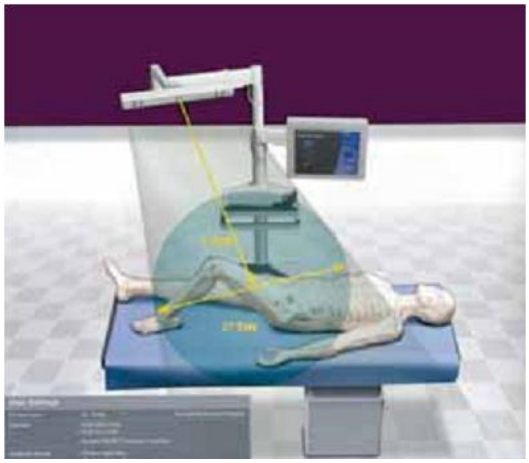

(a)

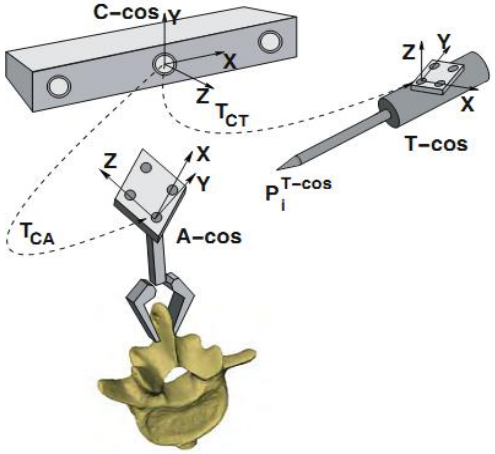

(b)

(c)

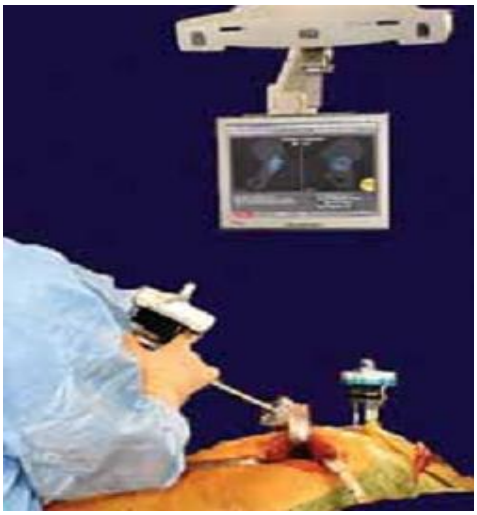

(d)

Figure 2.1 CAOS system: (a) System platform, computer and localizer camera[9]. (b) Related orientation and position between camera, surgical tool and anatomy coordinates system[10].(c) Point-cloud registration for knee joint implants. (d) Tracker is attached to the surgical tool, with position shown real-time on the monitor[9].

From the views of engineering, Kazanzides,et al [11], [12, 13] classify the CAS into four closed-loop processes with analogy to the concept of Computer Assisted Design/ Manufacture (CAD/CAM):

1. Constructing a patient-specific model and interventional surgical plan. (Pre-operative)
2. Registering the model and plan with the patient. (Intra-operative)
3. Using multiple technologies to assist for implementing the surgical plan. (Intra-operative)

4. Assessing the result. (Post-operative)

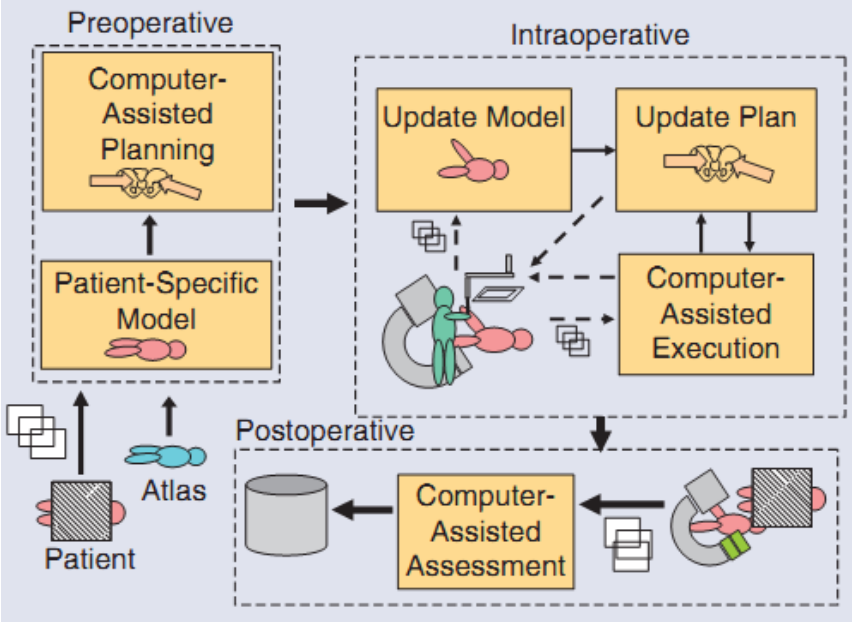

Figure 2.2 Architecture of a surgical CAD/CAM system [11].

2.2 Overview of RAS (Robot Assisted System)

As the pioneer of robotics in surgery, Lanfranco,et al [4], [14] perform the guidance of neurosurgical biopsy with greater precision using the 6-axis industrial robot arm Puma 560 to replace the stereotactic frame in 1985. Later in 1988, Davies [15] implemented a transurethral resection of the prostate using the Puma 560. This project finally was led to a well-developed RAS called PROBOT, which is designed specifically for transurethral resection of the prostate. Their works bridged the gap between robot and medicine, bringing about the rapid development of the RAS.

2.2.1 Classification of RAS

Surgical robots can be categorized based on their different roles in the operating room (OR) [16].

- Passive robots only serve as a tool holder once directed to the target position or provide the information to the surgeon.
- Active robots perform the operation under the control of its computer program. (E.g. in compliant mode). Surgeons almost plan the surgery procedure, download the surgery control program to the controller and observe the whole execution conducted by robot autonomously. Surgeon, on the side of robot, will stop the robotic system, if surgery plan is required to revise or emergency occurs (Figure 2.3).

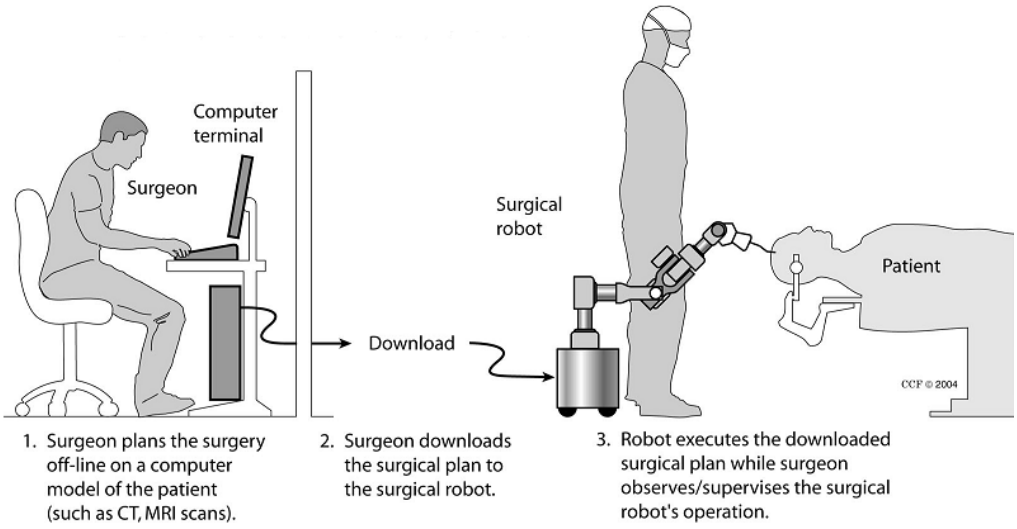

Figure 2.3. Active robot executes the process while surgeon observes or supervises [3].

- Interactive (or semi-active) robots are under computer control and act as mechanical guides through direct cooperation with human.

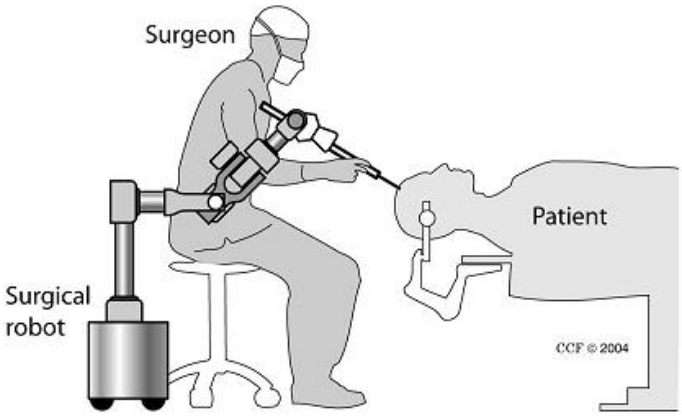

Figure 2.4. Interactive robot shares control with surgeon [3].

- Tele-operative robots perform remote interventions or haptic feedback with surgeon on other sites. In tele-operative systems, with an online input/output device that is a typical force feedback device (called master), the surgeon performs the surgical manipulations, and the surgical robot (called slave) precisely follows the motions of the surgeon through input device. Meanwhile, the surgeon can be informed the surgery information feedback from the various sensors mounted on robot's end or surgical tools. In tele-operative system, the robotic system is considered as the extension of the surgeon's hand and sense.

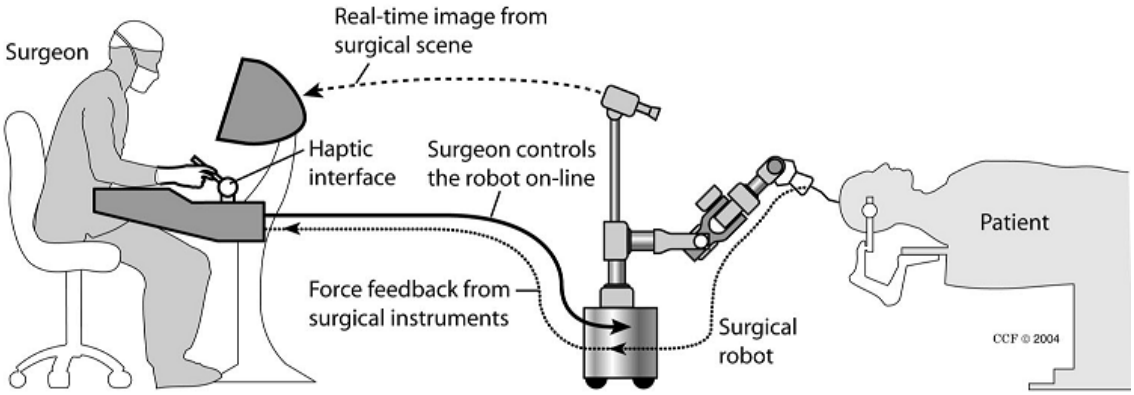

Figure 2.5. Tele-operated robot system consists of master and slave parts. Surgeon controls the robot in real-time through the interface, such as haptic device or joy stick (as master). Robot (as slave) faithfully replicates the surgeon's motions with the interface.

According to the different roles of the robots during the surgery process, Taylor,et al [17] categorize the robots, by which surgeon can work cooperatively to surgical intervention , as:

- Intern replacements: The robot performs the role of assistant to surgeon in the most surgical tasks instead of surgical interns and other people whose main job is to help the surgeon.
- Tele-surgery systems: The robot's motions are directed by the surgeon by means of a joy-stick, haptic device, or similar device from the remote districts, which is always called master-slave system. The robot acts as an extension of surgeon's hands with direct manipulation capabilities. With such systems, it is possible for surgeon to access difficult reach parts of the body and to perform delicate microsurgical tasks without tremor.
- Navigation aids: The objective of navigation is to provide the surgeon with accurately relative position between the location of surgical instruments and the patient's anatomy. These systems typically consist of a 3D localizing device such as an instrumented passive manipulator, ultrasound detector and 3D optical tracker, together with a computer graphic workstation for displaying position relative to volumetric medical images.
- Position aids: The robot can support and guide a surgical tool along the desired path and orientation relative to the target anatomy. For safety considerations, the robot is often shut down during the actual instrument insertion. Although this re-

duces the chance of unwanted motion at critical region, it does not address more crucial issue of mis-registration.

- Path following systems: The robot is moved along a planned path to complete specific tasks, such as a precise neurosurgery using the robot to insert the needle. In other case, the robot control system keeps the surgeon's operation from the critical surgical area.

Clinical doctor prefers to classify the robots through clinical applications[18, 19]. A list of several clinical areas and the specific robotic projects applied is shown in Table 2–1.

Table 2–1. Selected robotic projects according to the clinical area[1].

Clinical Area	Name	Development team	Institute/company	Functions of the system
Neurosurgery	NEUROMATE[20]	Renishaw, Inc.	Renishaw, Inc.	Guidance of a drill sleeve, 6-DoF articulated arm for industrial deployment
Neurosurgery	PATHFINDER[21]	Armstrong Healthcare Ltd	Armstrong Healthcare Ltd.	Move tools according to a pre-operatively defined trajectory, based on a serial articulated kinematics
Orthopedics	ROBODOC[22]	Curexo Technology Corp.	Curexo Technology Corp.	milling of the implant bed for hip arthroplasty based on 5-axis -SCARA for industrial deployment
Orthopedics	CASPAR[23]	OrtoMaquet	URS GmbH.	Milling of the implant bed for hip and knee arthroplasty, cruciform ligament replacement
Orthopedics	Galileo[24]	Precsison Implants	Precision Impants AG.	Guidance of sawbladed gauges for knee arthroplasty
Orthopedics	Renaissance /SpineAssist[25]	Shoham, Kunicher	Technion-Israel Institute of Technology.	Carrier system for the positioning of a drill for spinal surgery
Orthopedics	WATO I/II[26]	Shi, Zhao	Institute of Image Processing & Pattern Recognition, Shanghai Jiao Tong University.	Total knee replacement surgery. The cutting of the bone is done by the robot according to the intra-operatively decided implant position
Orthopedics	RIO[27]	MAKO Surgical Systems.	MAKO Surgical Corp.	The HGS Haptic Guidance robotic system for the implantation of unicondylar knee pros-

				thesis
Ophthalmology	MICRON[28]	Riviere, Ang, Khosla	Robotics Institute, Carnegie Mellon.	Handheld tremor compensation for micro surgery
Ophthalmology	BioMicroRobot[29]	Nelson	Institute of Robotics and Intelligent Systems, ETH Zurich, CH.	Micro-scale device controlled by changing external magnet fields and can travel through the patients bod
General Surgery	ZEUS[30]	Intuitive Surgical Ltd.	Intuitive Surgical Ltd.	Laparoscopic interventions, tele-surgery, master-slave system
General Surgery	DaVinci[30]	Intuitive Surgical Ltd.	Intuitive Surgical Ltd.	The tele-surgical workstations consist of a cockpit unit with joysticks, imaging elements and a manipulator unit of which three arms control the instruments and the endoscopic camera.
Percutaneous	InnoMotion[31]	Innomedic GmbH.	Innomedic GmbH.	Biopsy robot arm designed to operate within a CT/MRI machine
Steerable Catheters	Sensei[32]	Hansen Medical.	Hansen Medical.	Tele-robotic system for catheter guidance during heart surgery
Radiotherapy	CyberKnife[33]	Accuray Inc.	Accuray Inc.	Tumor irradiation, automatic alignment of the beam, determination of the tumor's position in x-ray pictures
Radiotherapy	Novalis [34, 35]	Brainlab Inc.	Brainlab Inc.	Image-guided Stereotactic Body Radiotherapy including beam shaping and alignment.
Emergency Response	AutoPulse Plus[36]	Zoll Medical Corp.	Zoll Medical Corp.	Emergency cardiopulmonary resuscitation and the E Series monitor/defibrillator.
Rehabilitation	AutoAmbulator[37]	Healthsouth Inc.	Healthsouth Inc.	Balance the neuro-disease patient's weight and moves his/her lower limbs over the treadmill.
Rehabilitation	HAL[38]	Suzuki	Graduate School of Systems and information Engineering, University of Tsukuba.	Exoskeleton devices for lower-limb rehabilitation of paraplegic patients.

2.3 Previous Works

In this section, we will survey and describe the key technologies through some typical RAS based on their specific application and the degree of autonomy.

2.3.1 Passive Systems

iBlock

iBlock (Praxim Inc) is a compact automated cutting guide for total knee replacement. The robot is mounted directly to the bone, to position bone cutting guides in the appropriate planes surrounding the knee. Beyond the guiding function, the bond-mounted structure can prevent any relative motion between the robot and the bone (see Figure 2.6).

The robot architecture has 2 motorized degrees of freedom (DoF) whose axes of rotation are arranged in parallel and precisely aligned to the implant cutting planes with a 2 DoF adjustment mechanism[39].

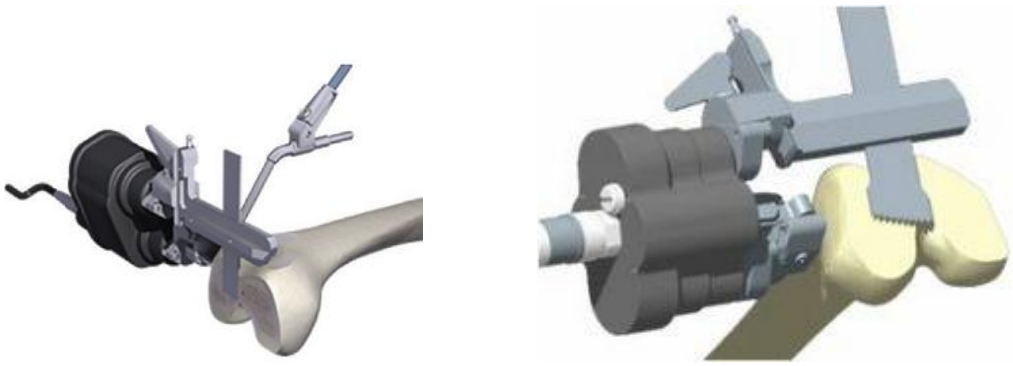

Figure 2.6. iBlock as the bone-mounted guide.

BRIGIT

The BRIGIT (Bone Resection Instrument Guidance by Intelligent Telemanipulator, developed by MedTech SA France), aims for easy installation and operation in osteotomies and TKR (Total Knee Replacement) surgery. This robot can be used as a positioner of a guide providing a mechanical support during bone sawing or drilling without pre-operative imaging or a navigation system (see Figure 2.7).

The planned position of the guide is obtained after a registration process which collects anatomical landmarks on the surface of the patient's bone. This can be done in a interactive mode, by grabbing the tool tip, through an appropriate force control, or in a tele-operated mode via a master device[40].

Figure 2.7. BRIGIT as a mechanical support and guidance for cutting[40].

2.3.2 Active Systems

RoboDoc

RoboDoc developed by Taylor and associates at IBM, was considered as the initial robot assistance for orthopedics[22]. This system, further commercialized for clinical application by Curexo Technology Corp, was first used in 1992 for total hip replacement (THR)[41]. RoboDoc has received a CE mark (1996), and FDA clearance for total hip replacement (1998) and total knee replacement (2009)[42]. RoboDoc consists of three main parts (see Figure 2.8):

- OrthoDoc: It is surgery planner software displayed on the monitor, with which the surgeon plans bone milling based on pre-operative CT images.
- A 5 DoF IBM SCARA robot: it does the cutting and milling operation.
- A Center Control Cabinet: It guides and controls the robot in real-time.

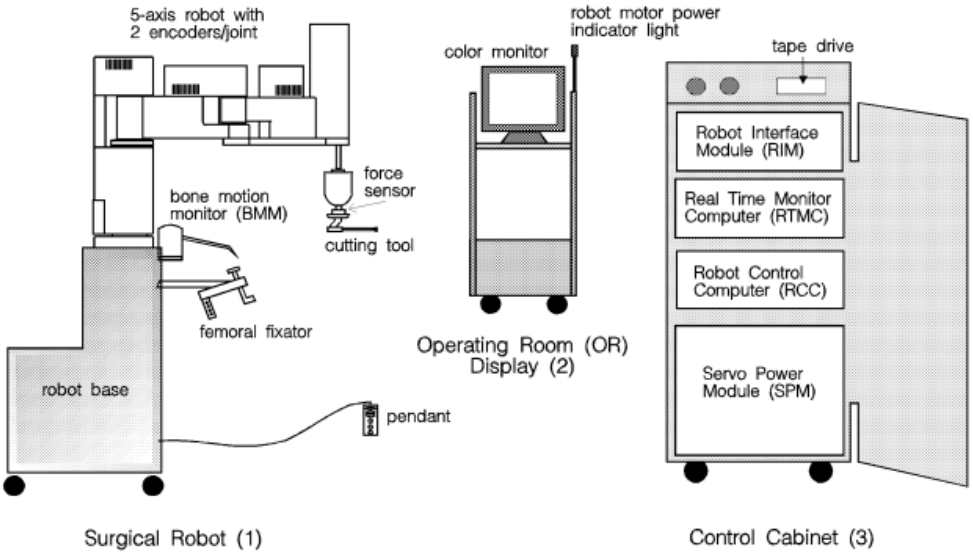

Figure 2.8. Architecture of the RoboDoc system[43].

Before using the RoboDoc surgical system, the surgeon is responsible for planning the surgery on the Orthodoc, importing pre-operative 3D image data from the CT scan on the patient. The surgeon then plans the optimal implant location and orientation (Figure 2.9 (a)).

In the beginning of surgery, patient's leg is clamped to the robot's pedestal. During the surgery, if the leg moves, a second clamp locating the femoral head was used to halt the robot automatically. The registration between the bone and the robot is implemented either by touching multiple points on the surface of the bone or by touching pre-implanted fiducial markers on the pre-operative CT images.

The robot is manually guided to an approximate initial position by surgeon using a 6-axis force sensor mounted at the robot's wrist. Then RoboDoc performs the milling or drilling operation automatically in compliance with the surgical plan (see Figure 2.9 (b)). The autonomous operation as the characteristic technology of RoboDoc, is designed for concerns with the doctor and patient's safety.

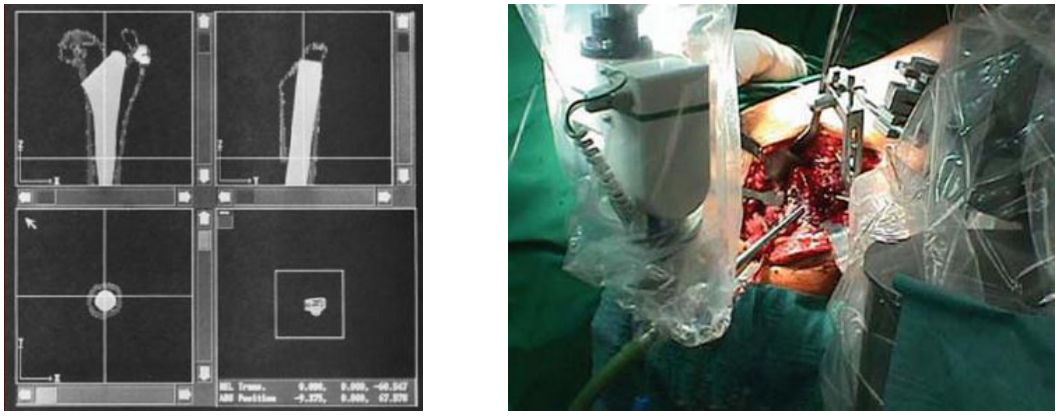

(a) Orthodoc (b)

Figure 2.9. The RoboDoc system for orthopedic surgery. (a) Registration and surgical plan on Orthodoc. (b) Close-up of robotic milling of femur[44].

The RoboDoc can achieve higher precision and sub-millimeter precision in bone milling[44]. The steady control of the surgical operation and boundary programming can avoid accidental damage to surrounding areas. During the process, the surgeon is able to observe where the robot is milling in comparison to the initial 3D reconstructed bone anatomy on the Orthodoc software.

However, the complex fixation of the bone structure and system set-up cost much time for operation which may cause post-operative pain. In the other hand, for lack of the all field tracking system, if the bone shift is detected, the milling is inter-

rupted and the registration process must be repeated. During the actual surgery, the surgeon is unable to intervene the operation especially in unpredictable circumstances[45].

CASPAR

As a directly competitive product to RoboDoc, CASPAR (Computer Assisted Surgical Planning and Robotics) was developed in 1997 by OrthoMaquet. The CASPAR was based on the industrial RX 90 which is 6 DoF clean room robot developed by Stäubli. The principle of CASPAR appears like that of RoboDoc, which has been used automatically for hip and knee implantation surgery, as well as for anterior cruciate ligament reconstruction[46](see Figure 2.10 (a)).

The CASPAR surgery process consists of four step by step phases. First, surgeons insert rigid bodies, commonly pins, at different locations around the knee. The process requires local or total anesthesia, and a tibial pin is placed 8 to 10 cm above and below the knee joint. The aim of the first step is for registration and referencing. Second, CT-scan is performed to retrieve pre-operative data and images of the knee. Next, the surgeon can perform pre-operative planning with the data. It generally involves measuring the femur and the tibia and planning the femur and tibia tunnels in a 3D environment. Finally, the robotics can do the tunnel drillings automatically under surgeon's supervision[47](see Figure 2.10 (b)).

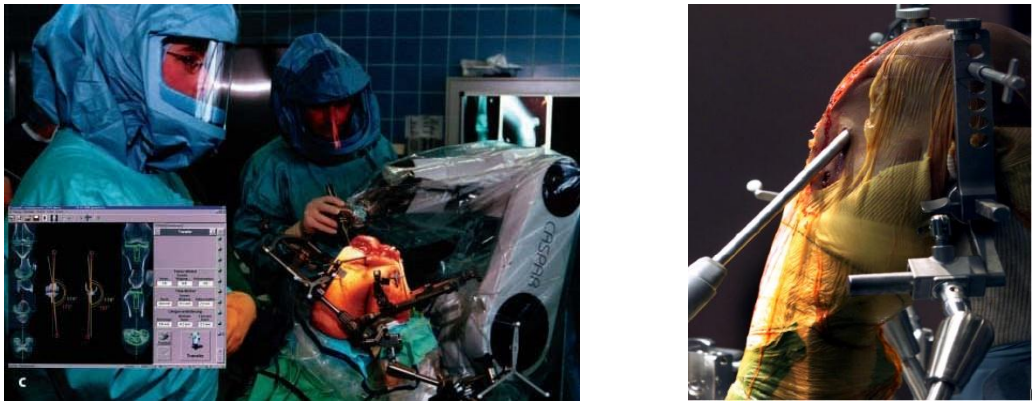

(a) (b)

Figure 2.10. (a) Total knee replacement by CASPAR[47]. (b) Tunnel drilling[47].

Arthrobot

To simplify robot assisted surgery, the Arthrobot (developed by Kaist, Korea) system registration process uses a reamer attached gauge and a femoral frame to determine the position and orientation of the femur relative to the robot.

The reamer-shaped gauge is mounted onto the patient's femur as in a manual surgery then the manual broaching process is replaced by the robot. The reported advantage is the less complex registration process with limiting the reaming process to the metaphyseal region meanwhile leaving the diaphyseal hard bone untouched. In an experiment with composite and pig bones 93% of the gaps between the bon e and implant surface were under the critical .25 mm[48].

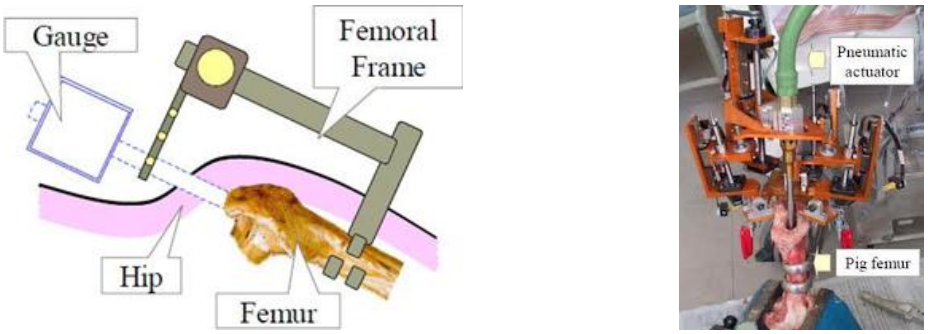

(a) (b)

Figure 2.11. (a) Efficient work space through gauge based registration. (b) Pig femur experiment.

2.3.3 Interactive Systems

Acrobot

Acrobot (developed by Davises, Imperial College London, UK) is designed for Total Knee Replacement. The hands-on robot, in which the surgeon and robot participated in the process as a unit, was treated as an intelligent tool under the surgeon's control [49].

During the operation, the surgeon stays in control; the robot actively constrained the surgeon's movements through haptic feedback to keep them within a safe predetermined region in the operative field. Acrobot allows the surgeon to remain in contact with the patient and move the robotic arm with his hand while controlling the cutting tool [50].

(a) (b)

Figure 2.12. (a) Acrobot for knee surgery. (b).Manipulation of the hands-on robot [50].

RIO

The RIO robotic arm(by MAKO Surgical Corp) was released in 2009 and received FDA clearance[51]. With three components: robotic arm, optical camera and operator computer, the RIO offers the surgeon visual, auditory, and tactile feed-back in minimally invasive surgery for medial and lateral UKA components as well as patellofemoral arthroplasty (see Figure 2.13 (a)).

Different from the autonomous robot such as Robodoc, both the RIO and the surgeon simultaneously hold the surgical tool, manipulating the bone-removing burr within the intended volume but restricting motion beyond that predetermined volume. With the low friction and low inertia robotic arm, the surgeon can easily move the tool and back drive the robot's joint motors in the process (see Figure 2.13 (b)). During milling process, the arm acts as a haptic device resisting motions outside of the planned cutting envelope by pushing back on the surgeon's hand[52]. Different from other active or semi-active robot systems, during surgery process, the bone is not required to be fixed in place, RIO system relies on an optical camera system to track osseous reference markers' position on the bone and tools and instantaneously register the planned cutting envelope to the patient in the operating room[52].

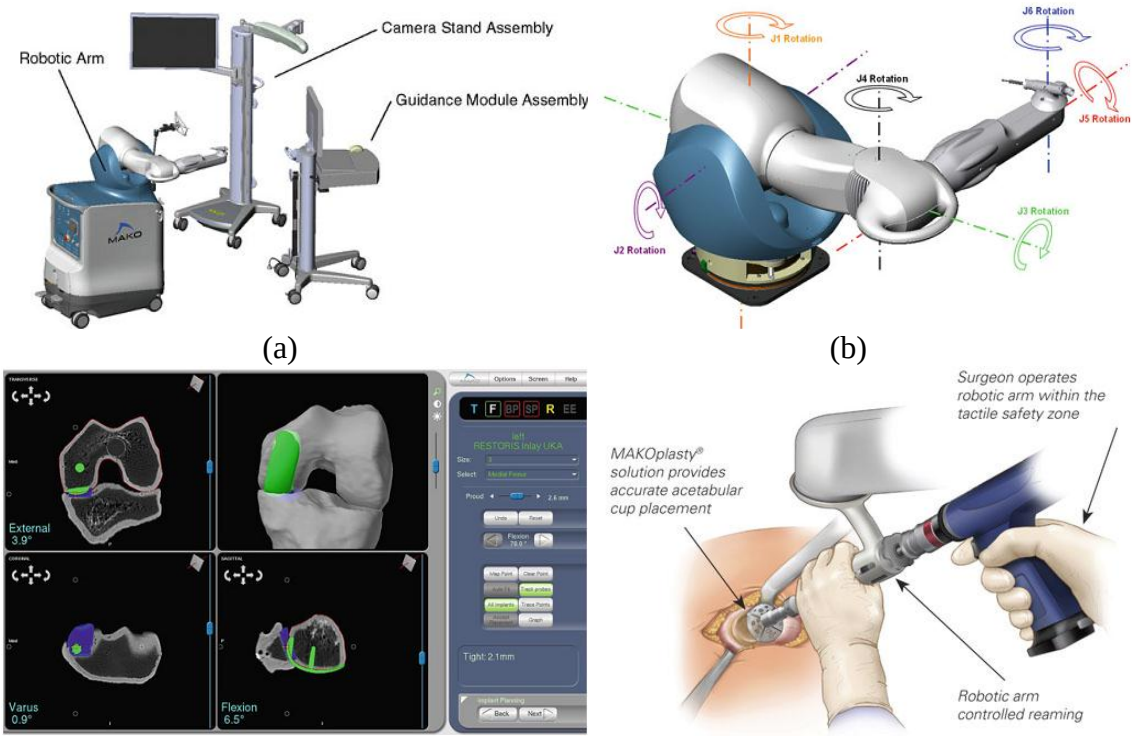

(a) (b)

(c) (d)

Figure 2.13.(a) RIO robotic arm interactive orthopedic system (b)Joint motion of the RIO robotic arm. (c) CT based patient specific pre-operative planning[52] (d) Total Hip Arthroplasty performed by RIO.

NeuroMate

The NeuroMate, now as the product of Renishaw (Wotton-under-Edge, UK), was the first neurosurgical robotic device to get a CE mark in Europe and FDA in USA. This robot was designed for neurosurgical process[53]. The 5 DoF robot provides an accurate and trusted assistance for supervised needle positioning and instrument holding for brain biopsy (see Figure 2.14(a)). Besides biopsy, the system is also marketed for deep brain stimulation, transcranial magnetic stimulation, stereotactic electro encephalography, radiosurgery and neuroendoscopy[20].

(a) (b)

Figure 2.14. (a) Neuromate for brain biospys (courtesy of Renishaw plc). (b) Neuromate with force sensor for skull surgery[54].

Xia,et al [54] developed an image-guided robotic system to provide mechanical assistance for skull base drilling. This system comprises Stealthstation navigation system, a NeuroMate robotic arm with 6-axes force sensor, and the 3D Slicer visualization software. In this system, the robotic arm of NeuroMate is under cooperative control of the surgeon via handle with force sensor mounted (see Figure 2.14(b)). The concept of virtual fixtures was used to constrain the motion of the robot-held cutting tool, promising remained in the safe zone defined on a pre-operative CT scan[54].

2.3.4 Tele-operative Systems

Zeus

The first generation commercial robotic system for laparoscopy is called AESOP, developed by Computer Motion. AESOP is designed for either holding endoscopes or moving the endoscope under voice control. In 1995, Computer Motion combined two tool-holding robot arms with AESOP to create the next generation product Zeus[55].

Zeus has two main parts: a surgeon control console and 3 table-mounted robotic arms (see Figure 3.12). The right and left robotic arms resemble that of the surgeon for doing surgery. The third arm is an AESOP voice-controlled robotic endoscope for visualization. In the Zeus system, The robotic arm s were tele-operated, following motions the surgeon made with instrument controls, and the surgeon is seated comfortably upright with the video monitor and instrument handles positioned ergonomically to maximize dexterity and allow complete visualization of the OR environment. The system uses both straight shafted endoscopic instruments similar to

conventional endoscopic instruments and jointed instruments with articulating end-effectors and seven degrees of freedom[56].

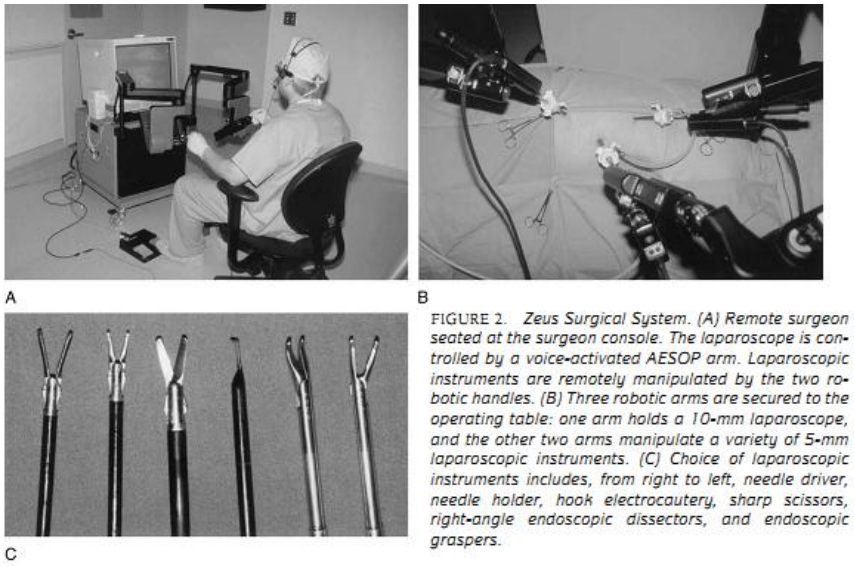

FIGURE 2. *Zeus Surgical System. (A) Remote surgeon seated at the surgeon console. The laparoscope is controlled by a voice-activated AESOP arm. Laparoscopic instruments are remotely manipulated by the two robotic handles. (B) Three robotic arms are secured to the operating table: one arm holds a 10-mm laparoscope, and the other two arms manipulate a variety of 5-mm laparoscopic instruments. (C) Choice of laparoscopic instruments includes, from right to left, needle driver, needle holder, hook electrocautery, sharp scissors, right-angle endoscopic dissectors, and endoscopic graspers.*

Figure 2.15. Zeus tele-surgery system[55]

In September 2001, with Zeus system, Marescaux and his team implemented 45-minute cholecystectomy surgery on a 68-year-old female patient between Strasbourg, France and New York, USA[56]. This so-called Lindbergh Operation was considered the first time in medical history that a technical solution proved capable of reducing the time delay inherent to long distance transmissions sufficiently to make this type of process possible[57].

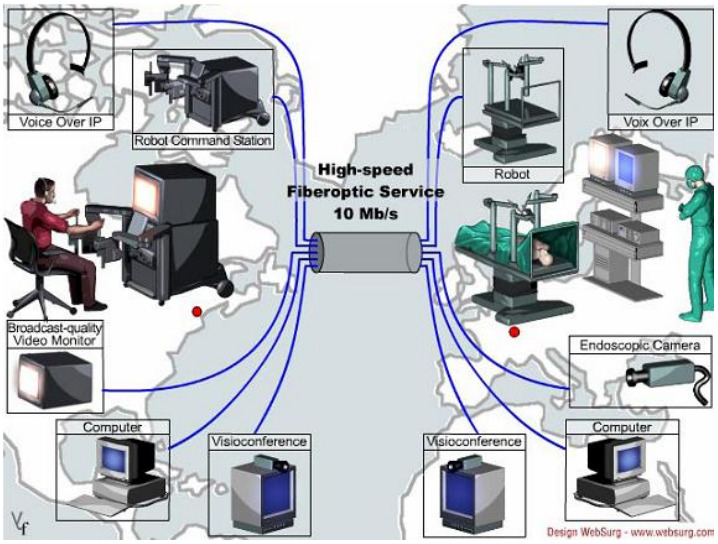

Figure 2.16. Configuration of Zeus system for Lindbergh Operation[58]

da Vinci

The da Vinci, developed by Intuitive Surgical Inc., is a tele-operated system like the Zeus. Because Zeus system is discontinued commercially, Zeus and da Vinci system represent the past and current versions of well-known commercially available robotic tele-surgery platforms[59].

The console is suitable designed for surgeon ergonomics and incorporates a separate video screen to display 3D video from the 3D endoscope (see Figure 2.17(a)). During surgery, the ends of the tools replicate the motions of the surgeon's hands, providing a more intuitive control rather than the "mirror-image" laparoscopic mapping (see Figure 2.17(b) (c)). The overall precision is improved by motion reduction scaling and by filtering involuntary motions caused by tremor[18].

The da Vinci system has several technical advantages over the Zeus. The grasper tools have two degrees of freedom inside the patient; the most salient feature is a three-axis wrist called EndoWrist which mimics the motion freedoms of the human wrist (see Figure 2.17(d)). Through the use of a master-slave robotic system, surgeon motions are scaled down, allowing the doctor to make more natural movements. By manipulating additional robotic arms, the surgeon can move the instruments with the required precision[60].

(a)

(b)

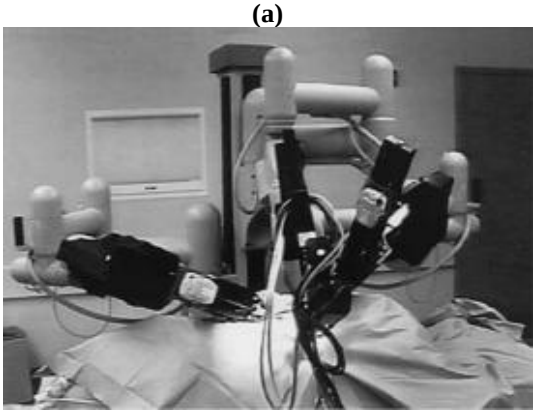

(c)

(d)

Figure 2.17. The da Vinci system. (a) Console part. (b) Surgeon's view and intuitive telemanipulator (c) three robotic arms (d) comparison of EndoWrist and human wrist[55].

The da Vinci, initially cleared by FDA for general laparoscopy, become commonly used for radical prostatectomy, and is now cleared for various surgery [61]. There are over 300 sites in the United States that are currently using the da Vinci surgical system and the number of surgeries that it is being utilized for is growing. The use of robots has grown from 1,500 cases in 2000 to an estimated 20,000 cases in 2004[62].

However, The da Vinci system costs $1.4 million, and maintenance costs are $140,000 per year, the financial burden would increase by $2698 per patient, given an average of 126 cases per year [63]. The huge space needed for system setup and the significant amount of necessary training are also the limitation of da Vinci system[64].

Chapter 3. System Architecture

Particularly for common robotic assisted orthopedic surgery, the surgical system consists of guidance, navigation and robotic control systems. In pre-operative procedure, the surgical protocols are planned. Typically pre-operative scanned 3D CT/MRI images are obtained and then registered to the intra-operative instantaneous 2D X-ray image by the C-arm. Optical tracking technique is more accurate and popular than other physical tracking means such as electromagnetic tracking and ultrasound tracking systems. In order to obtain aligned localization, the optical markers are fixed on the surgical tool, C-Arm, robotic arm and surgical object. With the obtained location and orientation information, the surgeons are able to guide or manipulate the robot arm to perform the pre-designed surgery plan (see Figure 3.1).

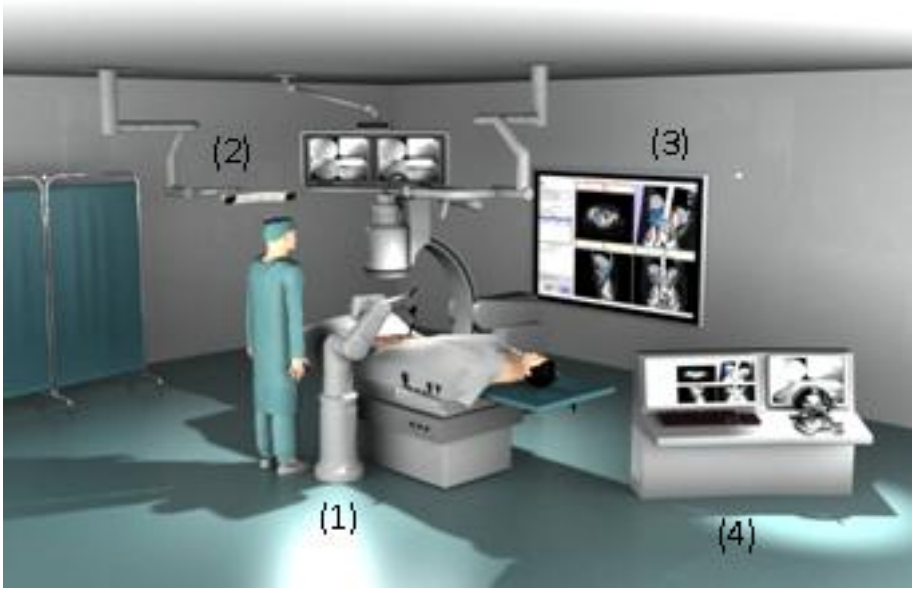

Figure 3.1. Scenario of the CAOS system in operating room. (1) Robot control system. (2) Optical tracking system. (3) Navigation system. (4) Tele-operation and haptic control system. In addition, there are C-arm and other necessary devices in the operating room.

3.1 The Integrated System

In the next section, we will give details about the main four parts of this system.

3.1.1 Robot Control System

Although there are some customized or dedicated surgical robot commercialized or under development in different institutes, we turn our view priory to the indus-

trial robot because of the cost, fast design with environmental compatibility and newly developed features of the industrial robot.

In contrast to industrial environment, the orthopedic surgery has specific requirements; the most significant thing is the safety margin which should be less than 2mm. The robot is expected to serve two basic surgeon-supervised working modes: Sleeve guiding and screw guiding. The first mode simply allows the robot to automatically move the light-weight sleeve (around 0.5 Kg) to pre-planned position with appropriate orientation. Then the surgeons perform drilling through the holding sleeve with screw driver by surgeon's hands. The second mode expects the robot arm to directly manipulate the screw driver to the desired position along the pre-planned path. In the actual surgery, the payload is as high as 70N measured by force gauge, because of the weight of screw driver and resistance from surgical object, such as bone. Indeed, both modes allow surgeons to intervene immediately whenever necessary [65].

Another critical point is that the operation room should be extremely clean and sterilized during surgery. Though not approved by FDA, series of industrial robots had been designed for using in hyper-clean room.

Considering above specific issues, the Stäubli six DoF robot TX60-SCR, designed for super clean room standard and hydrogen peroxide sterile, is a good choice. The robot is featured with 0.02mm repeatability, 9kg payload and 670mm reachability.

During the surgical process, the TX60-SCR, equipped with surgical tool and optical tracking markers, is controlled by surgeons via the robot controller. The force sensor, integrated on the robot wrist, can sample the environment contact force and manipulator's force. These force information, together with surgical plan provided by the navigation system, are taken as the input of the motion control algorithm. The output is the robustness desired robot motion (position or velocity) (see Figure 3.2(1)).

The low level control of the robot arm is implemented through the low level Interface called Real Time Robot Controller Abstraction Layer (RTRCAL) embedded in Stäubli CS8C robot controller [66]. With the RTRCAL, the control algorithm can directly get the feedback data including position, velocity, torque and position error, which represents the status of the robot. As the output result of the control law, commands, including position, velocity, anticipation velocity and anticipation torque, are sent to the robot in real-time to serve in the surgery.

3.1.2 Optical Tracking System

In the CAOS, the spatial location system, which is always considered as part of the navigation system, plays an important role by providing the relative positions and orientations among the surgical instruments, surgical objects and medical image scanners (e.g. CT, MRI and C-Arm) after registration [67]. Since orthopedic surgery is an exposure operation, the optical tracking system (NDI Polaris Hybrid Spectra) is introduced in our system which can implement the accurate position tracking in sub-millimeter (see Figure 3.2(2)).

For the fast and easy development, we applied the Image-Guided Surgery Toolkit (IGSTK) as the middleware to communicate with the tracking device. The IGSTK is a high-level, component-based framework integrated with low-level open source libraries and application programming interfaces (API) from hardware vendors [68]. With this toolkit, engineers can easily capture the position of multiple objects, besides this, the toolkit can provide some basic but versatile functionalities and process, such as the calibration and registration, for the image-guided surgery applications [69].

3.1.3 Navigation System

As significant part of the CAOS system, navigation system provides the complete visualization of the surgical process for surgeons. It should provide the following basic functions:

1) presenting virtual representations of the operated anatomy and the performed surgical action;
2) matching the replayed scene with what is performed at the surgical situation, by linking this virtual model to the operated patient;
3) visualizing the spatial relationship between multiple tracked objects;
4) incorporating other physical modalities such as acting force or torque of surgical tools [67].

We propose using 3D slicer as the navigation system. Initially, 3D Slicer is designed as a free, open source software package for visualization and image analysis (see Figure 3.2(3)). With the quadrant-view display and interactive GUI, 3D Slicer can be used as useful tool for medical image processing, analysis, visualization and fast 3D reconstruction. Since 3D Slicer supports extensive functional modules, it can be used to construct and visualize the patient's anatomy from multimodal images (CT/MRI) which are collected pre-operative or intra-operative. Through those pro-

cesses, surgeons can do the surgical planning or observe relative position and movement between planned regions and surgical tools [70].

OpenIGTLink, which can serve as an external module of 3D slicer, provides a simple but extensible data format to transfer various types of data among software and devices used in image-guided therapy (IGT) scenario, e.g. surgical navigation software, tracking device, robotic device and imaging scanner. The protocol can handle image, tracking data, transformation, device control and monitoring command, and other user-defined data types [71]. In the proposed system, OpenIGTLink could act as the communication protocol for data transmission among the robot control system, tracking system, navigation system and medical imaging instruments.

3.1.4 Tele-operation and Haptic Control System

In almost cases of orthopedic surgery, the surgeons always work under the hazardous radiation device, such as X-ray, during the entire surgical process[72]. To prevent surgeons from the damage of radiation, the tele-operation control of the robot will be also explored in our research.

For this purpose, we use the Omega.6 (Force Dimension, Inc.) as the tele-operation and haptic device for our robotic surgery system (see Figure 3.2(4)). With high-precision, 6 DoF, pen-shaped end-effector to accurately, omega.6 can capture the position and orientation of the operator's hand. With a perfect counter-balanced kinematic design around each joint, the pen combines performance, dexterity and elegance into one of the most accomplished haptic interfaces. This highly ergonomic end-effector makes the omega.6 better choice for surgery training, medical robotics which require operating robots remotely [73].

Force Dimension provides haptic CHAI3D framework[74] compatible to this haptic device, we are able to import 3D reconstructed medical model based on VTK. With advanced force-feedback rendering capabilities, these applications are perfect for medical simulating and training.

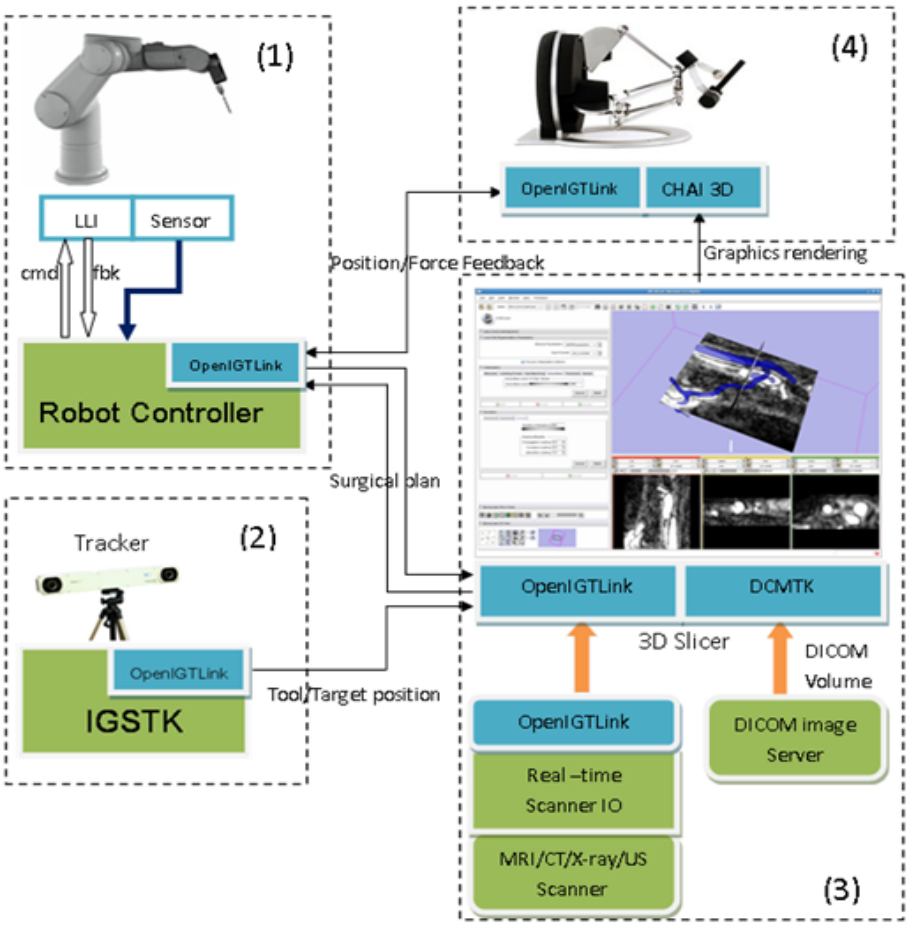

Figure 3.2. Architecture of proposed robot assisted surgery system.

3.2 Motion Analysis of Surgical Robot

In consideration for the working space of the surgery and the available space in the operating room, the TX60 robot arm is adopted in this system. TX60 is an industrial robot with six degrees of freedom, as shown in Figure 3.3. Within its working space, the robot can move to the desired position and orientation along pre-planned trajectory.

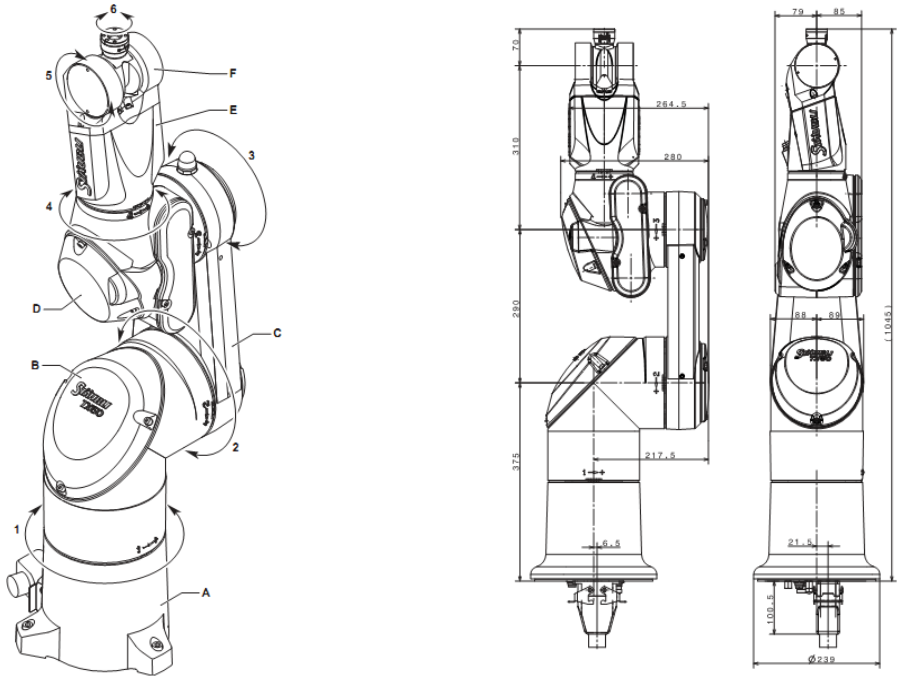

(a) (b)

Figure 3.3. (a) Six main parts of the robot arm are: the base (A), the shoulder (B), the arm (C), the elbow (D), the forearm (E) and the wrist (F). (b) Dimension of each part of the robot arm.

According to the Craig's book[75], we can use the modified Denavit-Hartenberg(MDH) parameters to describe the link of revolute or prismatic joints (see Figure 3.4).

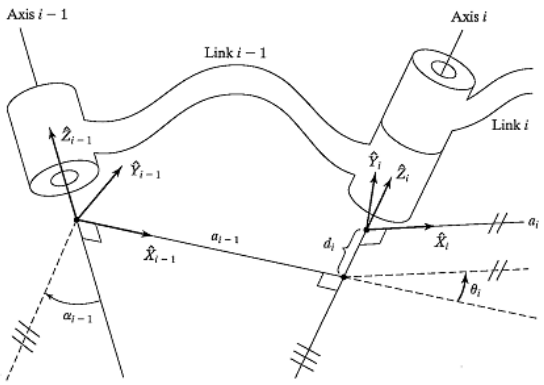

Figure 3.4. The modified Denavit-Hartenberg notation for link i-1 and link i [76].

Frame $\{i\}$ is attached rigidly to link i

$\hat{Z}_i$ is the Z-axis of the frame $\{i\}$ coincident with the joint axis i.

$\hat{X}_{i-1}$ axis is located along the common normal between $\hat{Z}_{i-1}$ and $\hat{Z}_i$ axes.

The origin of frame is at the intersection of the $\hat{X}$ and $\hat{Z}$.

a_i: the distance from $\hat{Z}_i$ to $\hat{Z}_{i+1}$ measured along $\hat{X}_i$.

α_i: the angle from $\hat{Z}_i$ to $\hat{Z}_{i+1}$ measured along $\hat{X}_i$.

d_i: the distance from $\hat{X}_{i-1}$ to $\hat{X}_i$ measured along $\hat{Z}_i$.

θ_i: the angle from $\hat{X}_{i-1}$ to $\hat{X}_i$ measured along $\hat{Z}_i$.

Table 3–1.Modified DH parameters of TX60

i	α_{i-1}	a_{i-1}	d_i	θ_i
1	0	0	0	θ_1
2	$-\frac{\pi}{2}$	0	0	θ_2
3	0	a_2	d_3	θ_3
4	$-\frac{\pi}{2}$	0	d_4	θ_4
5	$\frac{\pi}{2}$	0	0	θ_5
6	$-\frac{\pi}{2}$	0	d_6	θ_6

Table 3–1 lists the modified DH parameters for TX60, $a_2 = 290mm$, $d_3 = 20mm$, $d_4 = 310mm$ and $d_6 = 70mm$.

3.2.1 Forward Kinematics of TX60

We set frame $\{0\}$ as the base frame and T_i^{i-1} as the transformation between the adjacent $\{i\}$ and $\{i-1\}$ frame. T_i^{i-1} is 4×4 homogeneous matrix including rotation and translation parts:

$$T_i^{i-1} = \begin{bmatrix} \cos\theta_i & -\sin\theta_i & 0 & a_{i-1} \\ \sin\theta_i \cos\alpha_{i-1} & \cos\theta_i \cos\alpha_{i-1} & -\sin\alpha_{i-1} & -d_i \sin\alpha_{i-1} \\ \sin\theta_i \sin\alpha_{i-1} & \cos\theta_i \sin\alpha_{i-1} & \cos\alpha_{i-1} & d_i \cos\alpha_{i-1} \\ 0 & 0 & 0 & 1 \end{bmatrix} \quad (3\text{-}1)$$

TX-60 is a six serial chain joints robotic arm, therefore the forward kinematic of the end-effector is

$$T_6^0 = T_1^0 T_2^1 T_3^2 T_4^3 T_5^4 T_6^5 \quad (3\text{-}2)$$

We can derive T_6^0 step by step with result as

$$T_6^0 = \begin{bmatrix} n_x & o_x & a_x & p_x \\ n_y & o_y & a_y & p_y \\ n_z & o_z & a_z & p_z \\ 0 & 0 & 0 & 1 \end{bmatrix} \quad (3\text{-}3)$$

where

$$\begin{aligned} n_x &= c_1\big[\, c_{23}(c_4c_5c_6 - s_4s_6) - s_{23}s_5c_6 \,\big] + s_1 \;\; s_4c_5c_6 + c_4s_6 \\ n_y &= s_1\big[\, c_{23}(c_4c_5c_6 - s_4s_6) - s_{23}s_5c_6 \,\big] - c_1 \;\; s_4c_5c_6 + c_4s_6 \\ n_z &= -s_{23} \;\; c_4c_5c_6 - s_4s_6 \;\; - c_{23}s_5c_6 \end{aligned}$$

$$\begin{aligned} o_x &= c_1\big[\, c_{23}(-c_4c_5c_6 - s_4c_6) + s_{23}s_5s_6 \,\big] + s_1 \;\; c_4c_6 - s_4c_5s_6 \\ o_y &= s_1\big[\, c_{23}(-c_4c_5c_6 - s_4c_6) + s_{23}s_5c_6 \,\big] - c_1 \;\; c_4c_6 - s_4c_5s_6 \\ o_z &= -s_{23} \;\; -c_4c_5s_6 - s_4c_6 \;\; + c_{23}s_5s_6 \end{aligned}$$

$$\begin{aligned} a_x &= -c_1\big[\, c_{23}c_4s_5 + s_{23}c_5 \,\big] - s_1s_4s_5 \\ a_y &= -s_1\big[\, c_{23}c_4s_5 + s_{23}c_5 \,\big] + c_1s_4s_5 \\ a_z &= s_{23}c_4s_5 - c_{23}c_5 \end{aligned}$$

$$\begin{aligned} p_x &= a_2c_1c_2 - d_3s_1 - d_6[s_5 \cdot (s_1s_4 + c_1c_4c_{23}) + c_1c_5s_{23}] - d_4c_1s_{23} \\ p_y &= a_2s_1c_2 + d_3c_1 + d_6[s_5 \cdot (c_1s_4 - s_1c_4c_{23}) - s_1c_5s_{23}] - d_4s_1s_{23} \\ p_z &= d_6[s_{23}c_4s_5 - c_{23}c_5] - d_4c_{23} - a_2s_2 \end{aligned}$$

$$s_i : \sin(\theta_i), c_i : \cos(\theta_i), s_{ij} : \sin(\theta_i + \theta_j), c_{ij} : \cos(\theta_i + \theta_j)$$

With above formulas, we can get the direct movement workspace of robotic arm. The position of all the links of a manipulator of n degrees of freedom can be specified with a set of n joint variables, referred to $n \times 1$ joint vector. We can compute the position in Cartesian space from the knowledge of the joint space[76]. Con-

versely, the inverse kinematics is to get the joint space description from the Cartesian space information (see Figure 3.5).

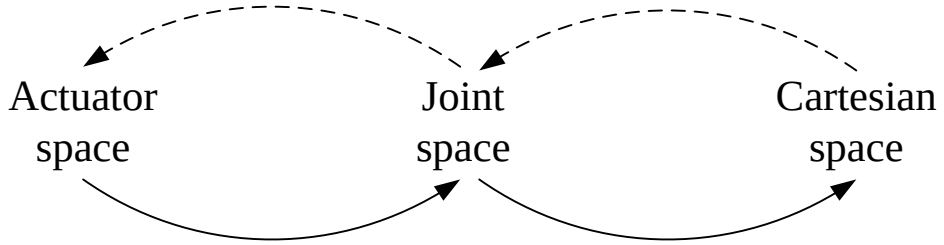

Figure 3.5. Mappings among different kinematic space.

3.2.2 Singularity Analysis

For static case, the Cartesian space and joint space can be formed by

$$p = T(\theta) \tag{3-4}$$

$\theta = [\theta_1, \theta_2, \cdots, \theta_n]$ is the joint rotation vector (n is the joint number of the robotic arm), p is the position in the Cartesian space. $p = [x, y, z, \alpha, \beta, \gamma]^T$, x , y , z are translation in position coordinates, the α , β , γ are Euler angle in orientation coordinates.

For movement of robotic arm, Jacobian matrix can be used to describe joint velocities with Cartesian velocities at the end-effector of the arm

$$\dot{p} = J(\theta)\dot{\theta} \tag{3-5}$$

where $\dot{\theta}$ is the joint velocities vector, $\dot{p}$ is the Cartesian velocities vector. $\dot{p} = [v, \omega]^T$, v is the linear velocities vector for translation, and ω is the angular velocities vector for rotation. $J(\theta)$ can be taken as the first derivative of $T(\theta)$. $J(\theta)$ is a nonlinear matrix function of instant θ , in many cases, $J(\theta)$ is not full rank, thus to directly get joint velocities $\dot{\theta} = J^{-1}(\theta) \cdot \dot{p}$ is an illness inverse problem, called singularity problem.

There are various methods to handle the singularity problem, starting from the simple approach of switching into joint space control[77].Others developed techniques to make manipulator to avoid the singularities[78, 79].In this section, we discuss on the real-time singularity analysis and robust control methods, if the reference trajectory is not known a priori and the robot is non-redundant.

For the convenient analysis of the singularity of robotic arm, first we put the frame $\{4\}$, $\{5\}$ and $\{6\}$ together as the wrist frame (see Figure 3.6).

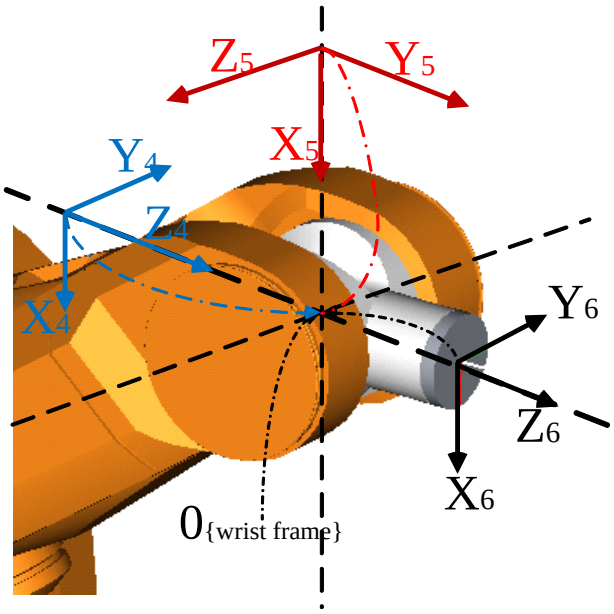

Figure 3.6. Wrist frame of TX60

In this case, we consider the wrist as a sphere (frame $\{4\}$, $\{5\}$ and $\{6\}$ share the same origin), which has only rotation and no translation. Since $J(\theta)$ is the first partial derivative of $T(\theta)$ and $T(\theta)$ is formulated in section 3.2.1, we can get the wrist frame Jacobian matrix as

$$ {}^{0}J_{W} = \begin{pmatrix} {}^{0}J_{11} & 0_{3\times3} \\ {}^{0}J_{21} & {}^{0}J_{22} \end{pmatrix} \tag{3-6} $$

W means wrist, thus $\left|{}^{0}J_{W}\right| = \left|{}^{0}J_{11}\right| \cdot \left|{}^{0}J_{22}\right|$ and the determinant of Jacobian matrix $\left|{}^{0}J_{W}\right|$ is independent of reference frames.

Now the Cartesian movement can partitioned to translation and rotation parts:

$$ \dot{p}_{\mathrm{w}} = \begin{bmatrix} V_{W} \\ \Omega_{W} \end{bmatrix} = {}^{0}J_{W} \begin{bmatrix} \dot{\theta}_{A} \\ \dot{\theta}_{W} \end{bmatrix} \tag{3-7} $$

$\dot{\theta}_{A} = [\dot{\theta}_{1} \quad \dot{\theta}_{2} \quad \dot{\theta}_{3}]^{T}$ are the forearm joints, $\dot{\theta}_{W} = [\dot{\theta}_{4} \quad \dot{\theta}_{5} \quad \dot{\theta}_{6}]^{T}$ are the wrist joints.

The translation of the Cartesian movement is only related to the first three joints:

$$ \begin{aligned} V_{W} &= {}^{0}J_{11}\dot{\theta}_{A} \\ \Omega_{W} &= {}^{0}J_{21}\dot{\theta}_{A} + {}^{0}J_{22}\dot{\theta}_{W} \end{aligned} \tag{3-8} $$

where V_{W} is the translation part, Ω_{W} is the rotation part. Substitute with the modified DH parameters, we can get

$$
{}^{0}J_{11} = \begin{pmatrix} s_1(d_4 s_{23} - a_2 c_2) - d_3 c_1 & -c_1(d_4 c_{23} + a_2 s_2) & -d_4 c_1 c_{23} \\ -c_1(d_4 s_{23} - a_2 c_2) - d_3 s_1 & -s_1(d_4 c_{23} + a_2 s_2) & -d_4 s_1 c_{23} \\ 0 & d_4 s_{23} - a_2 c_2 & d_4 s_{23} \end{pmatrix}
$$

$$
{}^{0}J_{21} = \begin{pmatrix} 0 & -s_1 & -s_1 \\ 0 & c_1 & c_1 \\ 1 & 0 & 0 \end{pmatrix}
$$

$$
{}^{0}J_{22} = \begin{pmatrix} -c_1 s_{23} & -s_1 c_4 + c_1 c_{23} s_4 & -s_1 s_4 s_5 - c_1 s_{23} c_5 - c_1 c_{23} c_4 s_5 \\ -s_1 s_{23} & c_1 c_4 + s_1 c_{23} s_4 & c_1 s_4 s_5 - s_1 s_{23} c_5 - s_1 c_{23} c_4 s_5 \\ -c_{23} & -s_{23} s_4 & s_{23} c_4 s_5 - c_{23} c_5 \end{pmatrix}
$$

thus $\left| {}^{0}J_{W} \right| = -a_2 \cdot d_4 \cdot c_3 \cdot (d_4 s_{23} - a_2 c_2)$.

Similarly, we can derive the wrist Jacobian matrix in the wrist frame

$$
{}^{W}J = \begin{pmatrix} {}^{W}J_{11} & 0_{3\times 3} \\ {}^{W}J_{21} & {}^{W}J_{22} \end{pmatrix} \tag{3-9}
$$

thus $\left| {}^{W}J \right| = -s_5$.

From equations (3-6) and(3-9), there are two type of singularity problem: forearm singularity and wrist singularity. Furthermore, the forearm singularity can be classified as boundary singularity and interior singularity:

- ***Forearm singularity***: $\left| {}^{0}J_{W} \right| = -a_2 \cdot d_4 \cdot c_3 \cdot (d_4 s_{23} - a_2 c_2) = 0$

1) Boundary singularity(Elbow lock): $c_3 = 0$

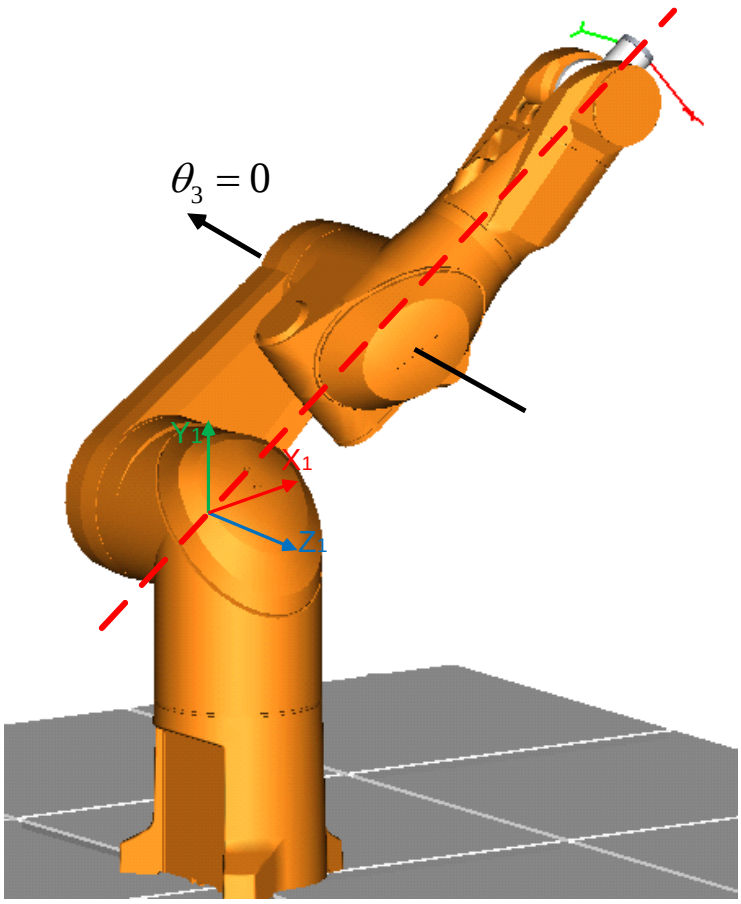

Figure 3.7. Boundary singularity case.

2) Interior singularity(Head lock): $d_4 s_{23} - a_2 c_2 = 0$

When only interior singularity occurs, wrist frame locates at the Y_1-Z_1 plane (see Figure 3.8):

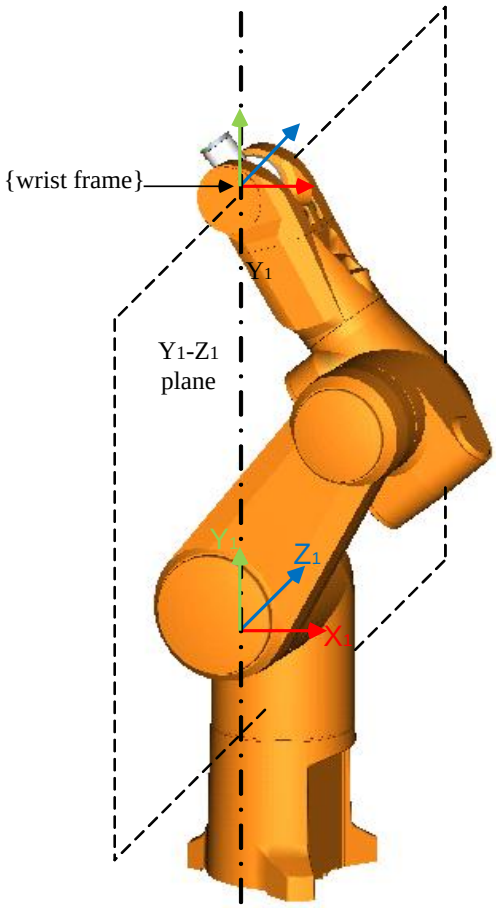

Figure 3.8. Interior singularity case.

In this case, the Jacobian matrices have the following forms:

$$ {}^{3}J_{11} = \begin{pmatrix} * & * & * \\ * & * & * \\ 0 & 0 & 0 \end{pmatrix}, {}^{2}J_{11} = \begin{pmatrix} * & * & * \\ * & * & * \\ 0 & 0 & 0 \end{pmatrix}, {}^{1}J_{11} = \begin{pmatrix} * & * & * \\ 0 & 0 & 0 \\ * & * & * \end{pmatrix}, {}^{0}J_{11} = \begin{pmatrix} * & * & * \\ 0 & 0 & 0 \\ * & * & * \end{pmatrix} $$

Translations along the Z_3 axis in frame {3}, Z_2 axis in frame {2}, Y_1 axis in frame {1} and Y_0 axis in frame {0} are singular.($*$ is any number rather than zero)

3) When both boundary and interior singularity occur: $c_3 = 0$ and $d_4 s_{23} - a_2 c_2 = 0$,

for modified DH parameter: $\theta_3 = -\frac{\pi}{2}$ and $\theta_2 = -\frac{\pi}{2}$.

In this case, the Jacobian matrices have the following forms:

$$ {}^{3}J_{11} = \begin{pmatrix} * & * & * \\ 0 & 0 & 0 \\ 0 & 0 & 0 \end{pmatrix}, {}^{2}J_{11} = \begin{pmatrix} 0 & 0 & 0 \\ * & * & * \\ 0 & 0 & 0 \end{pmatrix}, {}^{1}J_{11} = \begin{pmatrix} * & * & * \\ 0 & 0 & 0 \\ 0 & 0 & 0 \end{pmatrix}, {}^{0}J_{11} = \begin{pmatrix} * & * & * \\ 0 & 0 & 0 \\ 0 & 0 & 0 \end{pmatrix} $$

Translations along the Y_3 and Z_3axis in frame {3}, X_1 and Z_2 axis in frame {2}, Y_1 and Z_1 axis in frame {1} and Y_0 or Z_0 axis in frame {0} are singular.($*$ is any number rather than zero).

- ***Wrist singularity*** **:** $\left|{}^{W}J\right| = -s_5 = 0$

When $\theta_5 = 0$, wrist singularity occurs and Z_4 and Z_6 axis are collinear, the singular direction is the rotation around the X_4 axis in $\{4\}$ frame, but the movement of the first three joints can change the position of the wrist.

3.2.3 Damped Least Squares (DLS):

To avoid illness Jacobian matrix J when robotic manipulator enters the singularity region, the actual joints velocities have to be adjusted. There is a traditional method to avoid singularity called *Damped Least Squares* (DLS).

To solve the solution $\dot{\theta}$ of the equation(3-5) as

$$\dot{X} = J(\theta)\dot{\theta} \tag{3-10}$$

We can change it to the following optimization issue

$$\begin{aligned} &\min : \left\| J \cdot \dot{\theta} - \dot{x} \right\|^2 \\ &\text{s.t. } \dot{\theta}_{\min} \le \dot{\theta} \le \dot{\theta}_{\max} \end{aligned} \tag{3-11}$$

Buss [80] introduced the damping factor $\lambda \in \Re$, the objective is to minimize

$$\left\| J \cdot \dot{\theta} - \dot{x} \right\|^2 + \lambda^2 \left\| \dot{\theta} \right\|^2 \tag{3-12}$$

This is equivalent to the minimizing the quantity

$$\left\| \begin{pmatrix} J \\ \lambda I \end{pmatrix} \cdot \dot{\theta} - \begin{pmatrix} \dot{x} \\ 0 \end{pmatrix} \right\|^2 \tag{3-13}$$

The corresponding normal equation is

$$\begin{pmatrix} J \\ \lambda I \end{pmatrix}^T \begin{pmatrix} J \\ \lambda I \end{pmatrix} \cdot \dot{\theta} = \begin{pmatrix} J \\ \lambda I \end{pmatrix}^T \begin{pmatrix} \dot{x} \\ 0 \end{pmatrix} \tag{3-14}$$

Then we can get the solution as

$$\dot{\theta}_d = (J^T J + \lambda^2 I)^{-1} J^T \dot{x} \tag{3-15}$$

The damping factor λ can be assigned to make $(J^T J + \lambda^2 I)$ non-singular.

$J^TJ \in \mathbb{R}^{n\times n}$, where n is the DoF of robot arm. Using the equivalent formula $(J^TJ+\lambda^2 I)^{-1}J^T = J^T(JJ^T+\lambda^2 I)^{-1}$ to simplify $\dot{\theta}_d$ as

$$\dot{\theta}_d = J^T(JJ^T+\lambda^2 I)^{-1}\dot{x} \tag{3-16}$$

Because $JJ^T \in \mathbb{R}^{m\times m}$ (m is the dimension of the space of end-effector position, m is often much less than n, however for TX60, $n=m=6$, $p=[x,y,z,\alpha,\beta,\gamma]^T$).

Singular Value Decomposition (SVD):

Singular value decomposition (SVD) method is always used to analyze the pseudo inverse of Jacobian and implement the algorithm of DLS.

$$J = U\Sigma V^T \tag{3-17}$$

If $J \in \mathbb{R}^{m\times n}$, then $U \in \mathbb{R}^{m\times m}$ and $V \in \mathbb{R}^{n\times n}$ (U, V are orthogonal matrices), $\Sigma \in \mathbb{R}^{m\times n}$ is diagonal matrix. The only non-zero entries in the matrix Σ are the values ρ_i (if we assume $m \le n$, $\rho_1 \ge \rho_2 \ge \cdots \ge \rho_m \ge 0$, then ρ_i is the singular value of J). In fact, if the rank of J is r, then $\rho_{r+1} = \rho_{r+1} = \cdots = \rho_m = 0$, if we express U and V in the form of column vectors, $U = [\mathrm{u}_1, \mathrm{u}_2 \cdots, \mathrm{u}_m], \mathrm{u}_i \in \mathbb{R}^m$ and $V = [\mathrm{v}_1, \mathrm{v}_2 \cdots, \mathrm{v}_n], \mathrm{v}_i \in \mathbb{R}^n$. The vectors $\mathrm{v}_{r+1}, \cdots, \mathrm{v}_n$ are an orthonormal basis for the null-space of J.

Then J can be written in the form

$$J = \sum_{i=1}^{m} \rho_i \, \mathrm{u}_i \mathrm{v}_i^T = \sum_{i=1}^{r} \rho_i \, \mathrm{u}_i \mathrm{v}_i^T \tag{3-18}$$

Through the SVD decomposition

$$JJ^T + \lambda^2 I = (U\Sigma V^T)(V\Sigma^T U^T) + \lambda^2 I = U(\Sigma\Sigma^T + \lambda^2 I)U^T$$

$$\begin{aligned} J^T(JJ^T+\lambda^2 I)^{-1} &= (V\Sigma^T U^T)\cdot(U(\Sigma\Sigma^T+\lambda^2 I)U^T)^{-1} \\ &= (V\Sigma^T U^T)\cdot U(\Sigma\Sigma^T+\lambda^2 I)^{-1}U^T \\ &= V\Sigma^T(\Sigma\Sigma^T+\lambda^2 I)^{-1}U^T \\ &= V\Sigma^* U^T \end{aligned}$$

where $\Sigma^* = diag(\frac{\rho_1}{\rho_1^2+\lambda^2},\ldots,\frac{\rho_m}{\rho_m^2+\lambda^2})$, then we get

$$J^T(JJ^T + \lambda^2 I)^{-1} = \sum_{i=1}^{m} \frac{\rho_i}{\rho_i^2 + \lambda^2} \mathrm{v}_i \, \mathrm{u}_i^T \tag{3-19}$$

Then the objective solution is $\dot{\theta}_d = \left[\sum_{i=1}^{m} \frac{\rho_i}{\rho_i^2 + \lambda^2} \mathrm{v}_i \, \mathrm{u}_i^T \right] \dot{x}$.

We can choose another strategy to damp the smaller singular values rather than the larger ones as

$$\dot{\theta}_d = \left[\sum_{i=1}^{k} \mathrm{v}_i \, \mathrm{u}_i^T + \sum_{j=k+1}^{m} \frac{\rho_j}{\rho_j^2 + \lambda^2} \mathrm{v}_j \, \mathrm{u}_j^T \right] \dot{x} \tag{3-20}$$

where the damped factor λ is only applied on smaller singular value.

Nakamura [81] suggested the damping factor λ can be chosen through the manipulability w defined as

$$w = \sqrt{\det(JJ^T)} \tag{3-21}$$

$$\lambda = \begin{cases} \lambda_0 \cdot (1 - \frac{w}{w_0})^2 & w \le w_0 \\ 0 & otherwise \end{cases} \tag{3-22}$$

Equation (3-22) is the piecewise function of λ, where λ_0 is the scale factor at singular points and w_0 is an experienced chosen threshold. Therefore, no damping is applied when the value of w is greater than w_0 until the λ reaches the maximum value λ_0 when $w = 0$ (singular case). (However λ_0 and w_0 are needed to be pre-assigned).

Through the properties of piecewise function, it will create discontinuities when go through non-singularity region to singularity region.

In practice, the damped factor can be simply chosen through the SVD as

$$\lambda = \begin{cases} \lambda_0 \cdot (1 - \frac{\rho_{min}}{\rho_0})^2, \ \rho_{min} < \rho_0 \\ 0 \qquad otherwise \end{cases} \tag{3-23}$$

$\rho_{\min}$ is the minimum singular value [81].

When $\lambda \to 0$, then $J^T(JJ^T + \lambda^2 I)^{-1} \to J^T(JJ^T)^{-1} = J^+$, where J^+ is the pseudo-inverse of Jacobian matrix.

3.2.4 Singularity Separation Damped Reciprocal (SSDR):

Different from the DLS method, this method using the specific separable properties of Jacobian matrix in the wrist frame, and do not need the SVD.

From equation(3-8), the translation of the Cartesian movement is only related to the first three joints

$$\begin{aligned} {}^0V_W &= {}^0J_{11}\dot{\theta}_A \\ {}^0\Omega_W &= {}^0J_{21}\dot{\theta}_A + {}^0J_{22}\dot{\theta}_W \end{aligned} \tag{3-24}$$

Substitute the modified DH parameters of TX60, we can get

$${}^0J_{11} = \begin{pmatrix} s_1(d_4 s_{23} - a_2 c_2) - d_3 c_1 & -c_1(d_4 c_{23} + a_2 s_2) & -d_4 c_1 c_{23} \\ -c_1(d_4 s_{23} - a_2 c_2) - d_3 s_1 & -s_1(d_4 c_{23} + a_2 s_2) & -d_4 s_1 c_{23} \\ 0 & d_4 s_{23} - a_2 c_2 & d_4 s_{23} \end{pmatrix}$$

$${}^0J_{21} = \begin{pmatrix} 0 & -s_1 & -s_1 \\ 0 & c_1 & c_1 \\ 1 & 0 & 0 \end{pmatrix}$$

$${}^0J_{22} = \begin{pmatrix} -c_1 s_{23} & -s_1 c_4 + c_1 c_{23} s_4 & -s_1 s_4 s_5 - c_1 s_{23} c_5 - c_1 c_{23} c_4 s_5 \\ -s_1 s_{23} & c_1 c_4 + s_1 c_{23} s_4 & c_1 s_4 s_5 - s_1 s_{23} c_5 - s_1 c_{23} c_4 s_5 \\ -c_{23} & -s_{23} s_4 & s_{23} c_4 s_5 - c_{23} c_5 \end{pmatrix}$$

The joint velocity of the first three joints $\dot{\theta}_A = [\dot{\theta}_1 \quad \dot{\theta}_2 \quad \dot{\theta}_3]^T$ can be resolved as

$$\dot{\theta}_A = ({}^0J_{11})^{-1}\,{}^0V_W \tag{3-25}$$

According to the coordinate transformation ${}^0J_{11} = {}^0R_3 \cdot {}^3J_{11}$, equation (3-25) can be written relative to {3} frame, then we can get

$$\begin{aligned} \dot{\theta}_A &= ({}^0J_{11})^{-1}\,{}^0V_W \\ &= ({}^0J_{11})^{-1}({}^0R_3 \cdot {}^3V_W) \\ &= ({}^0R_3 \cdot {}^3J_{11})^{-1}({}^0R_3 \cdot {}^3V_W) \\ &= ({}^3J_{11})^{-1}({}^3V_W) \end{aligned}$$

To do the frame transformation is that ${}^3J_{11}$ has a special property, we can derive ${}^3J_{11}$ as

$$ {}^3J_{11} = \begin{pmatrix} -d_3c_{23} & a_2s_3 - d_4 & -d_4 \\ d_3s_{23} & a_2c_3 & 0 \\ -(d_4s_{23} - a_2c_2) & 0 & 0 \end{pmatrix} \tag{3-26} $$

${}^3J_{11}$ is left upper-triangle matrix. Then the inverse of ${}^3J_{11}$ can be easily calculated as

$$ \begin{aligned} ({}^3J_{11})^{-1} &= \begin{pmatrix} 0 & 0 & -\dfrac{1}{(d_4s_{23} - a_2c_2)} \\ 0 & \dfrac{1}{a_2}\dfrac{1}{c_3} & \dfrac{d_3s_{23}}{a_2}\dfrac{1}{c_3}\dfrac{1}{(d_4s_{23} - a_2c_2)} \\ -\dfrac{1}{d_4} & \dfrac{a_2s_3 - d_4}{a_2d_4}\dfrac{1}{c_3} & \dfrac{-d_3}{a_2d_4}\dfrac{1}{c_3} \end{pmatrix} \\ &= \begin{pmatrix} 0 & 0 & -\dfrac{1}{k_1} \\ 0 & \dfrac{1}{a_2}\dfrac{1}{k_2} & \dfrac{d_3s_{23}}{a_2}\dfrac{1}{k_2}\dfrac{1}{k_1} \\ -\dfrac{1}{d_4} & \dfrac{a_2s_3 - d_4}{a_2d_4}\dfrac{1}{k_2} & \dfrac{-d_3}{a_2d_4}\dfrac{1}{k_2} \end{pmatrix} \end{aligned} \tag{3-27} $$

where $k_1 = d_4s_{23} - a_2c_2 = 0$ is the head lock singularity, and $k_2 = c_3 = 0$ is the elbow singularity.

$$ \begin{bmatrix} \dot{\theta}_1 \\ \dot{\theta}_2 \\ \dot{\theta}_3 \end{bmatrix} = ({}^3J_{11})^{-1} \begin{bmatrix} {}^3V_{W_X} \\ {}^3V_{W_Y} \\ {}^3V_{W_Z} \end{bmatrix} = \begin{bmatrix} -\dfrac{1}{k_1}\,{}^3V_{W_Z} \\ \dfrac{1}{k_2}(\dfrac{1}{a_2}\,{}^3V_{W_Y} + \dfrac{d_3s_{23}}{a_2}\dfrac{1}{k_1}\,{}^3V_{W_Z}) \\ -\dfrac{1}{d_4}\,{}^3V_{W_X} + \dfrac{1}{k_2}(\dfrac{a_2s_3 - d_4}{a_2d_4}\,{}^3V_{W_Y} - \dfrac{d_3}{a_2d_4}\,{}^3V_{W_Z}) \end{bmatrix} \tag{3-28} $$

When encountering the head lock singularity and elbow singularity, the damped factor λ_1 and λ_2 are involved to diminish the effect of these two singularities. However, these two singularities could not concur. Therefore, the estimated forearm joints velocities $\hat{\dot{\theta}}_A$ can be written as

$$\hat{\dot{\theta}}_A = \begin{bmatrix} \hat{\dot{\theta}}_1 \\ \hat{\dot{\theta}}_2 \\ \hat{\dot{\theta}}_3 \end{bmatrix} = \begin{bmatrix} -\dfrac{k_1}{k_1^2+\lambda_1^2}\,{}^3V_{W_Z} \\ \dfrac{k_2}{k_2^2+\lambda_2^2}\left(\dfrac{1}{a_2}\,{}^3V_{W_Y} + \dfrac{d_3 s_{23}}{a_2}\dfrac{k_1}{k_1^2+\lambda_1^2}\,{}^3V_{W_Z}\right) \\ -\dfrac{1}{d_4}\,{}^3V_{W_X} + \dfrac{k_2}{k_2^2+\lambda_2^2}\left(\dfrac{a_2 s_3 - d_4}{a_2 d_4}\,{}^3V_{W_Y} - \dfrac{d_3}{a_2 d_4}\,{}^3V_{W_Z}\right) \end{bmatrix} \quad (3\text{-}29)$$

the forearm joints velocities $\hat{\dot{\theta}}_A$ are only related to the translation velocities.

Through equation(3-30), the joint velocities of the wrist joints can be resolved as

$$\dot{\theta}_W = ({}^0J_{22})^{-1} \cdot ({}^0\Omega_W - {}^0J_{21}\dot{\theta}_A) \quad (3\text{-}31)$$

where $\dot{\theta}_A$ has been estimated as $\hat{\dot{\theta}}_A$ from (3-29). Using the frame transformation ${}^0J_{22} = {}^0R_5 \cdot {}^5J_{22}$, we can get a simpler form of ${}^5J_{22}$

$${}^5J_{22} = \begin{pmatrix} s_5 & 0 & 0 \\ c_5 & 0 & 1 \\ 0 & 1 & 0 \end{pmatrix} \quad (3\text{-}32)$$

Then the inverse of matrix has a simpler expression

$$\begin{aligned} ({}^5J_{22})^{-1} &= \frac{1}{s_5} \cdot \begin{pmatrix} 1 & 0 & 0 \\ 0 & 0 & s_5 \\ -c_5 & s_5 & 0 \end{pmatrix} \\ &= \frac{1}{k_3} \cdot \begin{pmatrix} 1 & 0 & 0 \\ 0 & 0 & k_3 \\ -c_5 & k_3 & 0 \end{pmatrix} \end{aligned}$$

where $k_3 = s_5 = 0$ is the wrist singularity. Thus

$$\hat{\dot{\theta}}_W = ({}^0J_{22})^{-1} \cdot ({}^0\Omega_W - {}^0J_{21}\hat{\dot{\theta}}_A) = ({}^5J_{22})^{-1} \cdot {}^5\Omega_W \quad (3\text{-}33)$$

therefore from equation (3-24)

$${}^5\Omega_W = {}^5R_0 \cdot ({}^0\Omega_W - {}^0J_{21} \cdot \hat{\dot{\theta}}_A) = ({}^0R_5)^T \cdot ({}^0\Omega_W - {}^0J_{21} \cdot \hat{\dot{\theta}}_A) \quad (3\text{-}34)$$

The estimated wrist joint velocity vector $\hat{\dot{\theta}}_W$ is

$$\hat{\dot{\theta}}_W = \begin{bmatrix} \hat{\dot{\theta}}_4 \\ \hat{\dot{\theta}}_5 \\ \hat{\dot{\theta}}_6 \end{bmatrix} = \begin{bmatrix} \dfrac{k_3}{k_3^2 + \lambda_3^2} \, {}^5\Omega_{W_X} \\ {}^5\Omega_{W_Z} \\ -\dfrac{k_3}{k_3^2 + \lambda_3^2} \cdot c_5 \cdot {}^5\Omega_{W_X} + {}^5\Omega_{W_Y} \end{bmatrix} \tag{3-35}$$

the wrist joints velocities $\hat{\dot{\theta}}_W$ are derived from rotation velocities and damped $\hat{\dot{\theta}}_A$, this will cause the error accumulation.

The damped factor λ_i ($i = 1,2,3$) can be chosen with respect to the three types of singularity

$$\lambda_i^2 = \begin{cases} \lambda_0^2 \cdot (1 - \dfrac{|k_i|}{w_i})^2 & 0 \le |k_i| \le w_i, i = 1,2,3 \\ 0 & otherwise \end{cases} \tag{3-36}$$

where λ_0 and w_i are fixed empirical value in the actual control computation.

3.2.5 Error Analysis

When the movement of the robotic arm encounters the singularity, the damped factors are applied. We have to evaluate the error between desired Cartesian velocities and computed joint velocities.

3.2.5.1 For Damped Least Square Method

The estimated Cartesian velocity $\hat{\dot{x}}$ is

$$\begin{aligned} \hat{\dot{x}} = J \cdot \dot{\theta}_d &= (\sum_{i=1}^{r} \rho_i \, \mathrm{u}_i \mathrm{v}_i^T) \cdot (\sum_{i=1}^{m} \frac{\rho_i}{\rho_i^2 + \lambda^2} \mathrm{v}_i \, \mathrm{u}_i^T \, \dot{x}) \\ &= \sum_{i=1}^{r} \frac{\rho_i^2}{\rho_i^2 + \lambda^2} \mathrm{u}_i \cdot \mathrm{u}_i^T \dot{x} \end{aligned} \tag{3-37}$$

The error between the actual and estimated translation velocity is

$$e = \dot{x} - \hat{\dot{x}} = \dot{x} - J \cdot \dot{\theta}_d = \sum_{i=1}^{r} \frac{\lambda^2}{\rho_i^2 + \lambda^2} \mathrm{u}_i \cdot \mathrm{u}_i^T \dot{x} \tag{3-38}$$

If $\dot{x}$ is projected to the U space, $\dot{x}$ can be expressed through the basis $u_1, \ldots, u_n$ as

$$\dot{x} = \sum_{i=1}^{m} \alpha_i \, \mathrm{u}_i$$

Then $e = \sum_{i=1}^{r} \frac{\lambda^2}{\rho_i^2 + \lambda^2} \alpha_i \, \mathrm{u}_i$.

3.2.5.2 For Singularity Separation Damped Reciprocal Method

From equation (3-29) and(3-31), the estimated translation velocities ${}^3\widehat{V}_W$ are

$$\begin{bmatrix} {}^3\widehat{V}_{W_X} \\ {}^3\widehat{V}_{W_Y} \\ {}^3\widehat{V}_{W_Z} \end{bmatrix} = \begin{bmatrix} -d_3 c_{23} & a_2 s_3 - d_4 & -d_4 \\ d_3 s_{23} & a_2 c_3 & 0 \\ -(d_4 s_{23} - a_2 c_2) & 0 & 0 \end{bmatrix} \begin{bmatrix} \dot{\widehat{\theta}}_1 \\ \dot{\widehat{\theta}}_2 \\ \dot{\widehat{\theta}}_3 \end{bmatrix}$$

$$= \begin{bmatrix} {}^3V_{W_X} + \frac{d_3(a_2 c_{23} k_1 \lambda_2^2 + k_2 \lambda_1^2)}{a_2(k_1^2 + \lambda_1^2)(k_2^2 + \lambda_2^2)} \, {}^3V_{W_Z} \\ \frac{k_2^2}{(k_2^2 + \lambda_2^2)} \, {}^3V_{W_Y} - \frac{d_3 s_{23} k_1 \lambda_2^2}{(k_1^2 + \lambda_1^2)(k_2^2 + \lambda_2^2)} \, {}^3V_{W_Z} \\ \frac{k_1^2}{(k_1^2 + \lambda_1^2)} \, {}^3V_{W_Z} \end{bmatrix} \qquad (3\text{-}39)$$

The translation velocity errors are

$${}^3e_{W_X} = {}^3V_{W_X} - {}^3\widehat{V}_{W_X} = -\frac{d_3(a_2 c_{23} k_1 \lambda_2^2 + k_2 \lambda_1^2)}{a_2(k_1^2 + \lambda_1^2)(k_2^2 + \lambda_2^2)} \, {}^3V_{W_Z}$$

$${}^3e_{W_Y} = {}^3V_{W_Y} - {}^3\widehat{V}_{W_Y} = \frac{\lambda_2^2}{(k_2^2 + \lambda_2^2)} \, {}^3V_{W_Y} + \frac{d_3 s_{23} k_1 \lambda_2^2}{(k_1^2 + \lambda_1^2)(k_2^2 + \lambda_2^2)} \, {}^3V_{W_Z}$$

$${}^3e_{W_Z} = {}^3V_{W_Z} - {}^3\widehat{V}_{W_Z} = \frac{\lambda_1^2}{(k_1^2 + \lambda_1^2)} \, {}^3V_{W_Z}$$

Similarly from equation(3-35), the estimated rotation velocities ${}^5\widehat{\Omega}_W$ are

$$\begin{bmatrix} {}^5\widehat{\Omega}_{W_X} \\ {}^5\widehat{\Omega}_{W_Y} \\ {}^5\widehat{\Omega}_{W_Z} \end{bmatrix} = {}^5J_{22} \cdot \begin{bmatrix} \dot{\widehat{\theta}}_4 \\ \dot{\widehat{\theta}}_5 \\ \dot{\widehat{\theta}}_6 \end{bmatrix} = \begin{pmatrix} s_5 & 0 & 0 \\ c_5 & 0 & 1 \\ 0 & 1 & 0 \end{pmatrix} \cdot \begin{bmatrix} \dot{\widehat{\theta}}_4 \\ \dot{\widehat{\theta}}_5 \\ \dot{\widehat{\theta}}_6 \end{bmatrix} = \begin{bmatrix} \frac{k_3^2}{k_3^2 + \lambda_3^2} \, {}^5\Omega_{W_X} \\ {}^5\Omega_{W_Y} \\ {}^5\Omega_{W_Z} \end{bmatrix} \qquad (3\text{-}40)$$

The rotation velocity errors are

$${}^5e_{W_X} = {}^5\Omega_{W_X} - {}^5\widehat{\Omega}_{W_X} = \frac{\lambda_3^2}{k_3^2 + \lambda_3^2} \, {}^5\Omega_{W_X}$$

$${}^5e_{W_Y} = {}^5\Omega_{W_Y} - {}^5\widehat{\Omega}_{W_Y} = 0$$

$$ {}^{5}e_{W_Z} = {}^{5}\Omega_{W_Z} - {}^{5}\widehat{\Omega}_{W_Z} = 0 $$

When $k_1 \to 0$, $\lambda_2 \to 0$, the translation velocity errors are

$$ {}^{3}e_{W_X} = -\frac{d_3\lambda_1^2}{a_2(k_1^2+\lambda_1^2)k_2}\,{}^{3}V_{W_Z} $$

$$ {}^{3}e_{W_Y} = 0 $$

$$ {}^{3}e_{W_Y} = \frac{\lambda_1^2}{(k_1^2+\lambda_1^2)}\,{}^{3}V_{W_Z} $$

When $k_2 \to 0$, $\lambda_1 \to 0$, this is the **Type I** singularity. As previous description, the rotation velocity errors are

$$ {}^{3}e_{W_X} = -\frac{d_3c_{23}\lambda_2^2}{k_1\,(k_2^2+\lambda_2^2)}\,{}^{3}V_{W_Z} $$

$$ {}^{3}e_{W_Y} = \frac{\lambda_2^2}{(k_2^2+\lambda_2^2)}\,{}^{3}V_{W_Y} + \frac{d_3s_{23}\lambda_2^2}{k_1\,(k_2^2+\lambda_2^2)}\,{}^{3}V_{W_Z} $$

$$ {}^{3}e_{W_Y} = 0 $$

3.2.5.3 Results and Discussion

In simulation for these two numerical methods, the first case of movement of the end-effector was the translation along Y axis at 0.25 m/s, the second case of movement of the end-effector was the rotation around X axis at 0.25 rad/s. The initial robot arm joint position was $\theta = [\pi/6, \pi/4, 0, \pi/4, 0, \pi/2]$ and the damping factors were selected as $\lambda_0 = 0.1$ and $w = 0.1$. The error of the Cartesian velocity is defined as

$$ \begin{aligned} e &= \left\| \dot{p} - \hat{\dot{p}} \right\|_2 \\ &= \left\| \dot{p} - J \cdot \hat{\dot{\theta}} \right\|_2 \end{aligned} \tag{3-41} $$

where Cartesian position of end-effector is $p = [x, y, z, \alpha, \gamma, \beta]$ and the Cartesian velocity is $\dot{p} = [\dot{x}, \dot{y}, \dot{z}, \dot{\alpha}, \dot{\beta}, \dot{\gamma}] = [\dot{x}, \dot{y}, \dot{z}, \Omega_x, \Omega_y, \Omega_z]$.

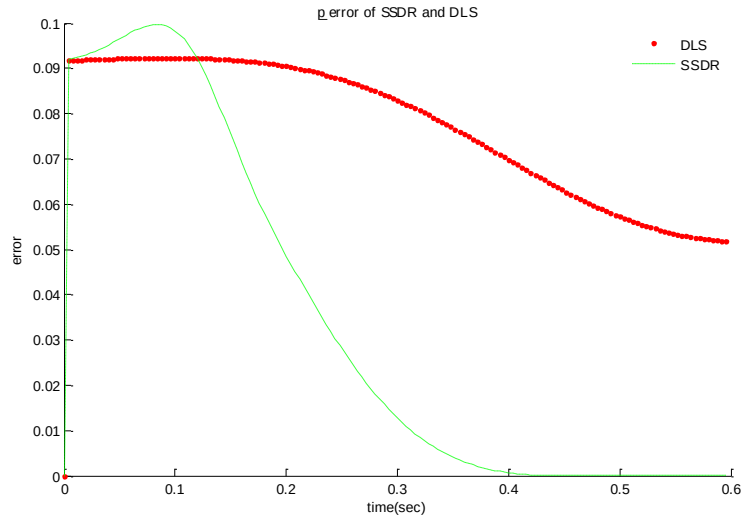

Figure 3.9.Error comparison of DLS and SSDR method by translation along Y axis at 0.25 m/s.

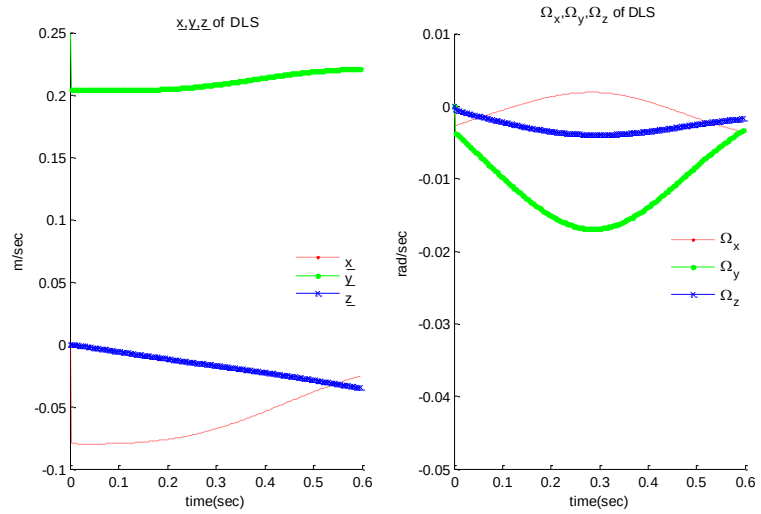

(a) Cartesian velocity with DLS

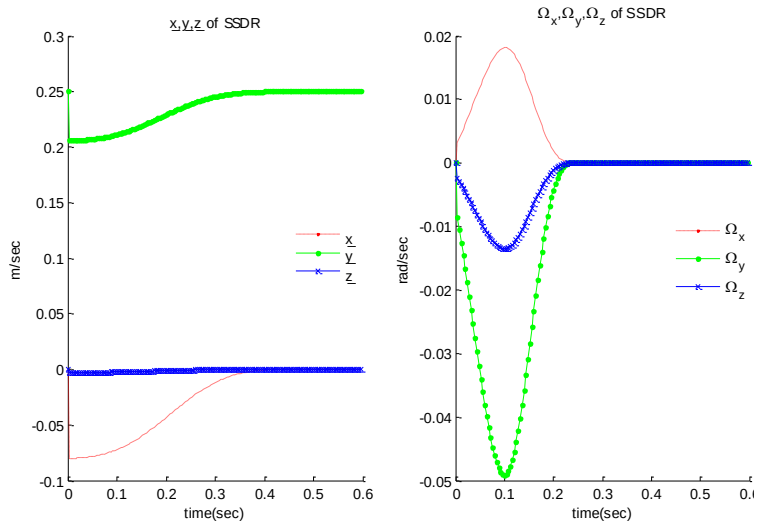

(b) Cartesian velocity with SSDR

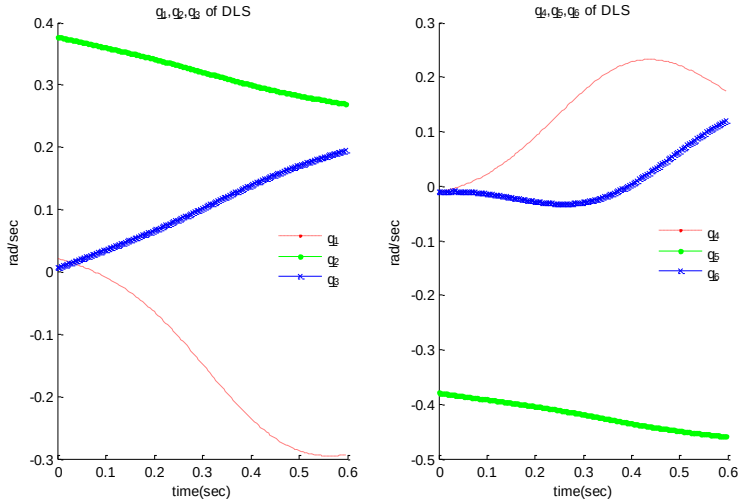

(c) Joint velocity with DLS

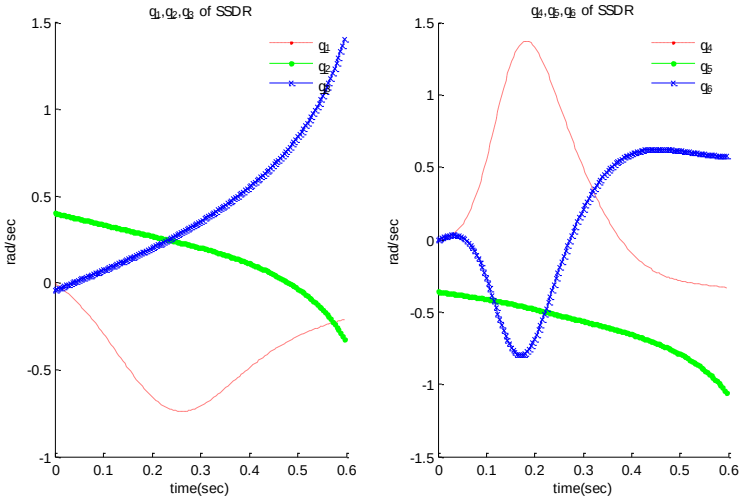

(d) Joint velocity with SSDR

Figure 3.10.Cartesian velocity and joint velocity of robot arm of DLS ((a) and (c)) and SSDR ((b) and (d)) methods with translation along Y axis at 0.25 m/s.

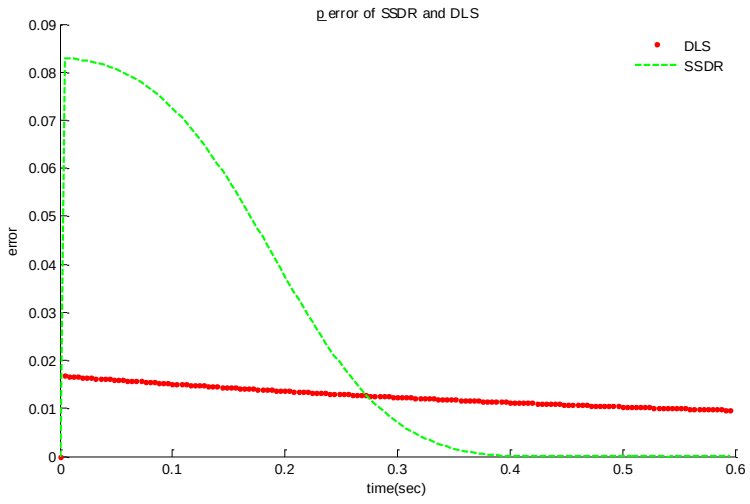

Figure 3.11. Error comparison of DLS and SSDR methods by rotation along X axis at 0.25 rad/s.

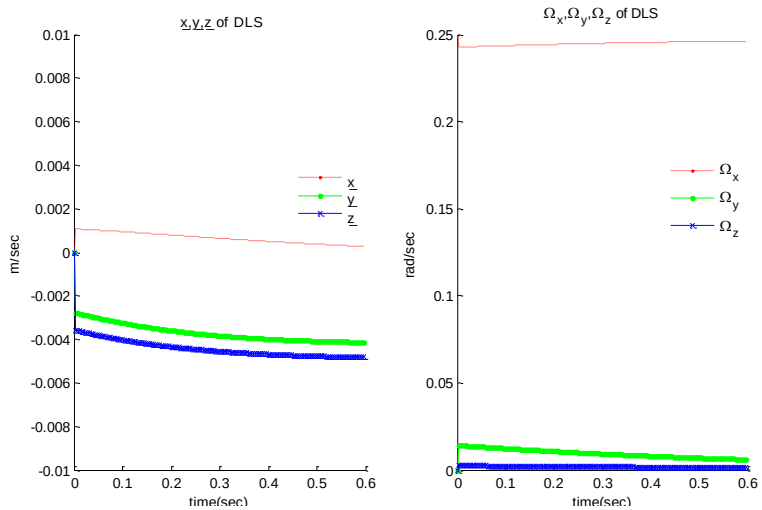

(a) Cartesian velocity with DLS

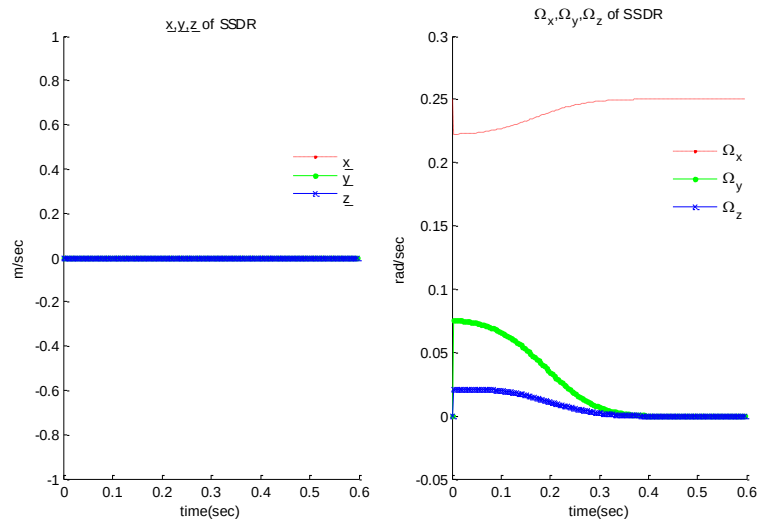

(b) Cartesian velocity with SSDR

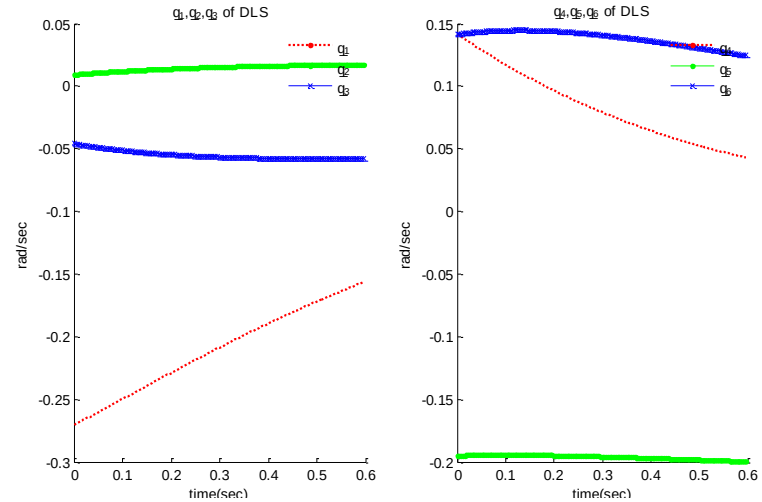

(c) Joint velocity with DLS

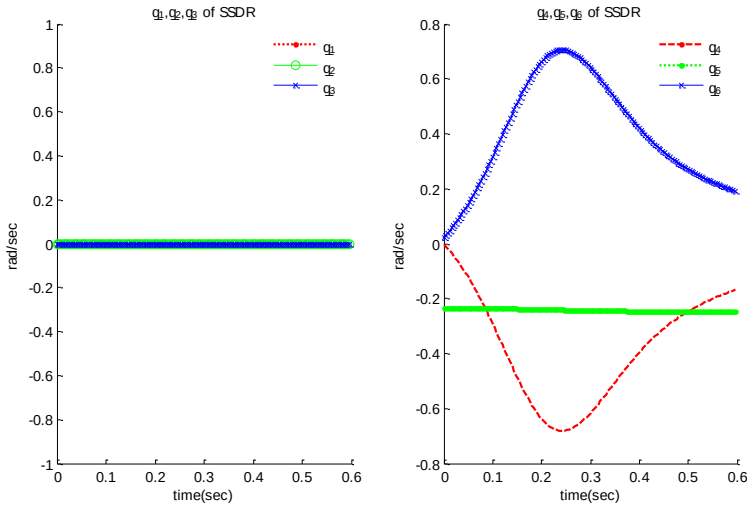

(d) Joint velocity with SSDR

Figure 3.12.Cartesian velocity and joint velocity of robot arm of DLS((a) and (c)) and SSDR((b) and (d)) methods with rotation along X axis at 0.25 rad/s.

The DLS method uses the global damping factor λ to damp the Jacobian matrix when solving inverse problem. However, the DLS needs the inverse operation and decomposition of Jacobian matrix. By contrast, the SSDR method uses different strategies to damp different parts of Jacobian matrix and gives explicit expression. From the results of simulation, not only could this method improve the accuracy, but also it was appropriate for real-time computation. From Figure 3.9 to Figure 3.12, SSDR method generated fluctuation on Cartesian and joint velocity in the singularity region. However, the error reduced quickly when leaving this region, because wrist joints solution $\dot{\hat{\theta}}_W$ were derived from the estimated forearm joints solution $\dot{\hat{\theta}}_A$ which would cause error accumulation.

Chapter 4. Cooperative Control Algorithm Design

4.1 Introduction

Because of the advanced technology used, the actions of robot are considered more precise and dexterous than of human. However, in the unstructured environments, when implementing the complex task, the robots are restricted because of the limitations of artificial intelligence. In this case, the control law should involve the human's intervention, and the control is shared by the robot and human operator. During the execution of task, this shared-control concept defines the human-machine collaborative system with human "in the control loop". However, the control strategy with human in loop produces additional problems that the tremor and fatigue may greatly affect the accuracy and completion time.

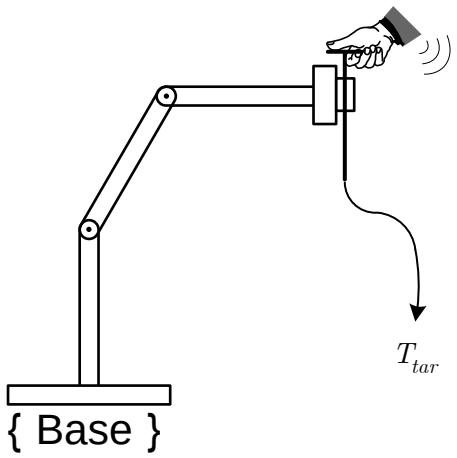

Figure 4.1. Demonstration of the human-machine collaborative system, 3 links robot is equipped with force/torque sensor which can be applied force and torque by user, the curve is the desired trajectory and T_{tar} is the target.

As illustrated in the Figure 4.1, when the user applies force/torque on the end-effector of the robot, the critical control problem is to guide the robot to move along the desired path while preventing the motion in undesired directions and regions in the workspace. In recent research, the concept of virtual fixture, which is the program generated motion guidance and constraint method, was widely explored and applied in the robotic assisted surgery. Virtual fixture was presented by Rosenberg[82] for the first time with analogy to a ruler as a physical fixture to help user drawing a straight line faster and more accurately, meanwhile leaving the user with the freedom to override the assistance if desired. In the tele-robotic system, Rosenberg implemented virtual fixtures like impedance surface on the master to assist in peg-in-hole tasks[82].

Based on JHU Steady-Hand Robot, a 7 DoF robot equipped with a force sensing handle at the endpoint, Funda,et al [83]defined basic classes of virtual fixtures from desired motion in any number of coordinate frames relevant to the task, and optionally subject to additional linear constraints in each of the frames for redundant and deficient robots. Li,et al [84]extended Funda's work[83] to define a library of virtual fixtures for real-time obstacle avoidance, and simultaneously assist the surgeon to perform tool movement along desired trajectory by using an optimization-based approach.

In Li's work [84], the movement of the end-effector of a robot is under the position control and the desired joint angle solution should be solved through the complex second order cone program online, therefore, this algorithm costs much more computation. From another viewpoint, similarly based on the Steady-Hand Robot, Bettini,et al [85] and Marayong,et al [86] extended the general admittance control law to develop guidance virtual fixtures to assist the surgeons in order to move the surgical instruments along the desired direction. Their work was focused on 2D geometric guidance motion of the tool tip based on vision information, the robot is under the velocity control and less computation is obtained in real-time.

In this chapter, we propose a scheme and simulation system which can be used to evaluate the effect of guidance virtual fixture based on the haptic device (Phantom Desktop™) and virtual robot model in the MATLAB environment.

4.2 Mathematic Description of Virtual Fixtures

4.2.1 Virtual Fixture Control Law

In the Cartesian coordinate, for rigid robot system, the desired end-effector velocity is $v = [\dot{p}, \dot{r}] \in \mathbb{R}^6$, where $p = [x, y, z]$ is the position and $r = [\alpha, \beta, \gamma]$ is the orientation of end-effector in the robot's base frame. From the general admittance control law

$$v = c \cdot v_{op} \tag{4-1}$$

where v_{op} is the input velocity of operator. If the input of operator is in other form such as a force or position, it has to be converted to velocity as input, by linear scaling the force or making differentiation of the position. The scalar $c > 0$ is the coefficient for the isotropic compliance along all dimensions of the v. If the anisotropic compliance for the different dimensions needed, the diagonal matrix C should be involved.

Then the end-effector of robot will follow the user's input action, meanwhile it perform different compliance in 3D translation and 3D orientation. However, owing to tremor, fatigue and unskillful operation of the user, the motion under general admittance control as equation (1) will not always follow the user's intention but with disturbance and offset. We call the user's desired intention as the preferred direction with high compliance and the remaining as the non-preferred direction.

4.2.2 Guidance Virtual Fixture (GVF)

If Cartesian coordinate is specified, all directions or geometry constraints could be divided to two parts: translation part $p = [x, y, z] \in \mathbb{R}^3$ and rotation part $r = [\alpha, \beta, \gamma] \in \mathbb{R}^3$. Therefore, virtual fixture along the preferred direction can be separated into two parts: translation and rotation. A subspace U, containing all preferred directions for both translation and rotation, can be defined. Let $S^p \; and \; S^r$ be two subsets of $\mathbb{R}^3$ comprising the linear independent set of vectors that span U for translation and rotation respectively.

$$S^p = \; p_1,\ldots,p_k \tag{4-2}$$

$$S^r = \; r_1,\ldots,r_l \tag{4-3}$$

where the $p_i (i = 1 \cdots k)$ is the unit vector along the specific direction, S^p is the translation part, $r_i (i = 1 \cdots l)$ is the specific unit rotation axis and S^r is the rotation part of the preferred direction. Since three linear independent vectors can span the whole $\mathbb{R}^3$ space with $k, l \leq 3$. Then a time-varying matrix $D = D(t)$ can be used to indicate the instantaneous preferred direction at time t. Matrix D comprises the subsets S^p and S^r as

$$D = \begin{bmatrix} S^p & 0_{3\times l} \\ 0_{3\times k} & S^r \end{bmatrix} = \begin{bmatrix} (p_1,\ldots,p_k) & 0_{3\times l} \\ 0_{3\times k} & (r_1,\ldots,r_l) \end{bmatrix} \tag{4-4}$$

where $D(t) \in \mathbb{R}^{6\times n}, 0 < n \leq 6$ [87]. Different to Marayong's work[86], the translation and rotation parts are decoupled. If we only consider the translation part, when n=1, the D means the preferred direction along a curve in $\mathbb{R}^6$; when n=2, the D indi-

cates the directions that span a surface; when n=3, the D means the free translation in the $\mathbb{R}^6$ space. From the matrix D, two projection operators can be defined[86] as

$$Span(D) = \left[D \right] = D(D^T D)^{\dagger} D^T \tag{4-5}$$

$$Kernel(D) = \left\langle D \right\rangle = I - \left[D \right] \tag{4-6}$$

where $\left[D \right]$ and $\left\langle D \right\rangle$ are the span and kernel projection through the column space.

For the general cases, the D does not have full column rank and the span cannot be calculated, thus in equation (4-7) the pseudo-inverse $(D^T D)^{\dagger}$ was introduced[86]. The orthogonal projection $[D]$ acts as the identity of U, i.e. any vector x in this subspaces has $[D]x = x$. Otherwise, there exists an orthogonal complementary subspace V that contains all the non-preferred direction. Each vector x in V has $[D]x = 0$. V is null space equivalent to kernel of the projection. More detail properties of the operators $[D]$ and $\left\langle D \right\rangle$ are described in Ref.[86].

Then the user's input velocity v_{op} can be decomposed into two components as

$$v_U = \left[D \right] v_{op}, v_V = \left\langle D \right\rangle v_{op} \tag{4-8}$$

Thus equation (4-1) could be rewritten as

$$v = c \cdot v_{op} = c \cdot (v_U + v_V) \tag{4-9}$$

where v_U is along the preferred direction (in the U subspace), and v_V is along the non-preferred direction (in the V subspace). v_V is usually considered as the disturbance from the preferred direction and should be eliminated. So the equation (4-9) should be changed to

$$v_d = c_U \cdot (v_D + c_V \cdot v_\tau) = c_U \cdot (\left[D \right] + c_V \cdot \left\langle D \right\rangle) \cdot v_{op} \tag{4-10}$$

where $c_U, c_V \in [0,1]$ are the admittance coefficients, c_U is as same as c in the equation (1) and c_V attenuates the non-preferred component of the user's input velocity. With the new expression of v_d, virtual fixtures will generate guidance effect that helps the user to move the end-effector along a desired path or surface defined by U. These virtual fixtures are called guidance virtual fixtures (GVF). If $c_v = 0$, the motion in subspace V is completely eliminated, i.e. a hard guidance level only along U is present. If $c_V = 1$, it assumes that there is no distinction between preferred and non-

preferred directions. Therefore, no guidance and constraint are present. If $0 < c_V < 1$, there will generate the effect called *'soft guidance'*.

4.2.3 Guidance Virtual Fixture Generation

For constraining the motion to a given subspace, continuous time-varying $S^p(t)$ and $S^r(t)$ should be provided and then equation (4-9) is applied to yield the motion within that subspace.

For moving the end-effector towards a target pose $x_{tar} \in \mathbb{R}^6$ by using a control law $u = f(x, x_{tar})$ such that by setting the control input equal to u, the pose of end-effector will eventually converge to the target pose

$$\lim_{t \to \infty} x(t) = x_{tar} \tag{4-11}$$

By choosing $D(t) = u$ and applying equation(4-9), the control system will guide the user to the given desired pose.

4.3 Configuration of Simulation for GVF

4.3.1 Haptic Interface

In our simulation system, Phantom Desktop is used as the haptic device, which could sense the user-hand's 6 DoF input including 3 DoF translational and 3 DoF rotational motions. Meanwhile, 3 DoF translational force feedback is supported.

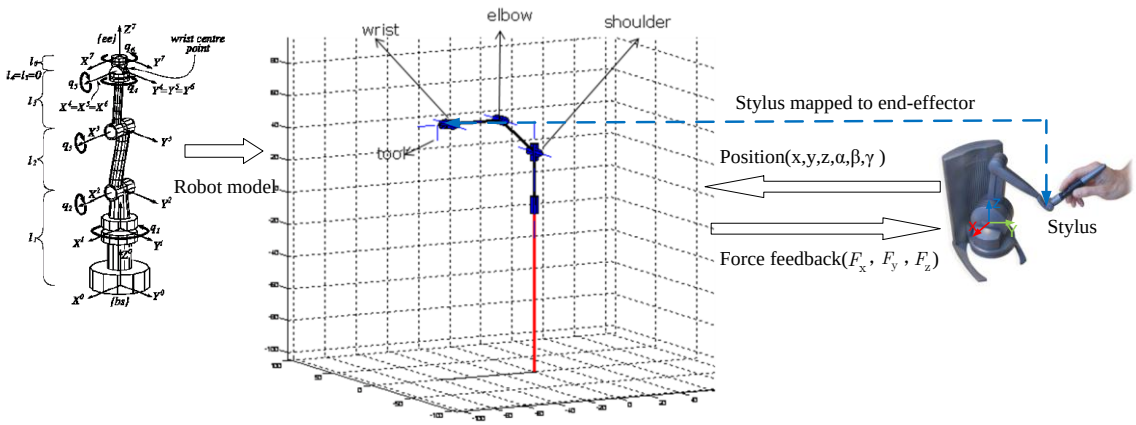

Figure 4.2. Haptic interface with robot model based on the Robotic Toolbox under MATLAB®.

Conventionally, development of virtual reality application with haptic device is always based on C++ or Java on computer; it is a complex task and needs a long time to implement even a simple algorithm. In our work, thanks to the ProkPhantom component[88], which is a .NET component designed as a middleware between

MATLAB software platform and Sensable Phantom® hardware platform. With this middleware, program to manipulate haptic device can be developed under MATLAB. Through ProkPhantom, the program can read the position of the haptic device or the force applied by haptic device in the sampling frequency (default 1 KHz), and send the target position and force command to the haptic device.

4.3.2 Virtual Robot Modeling

In this work, the Phantom Desktop acts as a master and we build a virtual slave robot through the Robotics Toolbox for MATLAB[89]. The toolbox provides many useful functions for robotic computation such as forward kinematics/inverse kinematics, dynamics/inverse dynamics and trajectory generation. Robotics Toolbox is useful for simulation as well as verifying results of experiment with real serial-link manipulators. In addition, the toolbox provides mathematical functions for vectors, homogeneous transformations matrix and unit-quaternions which are necessary to represent 3D position and orientation.

In Figure 4.2, a six DoF serial link robot is modeled in the toolbox based on the Stäubli TX60. Table 4–1 lists the modified Denavit-Hartenber parameters(MDH) [76]of the TX60.

Table 4–1. MDH parameters of TX60

i	α_{i-1}	a_{i-1}	d_i	θ_i
1	0	0	0	θ_1
2	$-\frac{\pi}{2}$	0	0	θ_2
3	0	a_2	d_3	θ_3
4	$-\frac{\pi}{2}$	0	d_4	θ_4
5	$\frac{\pi}{2}$	0	0	θ_5
6	$-\frac{\pi}{2}$	0	d_6	θ_6

With the given forward kinematic functions provided by Robotics Toolbox, we can get the position (x) and velocity ($\dot{x}$) of the end-effector in the Cartesian space from the pre-planned joint space:

(1) joint angle: $\theta = [\theta_1, \theta_2, \cdots, \theta_n]$ (n is the joint number of the robotic arm)

(2) joint angle velocity : $\dot{\theta} = [\dot{\theta}_1, \dot{\theta}_2, \cdots, \dot{\theta}_n]$

Similar with the inverse kinematic functions, we can get the θ and $\dot{\theta}$ from the given position (x) and velocity ($\dot{x}$) of the end-effector. More details about the programming using Robotics Toolbox[89].

Through the ProkPhantom middleware, the position and force of the haptic device can be obtained by MATLAB program. Thus, we can manipulate the virtual robot through haptic device. In the meantime, the trajectory following the movement of the operation can be displayed in the MATLAB by animation command.

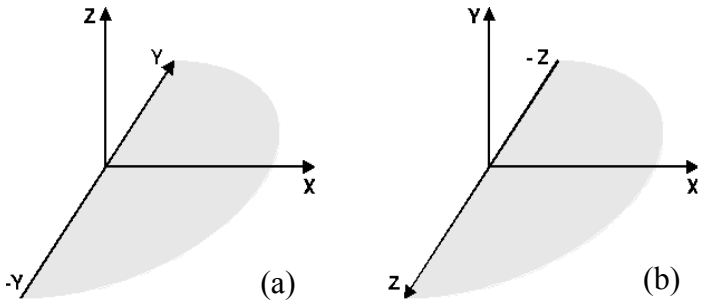

Figure 4.3. (a): MATLAB graphics coordinate. (b):Phantom Desktop coordinate

However, the position data read from ProkPhantom is the physical position of the haptic device (for Phantom Desktop, the workspace is 160 W×120 H×120 D mm)[90]. Besides, the coordinate of the haptic device is different from the coordinate of the MATLAB as shown in Figure 4.3. Thus we have to map the position of the haptic stylus from the coordinate of the haptic device to that of the MATLAB through

$$p_{vir} = \alpha \cdot T \cdot p_{haptic} \tag{4-12}$$

as registration, where the p_{haptic} is the position of the haptic stylus, T is the 4×4 homogeneous transformation matrix, α is the scale factor to balance the manipulation space between the workspace of haptic device and TX60 robot model in order not to excess the space limitation of the robot.

In Figure 4.4, the flow chart shows how to use the ProkPhantom to read from and write commands to the Phantom Desktop, the codes in the flow chart are MATLAB commands provided by the ProkPhantom. Initially, a handle pointed to the haptic device is created for writing command and reading status. When the “connect”

between middleware and haptic device is established, the program can communicate with the haptic device in MATLAB. The registration maps the physical position of the haptic device to the workspace of the robot.

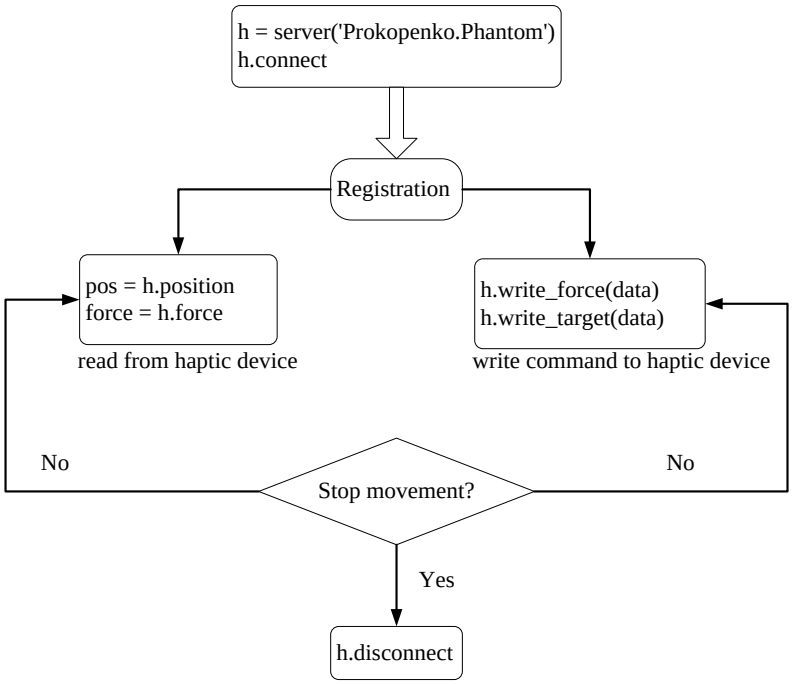

Figure 4.4. Flow chart of programming the haptic interface with the MATLAB®.

4.3.3 Force Feedback with GVF

Impedance force F_{imp} feedback to haptic device for user's guidance between virtual fixture and actual trajectory can be modeled as

$$F_{imp} = k_d \cdot (x_d - x) + k_v \cdot (\dot{x}_d - \dot{x}) \tag{4-13}$$

x_d is the position of virtual fixture, x is the position of the end-effector transformed from the coordinate of the haptic device. To apply guidance virtual fixture, the user's input velocity in (4-13), which can be force, position or velocity, should be transformed to the desired velocity v_{op}. In practice, v_{op} is set to $\dot{x}_d$ which is the differential of position computed in real-time.

4.4 Results and Discussion on Simulation

In the simulation, we tested two basic cases of the guidance virtual fixture: (1) move the end-effector along a line, (2) move the end-effector in specific plane. We compared the results of movement with and free of GVF.

4.4.1 Case 1: Move along a Line (One DoF)

A virtual fixture is created to move the end-effector along Z-axis while keeping the orientation constant. In this case, the definition of virtual fixture is $p_1 = [0,0,1]^T$, $S^p = \{p_1\}$, $S^r = \{0\}$ and $D = [0,0,1,0,0,0]^T$.The admittance coefficients are $c_U = 1$ and $c_V = 0.1$, different c_U and c_V will affect the compliance but not significant in this experiment.

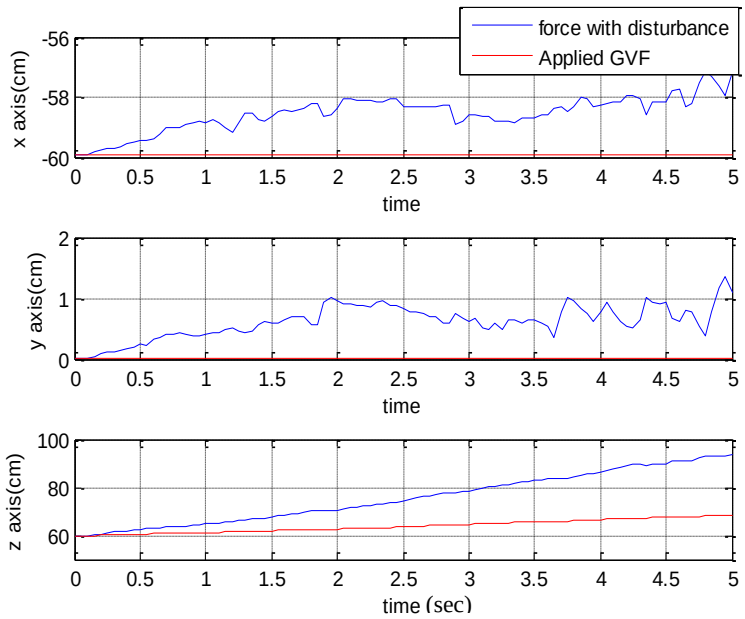

(a)

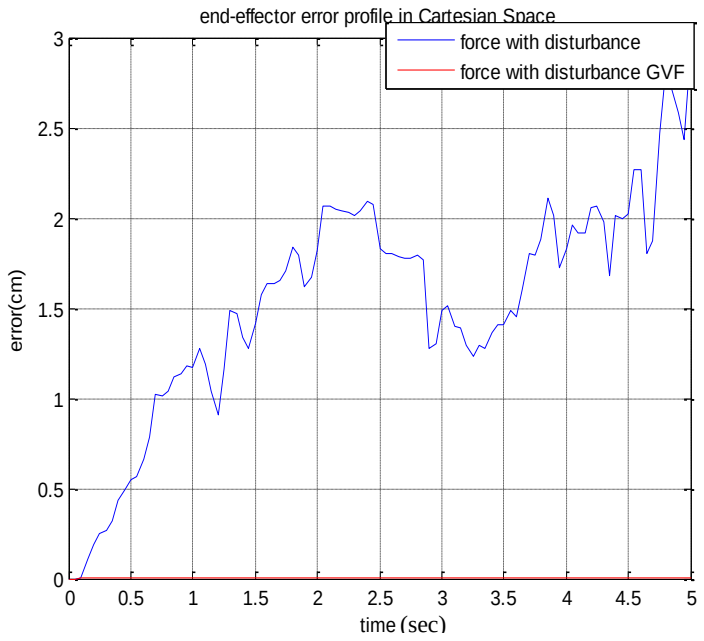

(b)

Figure 4.5. (a) X, Y and Z position of end-effector in Cartesian space. (b) Position error compared with and without GVF

The ideal path should be a line along Z-axis, thus when moving the end-effector, the x coordinate and y coordinate should not change, while the z coordinate should follow the movement. From the compared results in Figure 4.5, it is clearly found that the GVF guide the motion along the desired direction and the maximum position error $e = \left\| x_d - x \right\|_2$ is less than 0.74 mm.

When the user moves haptic device, the movement of the robot arm could be displayed in the screen and the joint angle and joint angle velocity could also be computed through the Robotics Toolbox. The result of the robot parameters is not given in this paper.

4.4.2 Case 2: Move in Plane (Two DoF)

The end-effector in the X-Y plane was moved along fold lines parallel to X and Y axes (the blue solid lines in Figure 4.7). When there is no disturbance, the movement along Z axis should not change while following the X and Y axis (shown in Figure 4.6.(a) and Figure 4.7). The definition of the virtual fixture for a plane in the U subspace is more complicate, but the definition of the V subspace is easier. For each plane, it has an unique norm vector n which is the orthogonal complementary of this plane[91], thus the equation (5) and (6) can be changed to

$$\left\langle D \right\rangle = D_V (D_V{}^T D_V)^{\dagger} D_V{}^T \tag{4-14}$$

$$\left[D \right] = I - \left\langle D \right\rangle \tag{4-15}$$

where $D_V = [n,0,0,0]^T$, for the X-Y plane, $n = [0,0,1]^T$ is the norm vector.

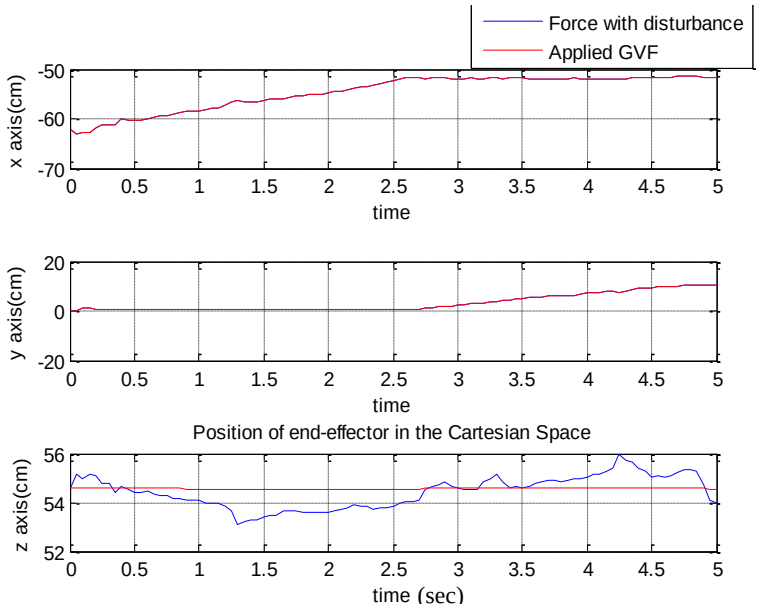

(a)

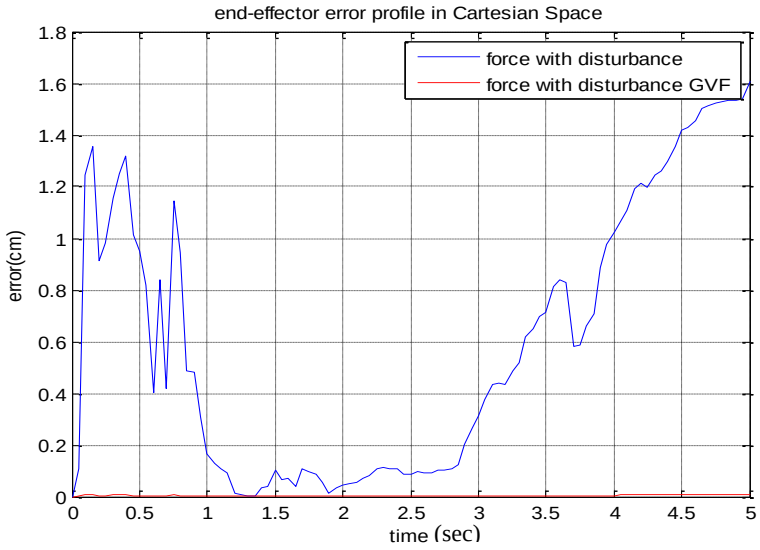

(b)

Figure 4.6.(a)X, Y and Z position of end-effector in Cartesian space. (b) Position error compared with and without GVF.

In Figure 4.6 (b) and Figure 4.7, the red line is the motion applied GVF and the blue one is free of GVF. From these two figures, the movement applied GVF is constrained in the X-Y plane with the maximum position error less than 1.45 mm.

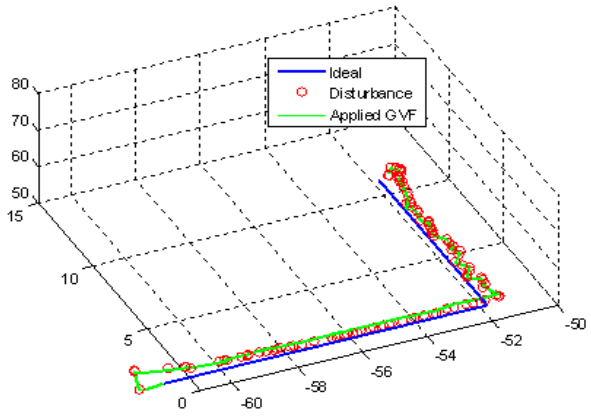

Figure 4.7. End-effector trajectory. Blue line is the ideal path; red circle is the movement without GVF, green line is the path applied GVF.

Chapter 5. Force Sensing and Finite Element Analysis for Bone Drilling Process

5.1 Introduction

In modern orthopedic surgery, before using nails, plates and screws for fracture fixation and joint replacement, various bone machining operations, e.g. drilling, milling and cutting, are required. Development of suitable surgical tools for reducing damage on the bone is significant[92, 93].

For surgical drilling on bone, whatever semi-automatic or manual operation, measurement of drilling force and torque are critical requirements for safety enhancement. The key point is detection of drill bit break-through to protect soft tissue and nerves surrounding the drilling hole. For this purpose, in this chapter, we discuss some techniques for force sensing in the robotic assisted orthopedic surgery system. This chapter includes two parts:

1. In section 5.4, we recorded the force/torque information of drilling bone and implement the real-time detection of drill bit break-through based on discrete wavelet transform.
2. In section 5.5, besides the signal processing techniques, drilling bone process was simulated based on 3-dimension finite element modeling (FEM) and analysis (FEA). Not only do FEM and FEA evaluate force and temperature distribution on the surgical tool and bone, but the methods provide the direct visual display of surgical drilling process.

5.2 Force Profile of Bone Drilling

Human's bones are rigid organs that form parts of the endoskeleton. Bones can support and protect the organs of the body, produce red and white blood cells and store minerals. Bone tissue is dense connective tissue, which is lightweight but strong and hard, with a variety of shapes and complex structure. Main ingredient of bone is the mineralized osseous tissue which makes bone rigid and a coral-like three-dimensional internal structure which makes bone porous. Other types of tissue found in bones include marrow, nerves, blood vessels, endosteum, periosteum and cartilage[94]. The anatomical structure of femur bone is shown in Figure 5.1.

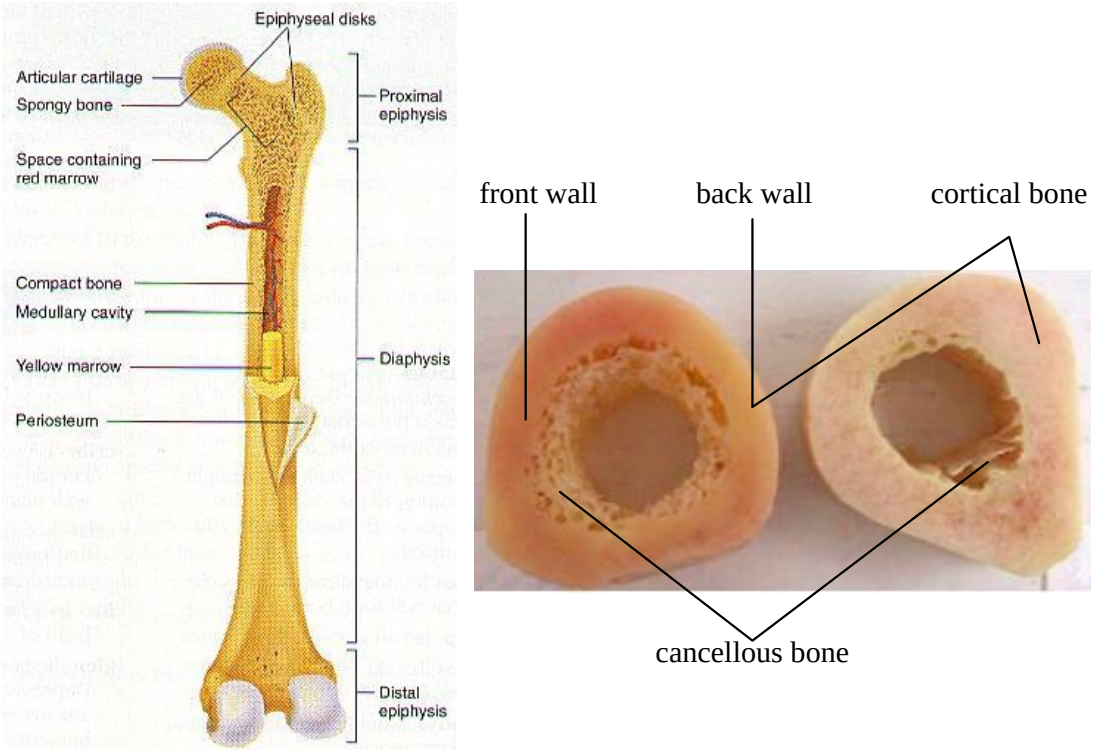

(a) femur shaft (b) slices of femur

Figure 5.1. Femur shaft and slices. The interior of a typical long bone showing the growing proximal end with a growth plate and a distal end with the epiphysis fused to the metaphysis[95].

While drilling bone, the thrust force F_t exerted by the twist drill bit on the bone can simply be modeled as[96]

$$F_t = K_s \cdot a \cdot \frac{D}{2} \sin \frac{\beta}{2} \tag{5-1}$$

where K_s is the total energy per unit volume required to cut the material, a is the feed rate expressed in unit length/revolution, D is the diameter of the drill bit, and β is the convex angle between the main cutting lips(see Figure 5.2.(a)).

The feed rate can be expressed as a function of the rotational speed ω of the drill bit and the feed rate v_f as

$$a = 2\pi \cdot \frac{v_f}{\omega} \tag{5-2}$$

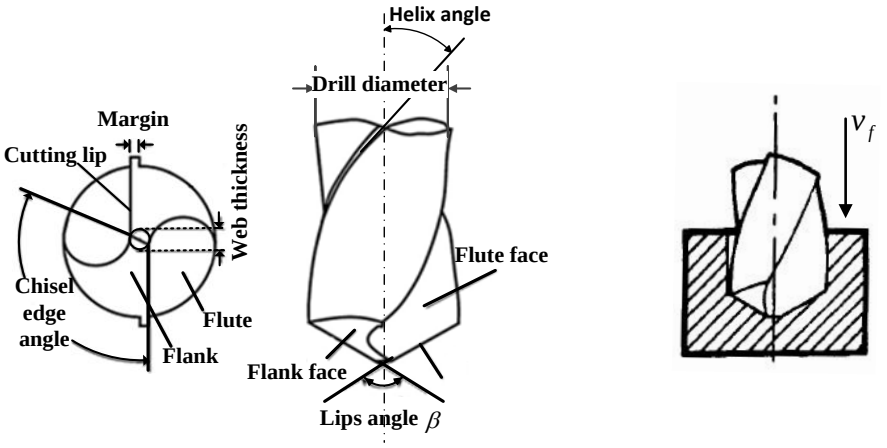

Figure 5.2. (a) Twist drill geometry (b) Drilling process of twist drill bit in single material layer.

When the drill bit penetrated into the material (see Figure 5.2. (b)), F_t could be considered as constant. While the drill bit was about to break through the material, the contact area between drill bit and material would decrease thus making F_t decrease as well.

Owing to the hollow structure of femur, the drilling process consists of three successive stages: (1). Penetration the front wall of cortical wall, (2). Penetration into the yellow marrow, (3). Break through the back wall of cortical wall. Detection of break-through and stop drilling during the stage 3 is to prevent damage for further penetration. Figure 5.3 shows above three stages and the drilling force profile under v_f =1.25 mm/s, ω =60 mm/min with D =3.2 mm and β = 120 of twist drill bit. The sudden fall of force can be considered as the break-through. Ong,et al [97] reported that because the compliance of the fixation on the distal femur and the flexibility of long bone, the recorded drilling force would perform low-stiffness of bone which was called "spring-back" effect. However, in our experiment, we found that the low-stiffness effect was trivial and could be ignored.

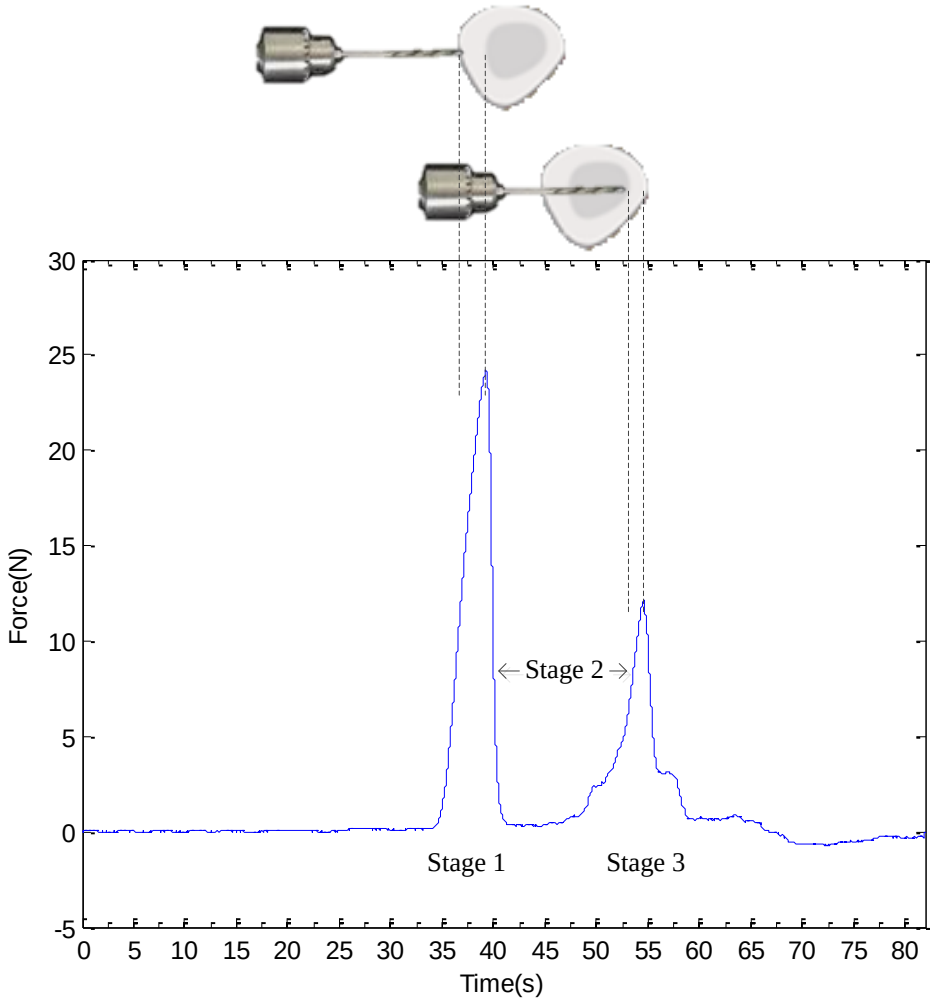

Figure 5.3. Process of drilling through a porcine femoral shaft. Stage 1 is drilling through the front cortical wall. Stage 2 is penetration into the yellow marrow. Stage 3 is drilling through the back cortical wall.

Different force measurements were recorded in Figure 5.4 under v_f =1.2 mm/s and 12.5 mm/s with ω = 600 rpm and diameter 3.2mm of twist drill bit. The magnitudes of those two force profiles show the approximate linearity on the feed rate through equation(5-1).

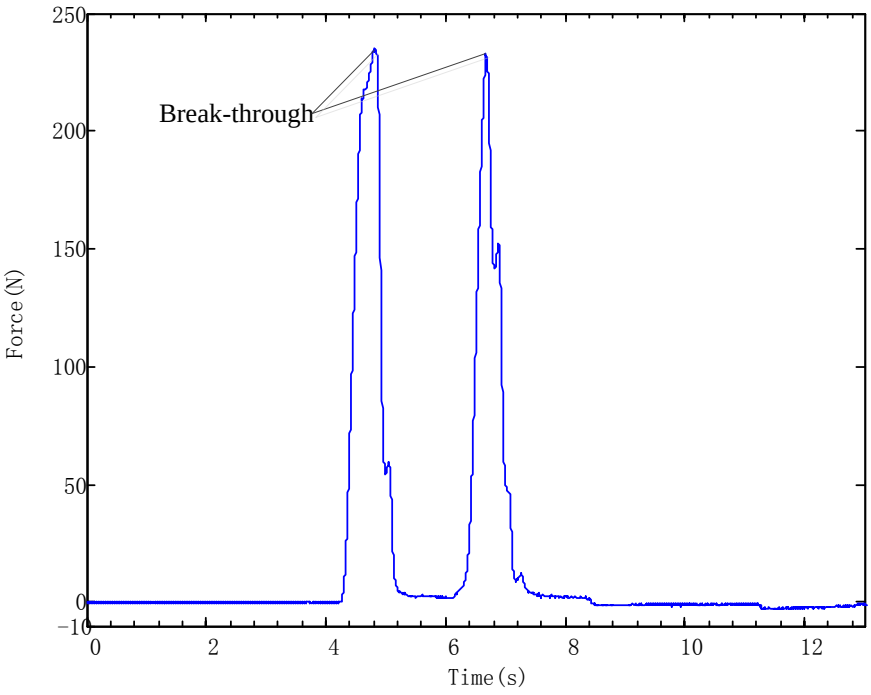

(a) Feed rate = 12.5 mm/s, rotation speed = 600 rpm

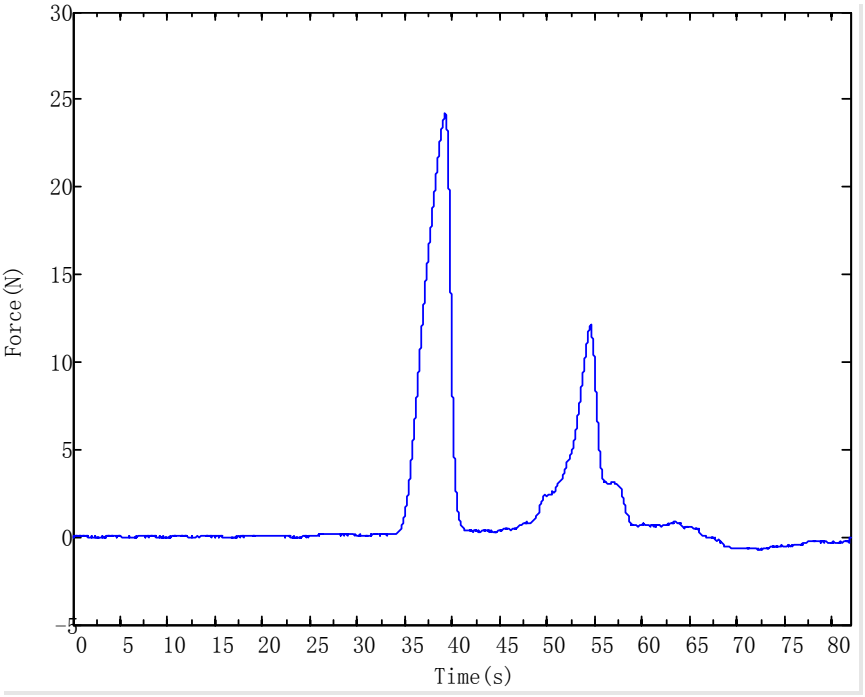

(b) Feed rate = 1.25 mm/s, rotation speed = 600 rpm

Figure 5.4. Profile of drilling force under different feed rate and fixed rotation speed.

5.3 Force Sensing Experiment

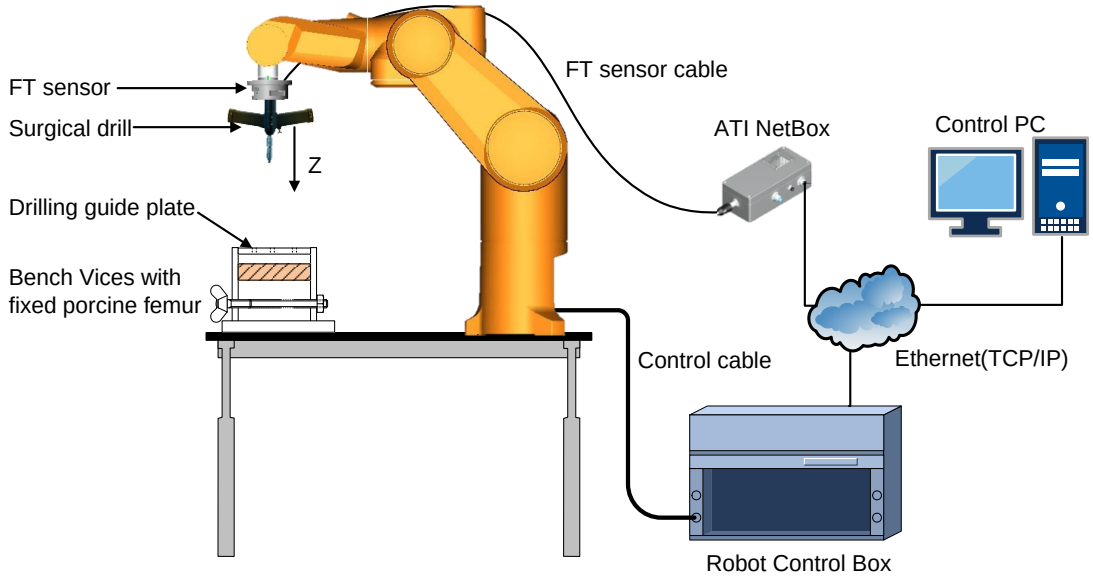

Figure 5.5. Force sensing experiment setup based on the robotic assisted orthopedic surgery system.

A six DoF robot arm (Stäubli TX60) for hyper-clean application is adopted in this system. The robot can approach 0.1mm accuracy along 3 dimensions of translation and rotation[98]. The movement of robot can be controlled by VAL3 program loaded in the Robot Control Box which can get command and feedback robot's status with remote computer via Ethernet[99]. ATI F/T transducer mini85 is mounted on the end-effector of robot arm for measuring multi-axis Force/Torque while drilling. The ATI NetBox is a portable device used to process and communicate the transducer's force and torque readings to the user's computer via Ethernet[100]. The NetBox can get power supply and implement data communication through one piece of LAN cable, thus it is convenient for various applications. Clinical surgical drill, which can be sterilized by hydrogen peroxide and provide high rotation power with fixed rotation speed 600 rpm, is used for drilling bone. The weight of surgical drill is removed through Bias function of F/T transducer before measuring, the drill bit moves along Z direction with one DoF. Two pieces of fresh porcine femur, with muscle and fat removed, are tested as surgical objects in the experiment.

5.4 Wavelet-based Real-time Detection of Drill Bit Breakthrough

For detection of break-through, Brett,et al [101] used sample window, which identified persistent increment in the torque over six sample periods while the force decreased. Colla,et al [102] used the wavelet transform of the drilling force and se-

lected the wavelet coefficients on specific scale for threshold classification. However, the complex structure and geometry of the femur bone will cause disturbance on the signal. Therefore, to reduce the disturbance interference, in this research, search of maxima modulus on different wavelet transformation scales is adopted for break-through detection.

5.4.1.1 Wavelet Transform

Wavelet transform (WT) is known as a useful tool for non-stationary and time-frequency signal processing. WT is a linear operator which can decompose the signal $f(t)$ into components with different resolutions [103, 104].

$\psi(t) \in L(\mathbb{R}^2)$ is wavelet function if and only if its fourier transform $\hat{\psi}(\omega)$ satisfies

$$\int_{-\infty}^{+\infty} \frac{\left|\hat{\psi}(\omega)\right|^2}{\left|\omega\right|} d\omega < \infty \tag{5-3}$$

This admissibility condition implies that $\psi(t)$ has zero average as

$$\int_{-\infty}^{+\infty} \psi(t) dt = 0 \tag{5-4}$$

A cluster wavelet function $\psi_{u,s}(t)$ can be generated through dilation and shift of $\psi(t)$ as form of

$$\psi_{u,s}(t) = \frac{1}{\sqrt{s}} \psi(\frac{t-u}{s}) \tag{5-5}$$

where u is time shift and $s > 0$ is dilation scale factor. The factor $1/\sqrt{S}$ is used to make the energy of $\psi_{u,s}(t)$ normalized.

The wavelet transform of a function $f(t) \in L^2(\mathbb{R})$ at scale s and time shift u is given by

$$\begin{aligned} W_\psi f(u,s) &= \int_{-\infty}^{+\infty} f(t) \cdot \frac{1}{\sqrt{s}} \psi^*(\frac{t-u}{s}) dt \\ &= \int_{-\infty}^{+\infty} f(t) \cdot \psi_{u,s}^*(t) dt = \langle f(t), \psi_{u,s}(t) \rangle \end{aligned} \tag{5-6}$$

where $\psi^*_{u,s}(t)$ is the complex conjugate of $\psi_{u,s}(t)$. $\langle f(t), \psi_{u,s}(t) \rangle$ is the inner product of $f(t)$ and $\psi_{u,s}(t)$, $W_\psi f(u,s)$ is the smooth of $f(t)$ with $\psi_{u,s}(t)$ at different scale and time shift. The frequency response of $\psi_{u,s}(t)$ has multiple frequency resolution in the frequency domain, thus $W_\psi f(u,s)$ reflects different frequency and time resolution. Because u and s is continuous variable, expression (5-6) is called Continuous Wavelet Transform (CWT).

For digital signal processing (DSP) application, CWT needs discretization. Mallat [104] described a dyadic discretization method as $u = 2^j$ and $s = k \cdot 2^j$, the discrete wavelet functions are defined as

$$\psi_{j,k}(t) = 2^{-\frac{j}{2}} \psi(2^{-j}t - k) \tag{5-7}$$

Thus the Dyadic Discrete Wavelet Transform can be defined as

$$d_{j,k} = \int_{-\infty}^{\infty} f(t) \cdot \psi^*_{j,k}(t) dt \tag{5-8}$$

Besides wavelet function, Mallat[104] introduced the scaling function

$$\phi_{j,k} = 2^{-\frac{j}{2}} \cdot \phi(2^{-j}t - k) \tag{5-9}$$

which is orthogonal to discrete wavelet $\psi_{j,k}(t)$, together with

$$a_{j,k} = \int_{-\infty}^{+\infty} f(t) \cdot \phi^*_{j,k}(t) dt \tag{5-10}$$

where $a_{j,k}$ is called the scaling coefficients as the sampled signal $f(t)$.

For a fast numerical computation, Mallat [104] proposed multi-resolution analysis , DWT was transcribed into a filtering process through a pair of quadrature mirror filters defined from the wavelet function $\psi(t)$ and scaling function $\phi(t)$. This is the well-known multi-resolution pyramid algorithm

$$\begin{aligned} a_{j,k} &= \sum_n f[n] \cdot g_j[n - 2^j k] \\ d_{j,k} &= \sum_n f[n] \cdot h_j[n - 2^j k] \end{aligned} \tag{5-11}$$

where $f[n]$ is a discrete time sequence of $f(t)$, $g_j[n - 2^j k]$ is the scaling sequence equivalent to $\phi_{j,k}(t)$ and $h_j[n - 2^j k]$ is called the discrete wavelets equivalent to

$\psi_{j,k}(t)$. $a_{j,k}$ and $d_{j,k}$ present the approximation and details of signal $f(t)$ at the $\mathrm{j}\mathrm{th}$ resolution (scale or level). At the resolution $j+1$, the scaling coefficients and the wavelet coefficients are

$$\begin{aligned} a_{j+1,k} &= \sum_n g_{j+1}[n-2^j k]\cdot a_{j,k} \\ d_{j+1,k} &= \sum_n h_{j+1}[n-2^j k]\cdot a_{j,k} \end{aligned} \tag{5-12}$$

where $g_{j+1}[n]$ and $h_{j+1}[n]$ are

$$\begin{aligned} g_{j+1}[n] &= \sum_k g_j[k]\cdot h_j[n-2k] \\ h_{j+1}[n] &= \sum_k h_j[k]\cdot g_j[n-2k] \end{aligned} \tag{5-13}$$

which present the dyadic down-sample operation. $g_j[n]$ and $h_j[n]$ corresponds to a pair of orthogonal low-pass filter and high-pass filter, the DWT can be implemented by low-high pass filter banks decomposition recursively. Because of dyadic down sampling with increment of level j, the band width of the filter will shrink, representing multi-resolution. The complete process is demonstrated in Figure 5.6.

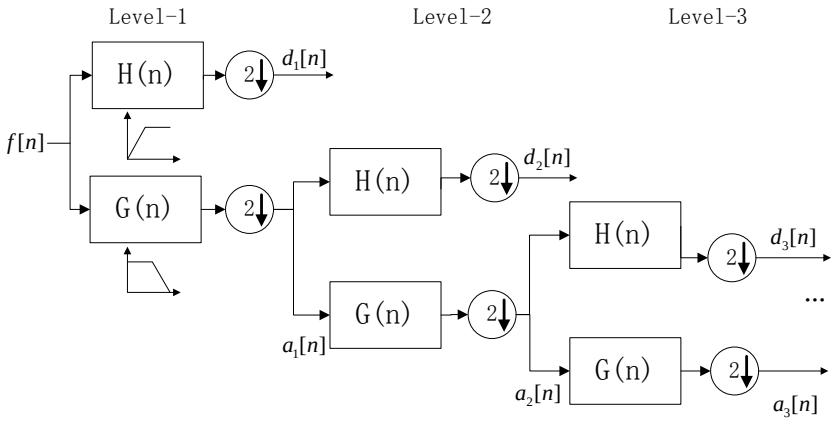

Figure 5.6. Mallat pyramid decomposition algorithm

$H(n)=[h_0,\cdots,h_n]$ are the high-pass filter coefficients, $G(n)=[g_0,\cdots,g_m]$ are low-pass filter coefficients.

$d_j[n]$ are wavelet coefficients at $j\mathrm{th}$ scale which present detail of signal $f[n]$, corresponding to the high-frequency component.

$a_j[n]$ are scaling coefficients at $j\mathrm{th}$ scale which present approximation of signal $f[n]$,corresponding to the low-frequency component.

$\textcircled{2}\downarrow$ is the dyadic down-sampling.

The relationship of signal and decomposed components at different levels is shown in Figure 5.7.

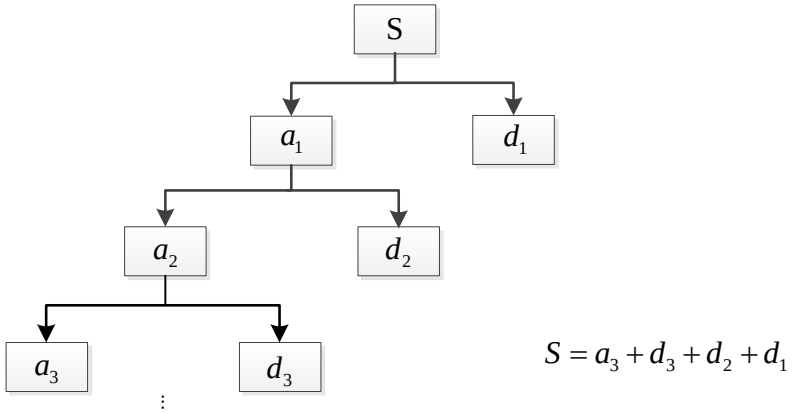

Figure 5.7. Signal and signal decomposition. S is the original signal. a_j and d_j are approximation and detail of the signal at the jth level.

5.4.1.2 Real-time Wavelet Transform

Figure 5.6 shows how to implement DWT by filter banks. In practical application, detecting the singularity or sudden change of the signal needs to calculate DWT through current sample x_i and previous samples $[x_{i-1}, x_{i-2}, \cdots]$. In fact, the $H(n)$ and $G(n)$ con be considered as Finite Impulse Response(FIR) filter, the real-time computation can be structured as in Figure 5.8[105]:

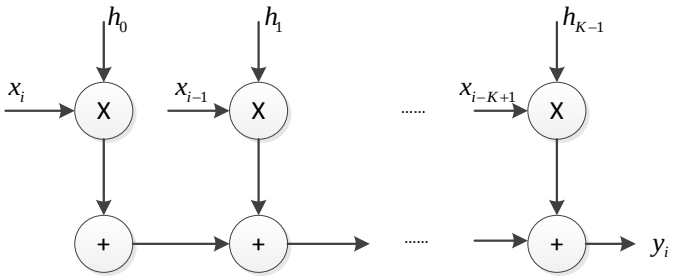

Figure 5.8. Block diagram of real-time K-tap FIR filter. Previous N input samples and output sample are in stored.

$h_0, \cdots, h_{K-1}$ are K-tap FIR filter coefficients, x_i is the current sample with previous samples $x_{i-K+1}, x_{i-N+2}, \cdots, x_{i-1}$. $H(n)$ and $G(n)$ FIR filter are repeatedly used to implement the high and low pass for wavelet decomposition as in Figure 5.6.

However, this lattice FIR filter module will cause $K \cdot \Delta T$ time delay, where ΔT is the sample period[105]. Table 5–1 shows the computational time delays ($K \cdot \Delta T$) at

different scales with various wavelet functions. More details of wavelet families and filter banks can be found in MATLAB Wavelet Toolbox[106].

Table 5–1.Time delays of wavelet coefficients at different scales

Scale (2^i)	Haar (K_i)	Db4 (K_i)	Db8 (K_i)	Coif1 (K_i)
2^1	2	8	16	6
2^2	4	22	46	16
2^3	8	50	106	36
2^4	16	106	226	76
2^5	32	218	466	156

As shown in Figure 5.9, at larger scale decomposition, the time delay will increase with respect to the K increment of $H(n)$ and $G(n)$.

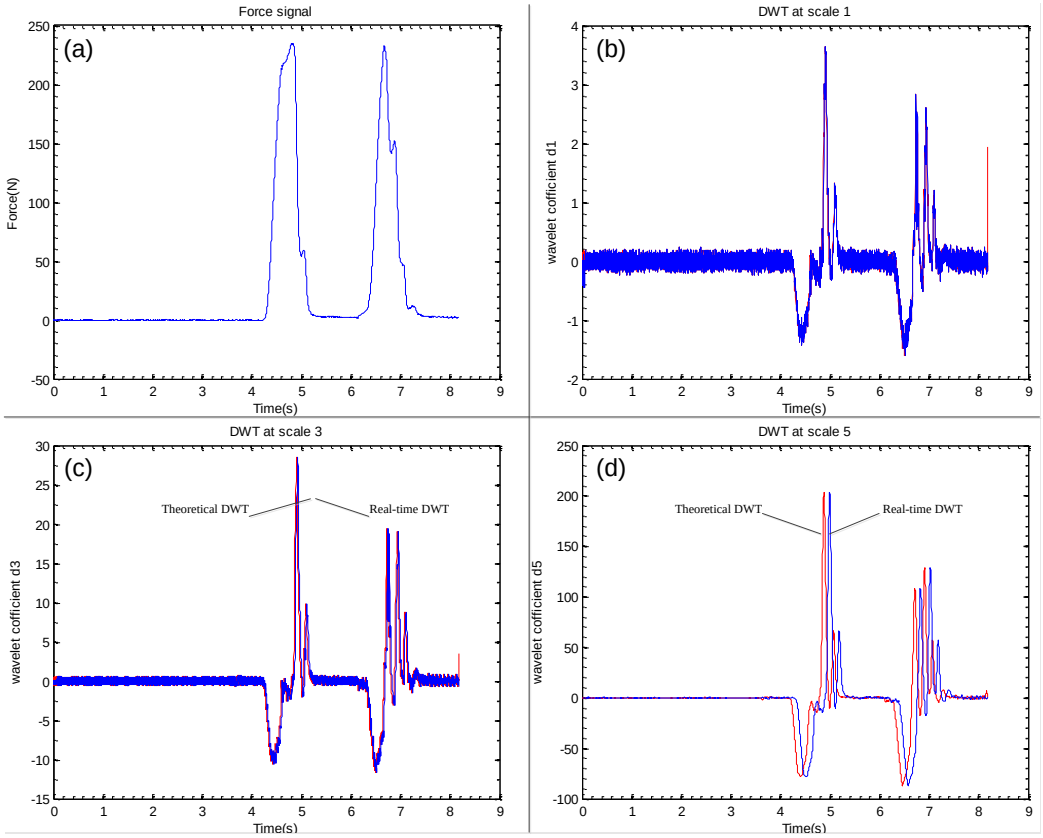

Figure 5.9. Time delays of wavelet coefficients at different scales. (a) Original drilling force through two layers of porcine femur at v_f =12.5mm/s and w =600 rpm (b) Wavelet coefficients at scale = 2^1, (c) Wavelet coefficients at scale= 2^3, (d) Wavelet coefficients at scale= 2^5. Blue solid line is the real-time computation value. Red dash line is the theoretical value. 'Haar' wavelet was chosen.

In practical computation, K is always chosen in form of 2^j, e.g. in our application, $K = 64$.

5.4.1.3 Modulus Maxima of Wavelet coefficients

Mallat,et al [107], [108, 109] proposed the wavelet transform as an efficient tool for detecting and characterizing signal singularity. The singular signal can be simply considered as addition of a stationary signal and step signal $s(t)$, which presents the signal edge, or addition of a stationary signal and pulse signal $\delta(t)$, which presents the sudden change of signal. The singularity of signal is characterized by wavelet vanishing moments, and converge wavelet modulus maxima across scales. Wavelet transform with n vanishing moments can be interpreted as a differential operator of $n\text{th}$ order of the smoothed signal. For the dyadic DWT, at each scale $s = 2^j$, the modulus maxima are defined as a set of wavelet coefficients which are locally maximum at $u = u_0$ as

$$\frac{\partial W_\psi f(u_0, 2^j)}{\partial u} = 0 \tag{5-14}$$

For numerical computation, equation (5-14) can be expressed as

$$\{W_\psi f(u_0, 2^j) \mid \left|W_\psi f(u, 2^j)\right| \le \left|W_\psi f(u_0, 2^j)\right|, u \in [u_0 - \varepsilon, u_0 + \varepsilon]\} \tag{5-15}$$

where u belongs to the left and right neighborhood of u_0. If the wavelet function $\psi_{u,2^j}(t)$ has one vanishing moment, the modulus maxima correspond to signal discontinuities. If $\psi_{u,2^j}(t)$ has two vanishing moments, the modulus maxima correspond to discontinuities on the derivative of signal smoothed. When the wavelet transform has no modulus maxima at fine scales, the signal is locally regular. Mallat,et al [107] pointed out that singularity could be detected by finding abscissa where the wavelet modulus maxima converged at fine scales, in other words, the modulus maxima preserved the characteristic of singularity along different scales by which some "pseudo singularity" caused by interference or noise could be identified and removed. Hence, the localization of wavelet transform modulus maxima at different scale can be used to detect the signal singularity. Figure 5.10 and Figure 5.11 show different types of singularities such as step and pulse signal, with different wavelet functions, the modulus maxima performed different shapes.

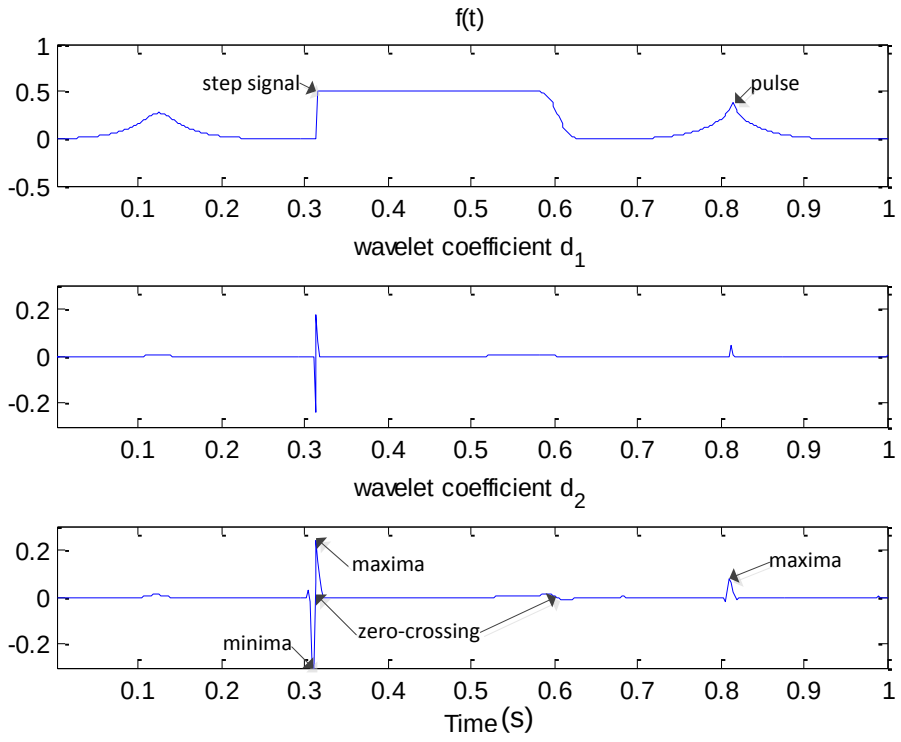

Figure 5.10. Different types of singularities and modulus maxima with 'db2' wavelet at scales 2^1 and 2^2. Minima, maxima and zero-crossing indicate the 'step type' signal.

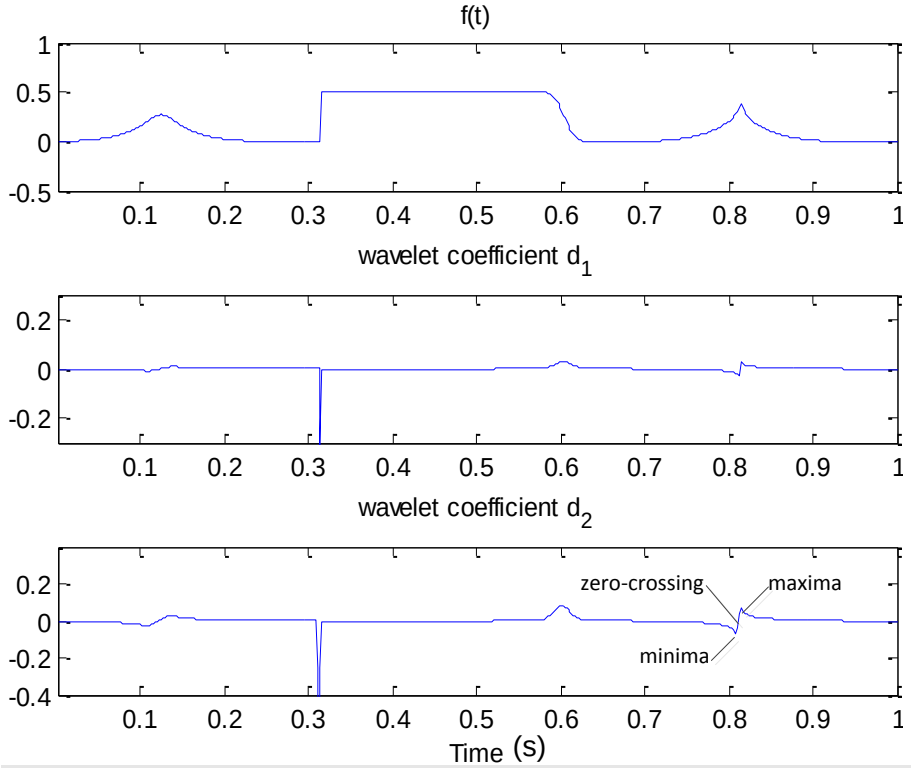

Figure 5.11. Different types of singularities and modulus maxima with 'haar' wavelet at scales 2^1 and 2^2. Minima, maxima and zero-crossing indicate the pulse type signal.

To improve the accuracy and anti-interference, maxima, minima and zero-crossing were suggested for singularity detection with specific wavelet function[108].

5.4.1.4 Break-through Detection Algorithm

Step 1: *Compute wavelet coefficients* $d_j(n)$

a) *Apply real-time DWT to force signal* $Fz(n)$ *for sequence of wavelet coefficients* $d_j(n)$ *at* 2^j *scale.* $j = 1,2,3,4,5$, $n = 1,\cdots,N$

b) *Shift* $d_j(n)$ *with filter length* K_j *at* 2^j *scale for alignment.*

Step 2: *Find modulus maxima at different scales*

Step (1): *Find minima* NM_k^j *and maxima* PM_k^j *at* 2^j *scale.* k *is the position recorded in sequence of* $d_j(n)$.

Step (2): *Repeat Step (1) from* j *= 5 to 2, in other words, from large to fine scale. If the position* k *preserve the modulus maxima at different scales,* NM_k^j *and* PM_k^j *should be kept with respect to* k .

Step (3): *Compute the threshold from stage 1 of drilling penetration.*

a) *If the* $F_z(n) < \frac{1}{3} \cdot \text{maximum of recorded } F_z(n)$ *, this can be considered as break-through of front cortical wall by drill bit.*

b) *Find maximum of* $\left|NM_k^j\right|$ *and* $\left|PM_k^j\right|$ *as* NTh_j *and* PTh_j *at* 2^j *scale.*

Step (4): *Prediction of the break-through of front cortical wall.*

a) *Repeat Step (1) to Step (3) until* $NM_k^j > \frac{1}{2} \cdot NTh_j$ *with successive* $PM_k^j > \frac{1}{2} \cdot PTh_j$ *occurs from scale* $j = 5 \text{ to } 2$ *, this moment can be considered as break-through of back cortical wall by drill bit.*

b) *Send 'STOP' command to robot.*

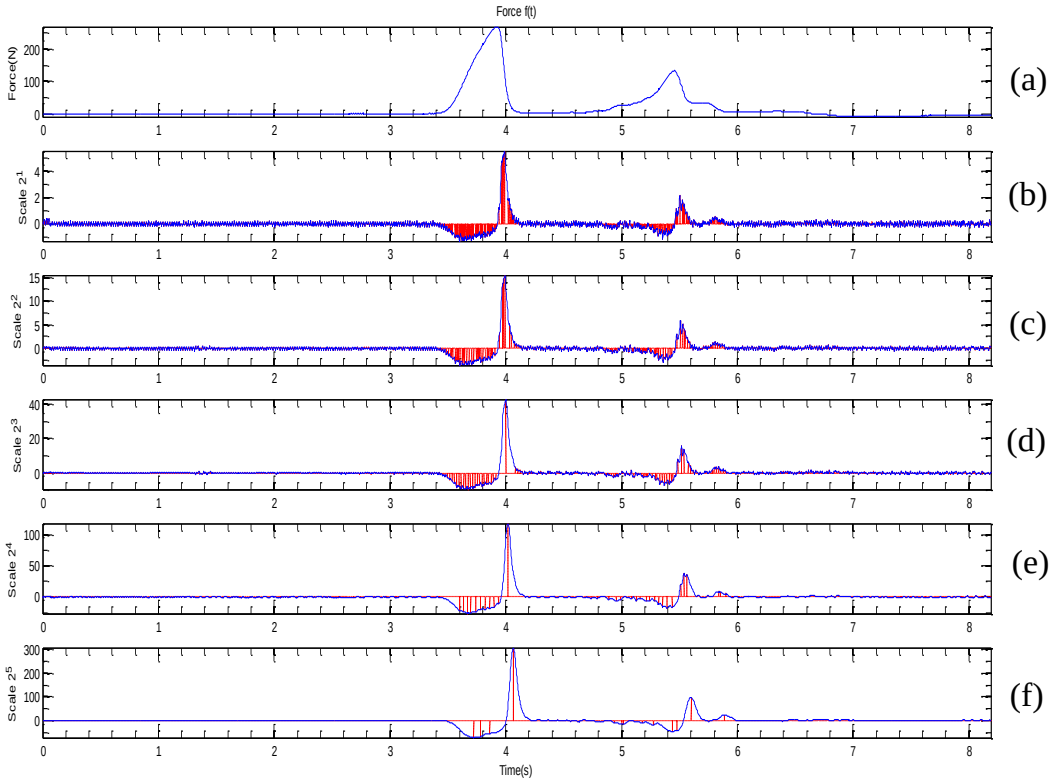

Figure 5.12. (a) $f(t)$ **is force signal. (b) to (f) Blue solid lines are wavelet coefficients at different scales, red dash lines are the modulus maxima at different scales.**

In the above steps, the search for modulus maxima is from larger scale to finer scale. This search method can reduce the effect of high-frequency disturbance which is always presented more in the lower scales, and red dash lines in Figure.5.12.(b) to (f) indicate of smaller number of modulus maxima (NM_k^j and PM_k^j) in larger scales with smaller number of search.

5.4.1.5 Result and Discussion

The results of detection algorithm are shown in Figure 5.13 (a). On the stage 1 of drilling penetration, the found positive and negative thresholds provide the reference for detection on stage 3. Figure 5.13 (b) shows two break-through stops compared with three complete penetrated holes on porcine femur segment.

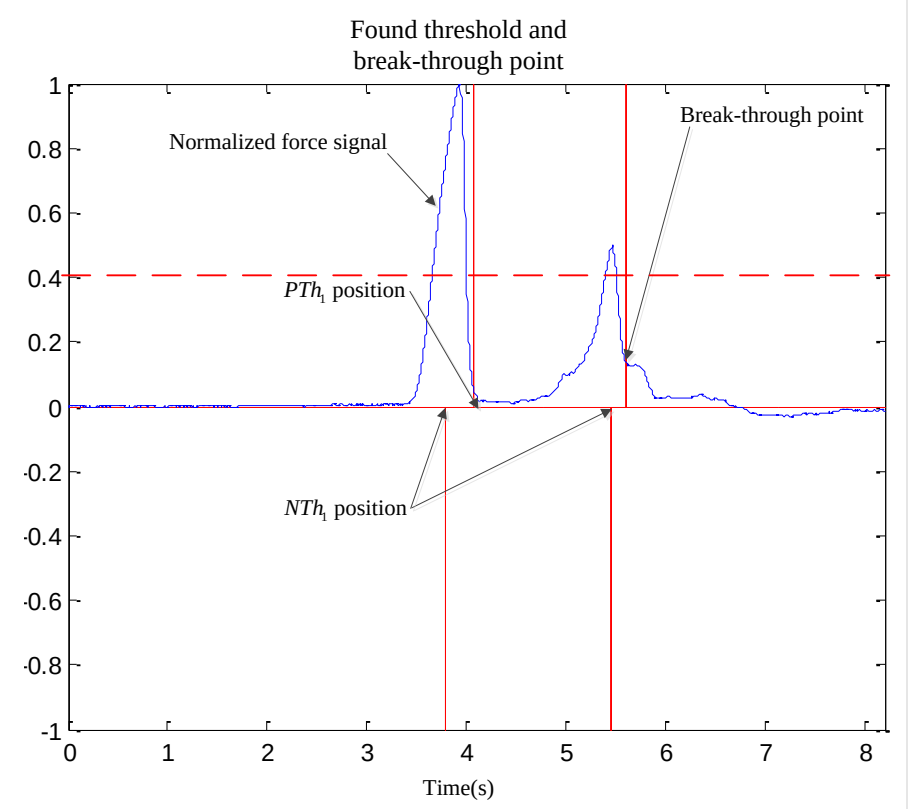

(a)

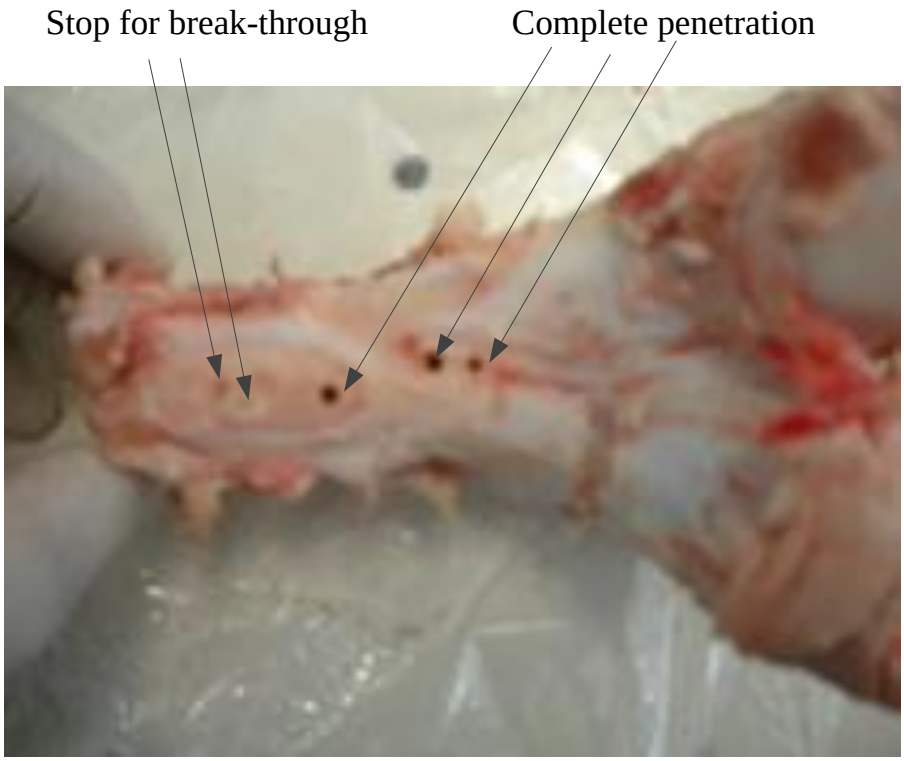

(b)

Figure 5.13. (a). Normalized force signal with found threshold position. The final PTh indicates the break-through point of back cortical wall. (b). Comparison of break-through stop and complete penetration on porcine femur.

However, because the composition and geometry of bone are complex and various, the force signal of drilling sometimes is mixed with high unknown disturbance, by which the maxima modulus search will fail for break-through detection.

5.5 3D Finite Element Analysis of Drilling Bone in Relation to Orthopedic Surgery

5.5.1 Motivation

In orthopedic surgery, bone machining operations such as drilling, milling and sawing are similar to the industrial manufacturing application. However, because of requirements by safety, low damage, minimal invasion and saving surgery time, various novel design and functionality of surgical tool have been introduced in the orthopedic surgery, neuro-surgery, and dental implant surgery. Engineer and doctor have kept investigation on instrument design, static or dynamic operation intro-/post- operative processes.

The finite element analysis (FEA) has been widely used for medical instrument design, evaluation of tissue biomechanics and various surgery processes, as possible substitute for high-cost and complex experimental work, especially as useful tool for validation of experimental or analytical results.

In maxillofacial surgery, three-dimensional finite element analysis is used to evaluate post-operative stress distribution in the fixation plates and screws in the surrounding bone and the complex biomechanical behavior. Vertical, horizontal and oblique external load are applied on implant [110-112].

In oral surgery, FEA has been extensively used as a tool of functional assessments for values or gradient distribution of stress and strain in the field of oral osseointegration [113].

In orthopedic surgery, Battula [114] utilize 3D finite element model to examine the effect of axial push-out and pull-out of self-tapping cortical bone screws inserted to different depths in normal and osteoporosis bone materials.

Keyak,et al [115], [116] apply and compare linear and nonlinear finite element models to identify proximal femoral fracture load. For the linear and non-linear model, finite element model of femur is considered as elastic and elastic-plastic material. Static load is applied to the model with fracture criterion derived from the *in vitro* experiment.

However, the above research focused on tiny deformation of bone with static external load. Elastic property is usually adopted for bone material. The biomechanics of bone performed elastic under small strain and plastic under large strain. When the

stress applied on bone beyond ultimate stress, fracture will generate. For machining bone operation, such as high speed and high load cutting or milling, the surgical region of bone performs large deformation, local fracture and heat increase with chip separation.

Tu,et al [117] use elastic FE model to simulate the process of temperature change for kirschner pin drilling through the bone. The phantom experiment which adopted bone-like substitute provided by Sawbones was tested for the simulation.

Paszenda,et al [118] give 3D FE model in ANSYS workbench to simulate the stress distribution on the drill bit during femur drilling process. The objective of simulation was to evaluate the effect of different drill bit geometries for optimizing the medical instrument design. Because the FE model is based on elastic model, the simulation process is far from the real process.

Alam,et al [119] apply plastic property of bone on FEM for plane cutting simulation. Since the proposed FE model is based on two-dimension, the drilling process has to be approximated to the orthogonal plane cutting. Chip generation, temperature and stress distribution of simulation are given and verified with the cutting experiment on frozen and dry bovine bone.

In our research, we proposed a versatile 3D finite element rigid-plastic and elasto-plastic model to predict the biomechanical performance and the stress states for drilling bone process. Mechanical analysis is conducted by applying parameters corresponding to specific porcine bone and drill bit. For the plastic model, material constitutive equation is based on stress-strain-strain rate curve. FEA shows complete drilling penetration of bone and display visualized drilling force and stress distribution during the robotic assisted orthopedic surgery. Experiment of drilling porcine femur was implemented for confirmation of the FEA results.

5.5.2 Methods and Material

5.5.2.1 Basic Principle of Mechanics and Finite Element Method

Under tiny deformation, elastic solid material is one that returns to its original unloaded shape upon the removal of applied forces. A homogeneous material is one that possesses the same material properties at all points. An isotropic material has the same material properties in all directions.

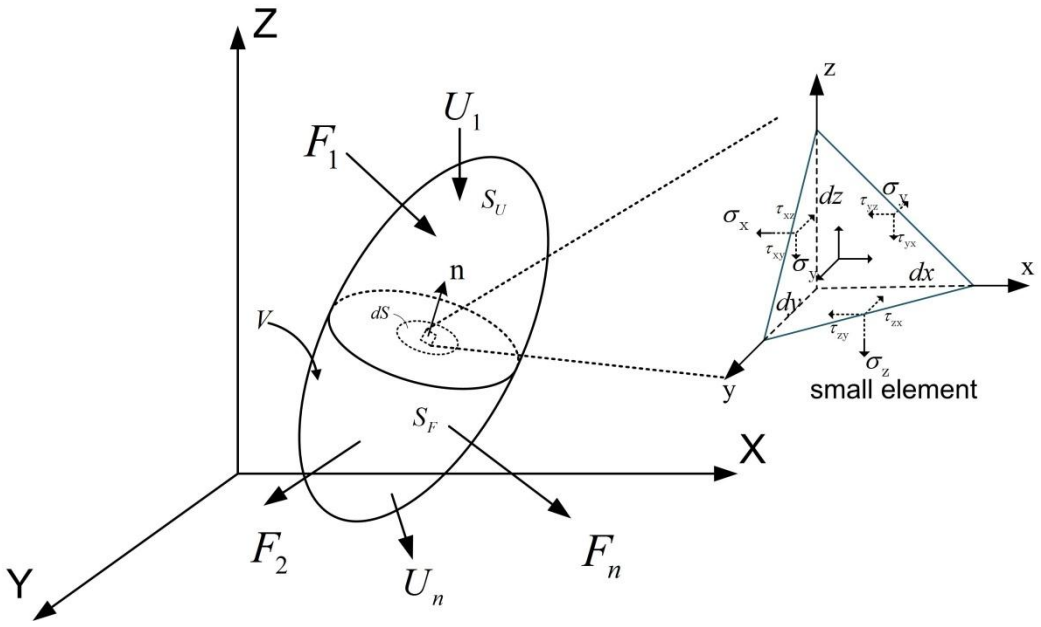

Figure 5.14. Normal stress and shear stress on tetrahedral element of solid object. $F_1,\cdots,F_n$ **are external forces on surface** S_F **,** $U_1,\cdots,U_n$ **are deformation velocity on surface** S_U **.** dS **and** S **are the internal surfaces.** n **is the normal vector on surface of** S **.** V **is the volume of solid object.**

As shown in Figure 5.14, σ_x , σ_y and σ_z represent the stresses acting on a plane normal to axis X, Y and Z. τ_{xy} , τ_{xz} , τ_{yx} , τ_{yz} , τ_{zx} and τ_{zy} represent shear stresses acting on a plane normal to axes X, Y and Z. According to Hooke's law, the stress and strain function can be written as

$$\begin{Bmatrix} \sigma_x \\ \sigma_y \\ \sigma_z \\ \tau_{xy} \\ \tau_{xz} \\ \tau_{yz} \end{Bmatrix} = \frac{E}{(1+\nu)(1-2\nu)} \begin{bmatrix} 1-\nu & \nu & \nu & 0 & 0 & 0 \\ \nu & 1-\nu & \nu & 0 & 0 & 0 \\ \nu & \nu & 1-\nu & 0 & 0 & 0 \\ 0 & 0 & 0 & \dfrac{1-2\nu}{\nu} & 0 & 0 \\ 0 & 0 & 0 & 0 & \dfrac{1-2\nu}{2} & 0 \\ 0 & 0 & 0 & 0 & 0 & \dfrac{1-2\nu}{2} \end{bmatrix} \begin{Bmatrix} \varepsilon_x \\ \varepsilon_y \\ \varepsilon_z \\ \gamma_{xy} \\ \gamma_{xz} \\ \gamma_{yz} \end{Bmatrix} \quad (5\text{-}16)$$

where ε_x , ε_y , ε_z and γ_{xy} , γ_{xz} , γ_{yz} are linear and shear strains, E is Young's modulus and ν is Poisson's ratio.

Equation (5-16) can be written as matrix form

$$\{\sigma\} = [C] \cdot \{\varepsilon\} \quad (5\text{-}17)$$

where $[C]$ refers to elastic stiffness matrix.

Considering the strain change due to the thermal effect, equation (5-17) can be written in differential form as

$$\{d\sigma\} = [C] \cdot \{d\varepsilon\} - [C^{th}] \cdot \{\alpha\} \cdot dT \tag{5-18}$$

where $\{d\sigma\}$ is the stress increment matrix, $[C^{th}]$ is the thermal stiffness matrix, $\{\alpha\}$ is the thermal expansion coefficient matrix, dT is the temperature increment.

Under large deformation, plastic material is one that generates permanent deformation upon the removal of applied forces. Stress under plastic deformation is highly non-linear function of strain and temperature. For elasto-plastic material, stress equation can be expanded to

$$\{d\sigma\} = ([C^e] + [C^p]) \cdot \{d\varepsilon\} - [C^{th}]\{\alpha\} \cdot dT \tag{5-19}$$

where, $[C^e]$ is the elastic stiffness matrix, $[C^p]$ is the plastic stiffness matrix, $\{d\sigma\}$ is the stress increment, $\{d\varepsilon\}$ is the total strain increment, $\{d\varepsilon^{th}\} = \{\alpha\} \cdot dT$ is thermal strain increment due to temperature increment dT for elastic deformation.

For finite element based simulation, flow formulation can be derived using following weak variational form of equilibrium equation (potential energy principle) expressed in terms of arbitrary variation in velocity field [120]

$$\int_V \bar{\sigma} \cdot \delta\dot{\varepsilon}_{ij} dV + K \int_V \dot{\varepsilon}_V \cdot \delta\dot{\varepsilon}_V dV - \int_{S_F} F_i \cdot \delta v_i dS = 0 \tag{5-20}$$

with boundary conditions:

$$v_i = U_i \text{ on } S_U$$

$$\sigma_{ij} n_j = F_i \text{ on } S_F$$

where $\dot{\varepsilon}_V = \dot{\varepsilon}_{ii} (i = x, y, z)$ is the volumetric strain-rate, v_i is the deformation velocity of element. F_i is the force on boundary surface of S_F and U_i is the deformation velocity on boundary surface of S_U. V and S are volume and surface of the object. The penalty constant K should be a large positive constant for incompressibility[120, 121].

Based on the flow formulation approach, finite element code always adopts iterative Lagrangian process. The finite element solving engine uses a direct iteration method and Newton–Raphson method to solve the non-linear equations. During solution process, the direct iteration method generates the initial estimate for the Newton–Raphson method, which is then used to obtain a rapid final convergence. The conver-

gence criteria for iteration process are based on the velocity norm error ratio $\|\Delta v\|/\|v\|$ and force norm error ratio $\|\Delta F\|/\|F\|$. $\|v\|$ is L^2 norm $(v^T v)^{1/2}$ [122].

As shown in Figure 5.15, to solve a problem using finite element method, the following basic steps are made:

1) Identify problem, sketch the structure and constitutive equation.
2) Create the object geometry by CAD/CAM system.
3) Mesh the model.
4) Apply boundary conditions (constraints, movement, load and initialization) on the model.
5) Solve numerical equations iteratively (remeshing and interpolation).
6) Analyze the results (for understanding, evaluation, and making a decision).

Steps 1), 2), 3) and 4) are known as a preprocessor, 5) is a processor and 6) is a postprocessor (Figure 5.15).

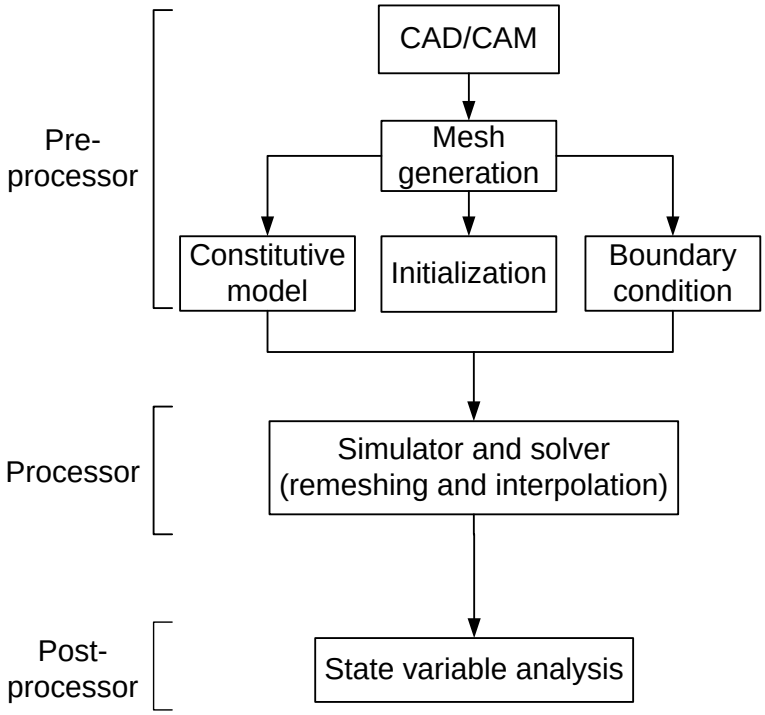

Figure 5.15. Solving process of finite element method

5.5.2.2 Mechanical Property of Bone

The main function of bones is to support and protect other types of tissue found in bones include marrow, nerves, blood vessels, endosteum, periosteum and cartilage[94].

Stress-strain curve is used to describe the whole mechanical property of compact bone (Figure 5.16). Stress is considered as the intensity of the load per unit area that applied on a plane surface. Strain is the deformation that responses to externally applied loads. In elastic region, external load does not cause permanent deformation, but once the yield point (*point A* in Figure 5.16) is exceeded, some deformation is permanent. For describing the elastic property, Young's modulus

$$E = \frac{\Delta\sigma}{\Delta\varepsilon} \tag{5-21}$$

is defined as slope of the stress-strain curve before *yield point A.* E represents stiffness of the material [94].

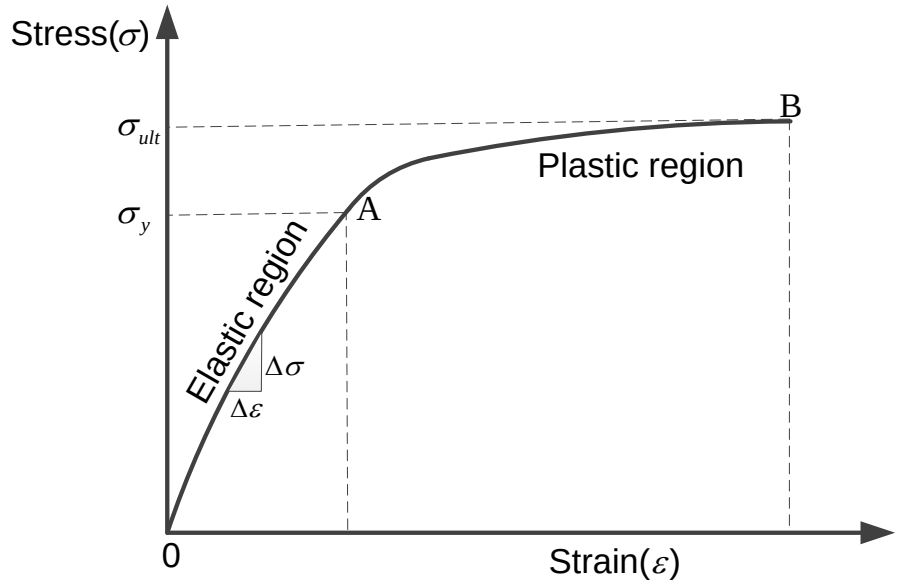

Figure 5.16. Strain-strain curve for a cortical bone sample in tension

After yield point is reached, bone exhibits extensive unrecovered deformation before failing, as indicated by the plastic region on the stress-strain curve. Stress-strain curve of bone is similar to of metal, but with much less in plastic region When ultimate failure *point B* is reached along the plastic curve, the bone will get broken.

Besides stress and strain, bone's biomechanical behavior varies with the rate at which it is loaded. This is called visco-plasticity which is stiffer and sustains a higher load to failure when loads are applied at higher strain rates ($\dot{\varepsilon} = d\varepsilon/dt$).rates ($\dot{\varepsilon} = d\varepsilon/dt$). Melnis,et al [123] measured the mechanical property of human compact bone and measured the tensile stress with strain deformation from 0~0.025 at five fixed strain rates (10^{-5}, 10^{-3}, 10^{-2}, 10^{-1} and 1 sec^{-1}) as shown in Figure 5.17.

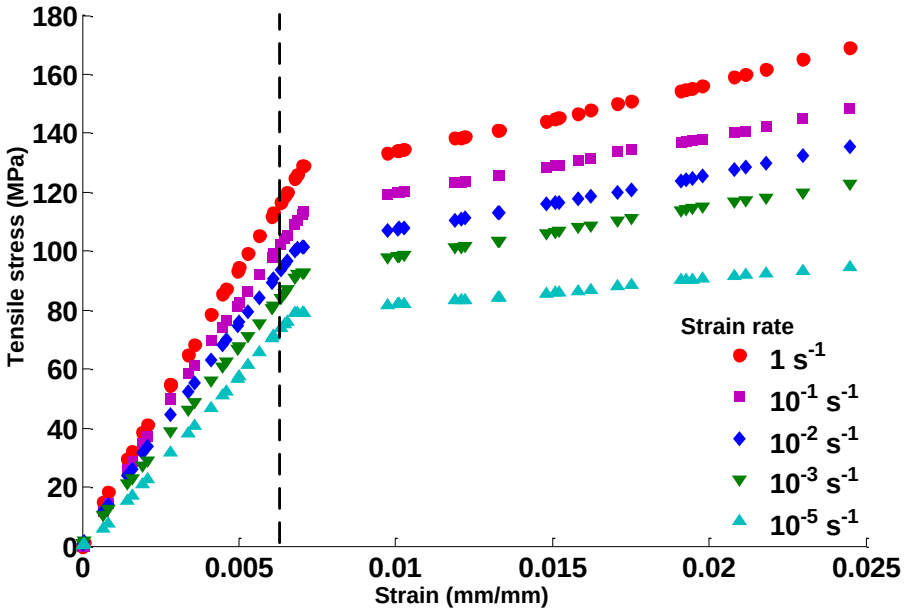

Figure 5.17. Tensile stress(σ)–strain(ε) curves for human femoral cortical bone as a function of strain rate($\dot{\varepsilon}$)(reprinted from [123]).

When strain ε is less than 0.006, cortical bone undergoes linear elastic deformation. When strain ε is larger than 0.006 with yield stress σ_y (80~100 MPa), cortical bone undergoes non-linear plastic deformation. When ε exceeds 0.025 and $\sigma > \sigma_{ult}$ (160~180 MPa), the cortical bone fracture will occurs[94].

In linear elastic region, basic mechanical parameters of drill bit and femur are listed in Table 5–2.

Table 5–2. Elastic and thermal parameters of drill bit and human femur cortical bone.

	Drill bit[124]	Femur cortical bone [123, 125, 126]
Density ($\mathrm{kg \cdot m^{-3}}$)	7840	2100
Young's modulus (GPa)	220	17
Poisson's ratio	0.3	0.35
Yielding strength (MPa)	608	110
Tension strength (MPa)	1000	148
Specific Heat ($\mathrm{J/(kg \cdot ^\circ C)}$)	490	1260
Thermal expansion ($^\circ\mathrm{C}^{-1}$)	6.3×10^{-06}	2.75×10^{-05}
Conductivity($\mathrm{W/(m \cdot ^\circ C)}$)	16	0.38

In non-linear plastic region, the stress-strain curve with strain rate can be expressed as implicit function

$$\sigma = \sigma(\varepsilon_p, \dot{\varepsilon}_p, T) \tag{5-22}$$

Empirical power law curve as

$$\sigma(\varepsilon_p, \dot{\varepsilon}_p, T) = c \cdot \varepsilon_p^n \cdot \dot{\varepsilon}_p^m \cdot (\frac{T}{T_0})^{-r} + y \tag{5-23}$$

is adopted to estimate the stress-strain curve, where ε_p is plastic strain, $\dot{\varepsilon}_p$ is plastic strain rate, T is temperature and T_0 is the reference room temperature. c, n, m, r and y are constant coefficients[122]. However, the thermal effect is omitted for plastic region.

Using the simplex method, fitted parameters are calculated as $c = 408.796$, $m = 0.0629271$, $n = 0.305785$ and $y = 32.7191$ (see Figure 5.18).

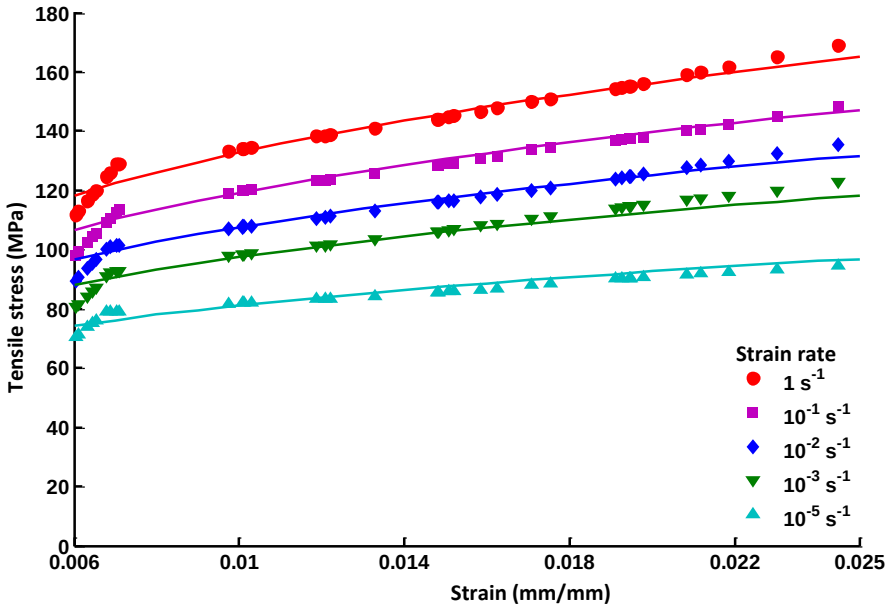

Figure 5.18. Fitted curve and the reported experimental data in plastic region. Solid lines are fitted curve, dot lines are experimental data from[123].

The FEM and FEA are implemented through DEFORM-3D™ software which is a powerful finite element simulation system. DEFORM-3D™ is designed to analyze three-dimensional deformation and heat treatment process used by metal forming and related manufacturing processes, such as forging, cutting and cogging. The FE software provides conjugate-gradient or sparse solvers with direct or Newton-Raphson iteration method. The drilling bone process can be approximate to similar deformation process of metal. DEFORM-3D™ provides four basic type materials:

rigid, elastic, plastic, and elasto-plastic materials with stress-strain curves shown in Figure 5.19:

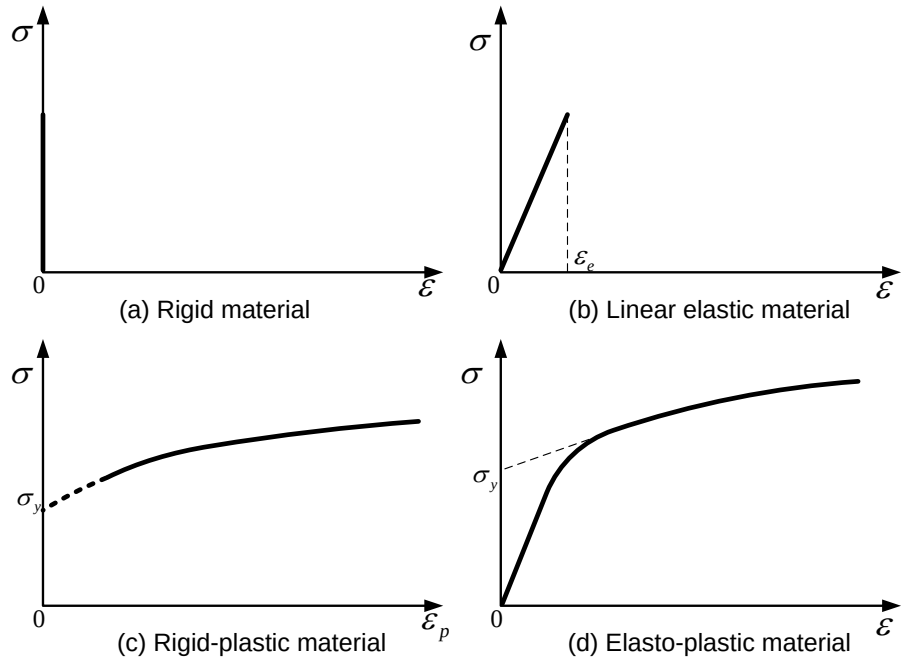

Figure 5.19. Stress-strain curves of rigid, elastic, plastic and elasto-plastic material in DEFORM-3D™.

In finite element simulation, the drill bit is set as rigid object which has no deformation under external load.

Rigid-plastic objects are modeled depending on the plastic material characteristic which assumes that stress (σ) increases with strain rate ($\dot{\varepsilon}$) until a threshold strain rate beyond which the objects deform plastically. For rigid-plastic object, the plastic stress-strain curve is needed. The rigid-plastic model provides good simulation of real material behavior and response of the strain rate sensitivity.

Elasto-plastic objects are treated as elastic objects until the yield point is reached. Any portions of the object that reach the yield point are treated as plastic, while the remainder of the object is treated as elastic. The total strain (ε_{total}) in the object is a combination of elastic strain (ε_e) and plastic strain (ε_p) as

$$\varepsilon_{total} = \varepsilon_e + \varepsilon_p \tag{5-24}$$

Elasto-plastic model provides a realistic simulation of elastic recovery and strains due to thermal expansion. However, the simulation of elasto-plastic object always takes extremely long solution time and is difficult for convergence.

For elasto-plastic object in DEFORM-3D™, in addition to the stress-strain data, the material is also required to have Young's modulus (E), Poisson's ratio (υ) and Thermal expansion coefficient (α) which are parameters for elastic deformation. The bone model is set as plastic and elasto-plastic object for comparison.

5.5.2.3 Geometry Modeling, Mesh Generation and Boundary Condition

The twist drill bit is commonly used for orthopedic surgery (Figure 5.20 (b)). The hollow drill bit (Figure 5.20 (a)) is particularly used to remove a bone block or to take bone core samples in post-surgical process [127] or *in vitro* experiment [128]. In the experiment and FEM, the diameter and lips angle of twist drill bit are 3.2 mm and 120 . The hollow drill bit consists of three cutting blades with flutes and inner cored grinder with diameter of 3.2 mm.

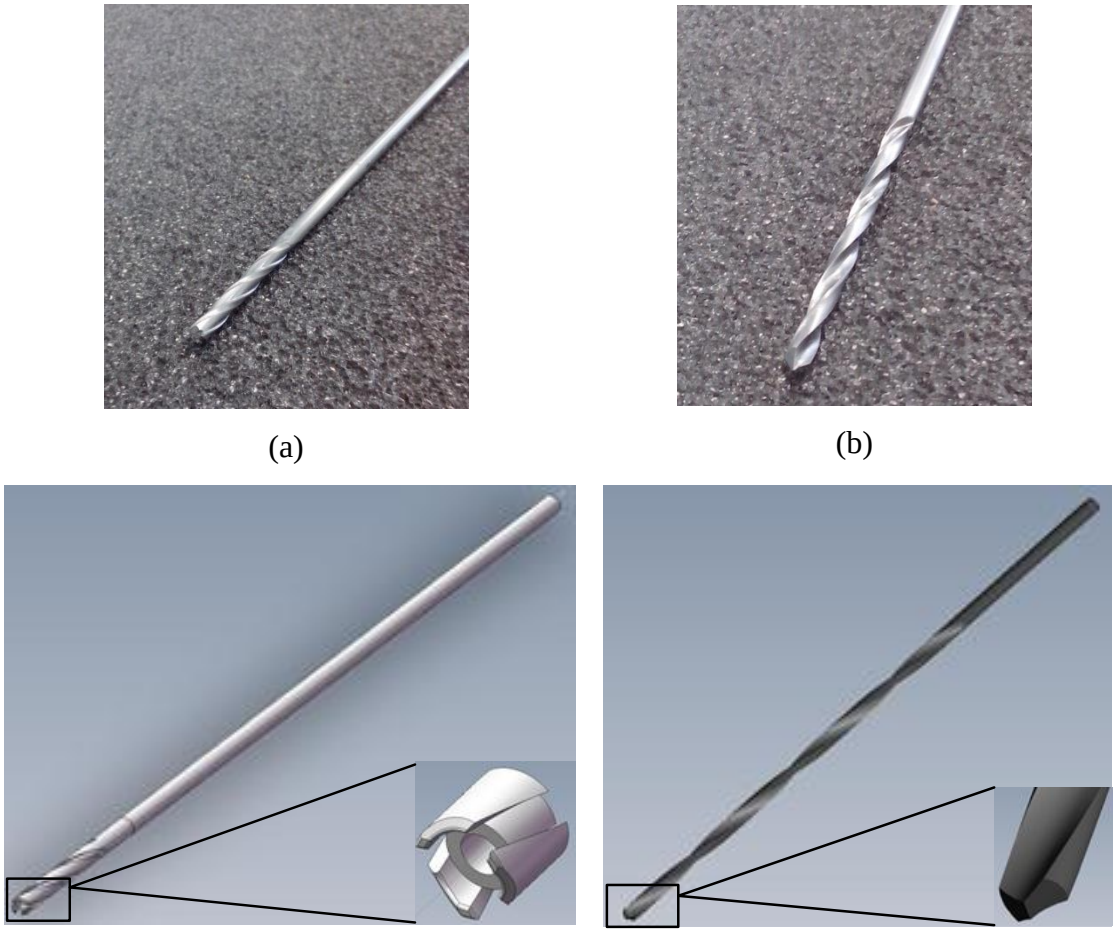

Figure 5.20. (a) and (b) are hollow bit and twist bit. (c) and (d) are CAD models in SolidWorks®.

The process of drilling bone by a twist bit can be approximated to orthogonal cutting operation (see Figure.21). The feed rate and rotation speed are decomposed into to cutting speed V_c.

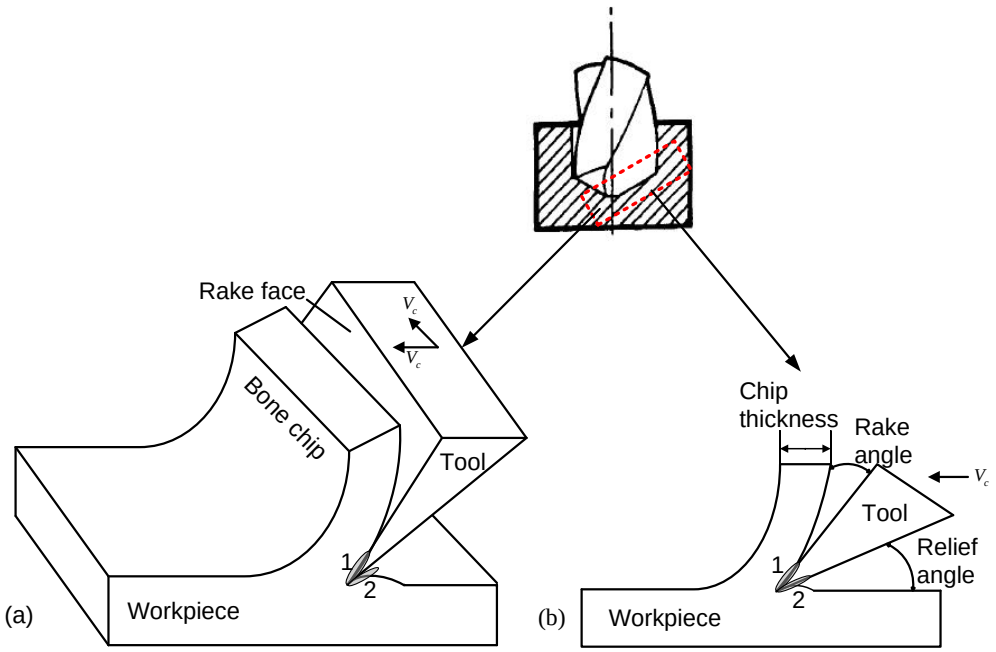

Figure.21. Mechanism of orthogonal cutting. (a) is isotropic view and (b) is side view. Region 1 and 2 are the primary and second shear zone[129].

Different from the twist bit, the process of drilling bone by hollow bit consists of cutting, milling and punching operation. It is difficult to setup analytical analysis of the complex tool, but FEM is a sufficient tool instead. The effects of these two type drill bits are evaluated in FEM and *in vitro* experiment.

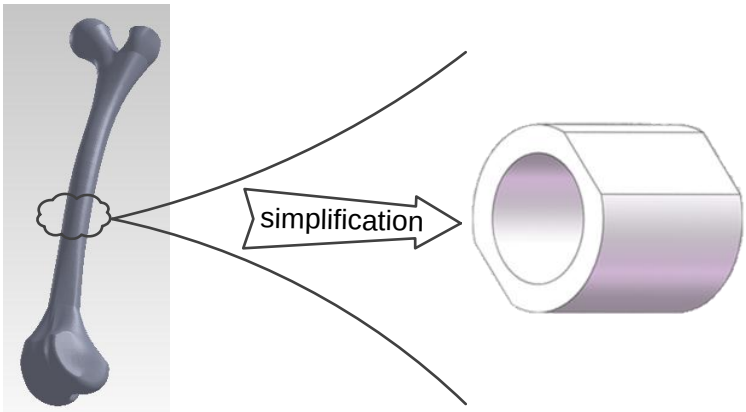

Figure 5.22. Geometry model of porcine femur for plastic object as hollow cylinder.

A segment of porcine femur is modeled as hollow cylinder (see Figure 5.23). Since the thickness of the fresh porcine femur samples varied from 1 mm to 5 mm,

the thickness of the drilling area on 3D model is set as 2 mm for trade-off between accuracy and feasibility. Material of the model is assumed as homogenous and isotropic.

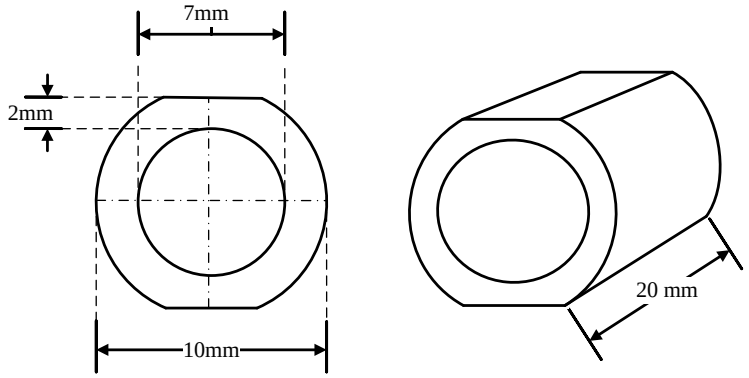

Figure 5.23. Simplified femur bone as hollow cylinder with side view and isotropic view: length = 20mm, inner diameter = 7 mm, outer diameter = 10 mm, thickness = 2 mm.

To shorten the simulation time for solving the elasto-plastic model, the bone is modeled as thin piece of disc with 2 mm height and 8 mm diameter (see Figure 5.24).

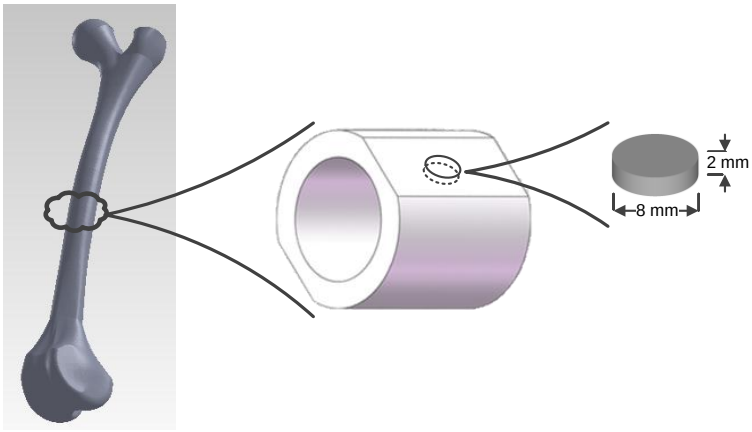

Figure 5.24. Geometry model of femur bone for elasto-plastic object as thin cylinder.

Tetra elements with four nodes are used for meshing the drill bit and piece. DEFORM-3D™ provides dual mesh density technology for improving accuracy and saving computation time. The finer the mesh grid is defined, the more number of elements are generated. Finer mesh density is applied on the drilling regions in order to predict where steep stress or temperature gradient arises, and coarser mesh density is chosen for the regions with low stress gradient, the regions away from the drilling region. The length of element edge is set to 0.08mm for finer mesh grid, and 0.8mm for coarser mesh grid.

The feed rate and rotation velocity of drill bit are set as 12.5 mm/s and 600 rpm respectively. The bone model is fixed during the simulation of drilling process,

thus on the configuration of boundary condition, the distal edge of the object is fixed along the X, Y and Z axes (see Figure 5.25 and Figure 5.26).

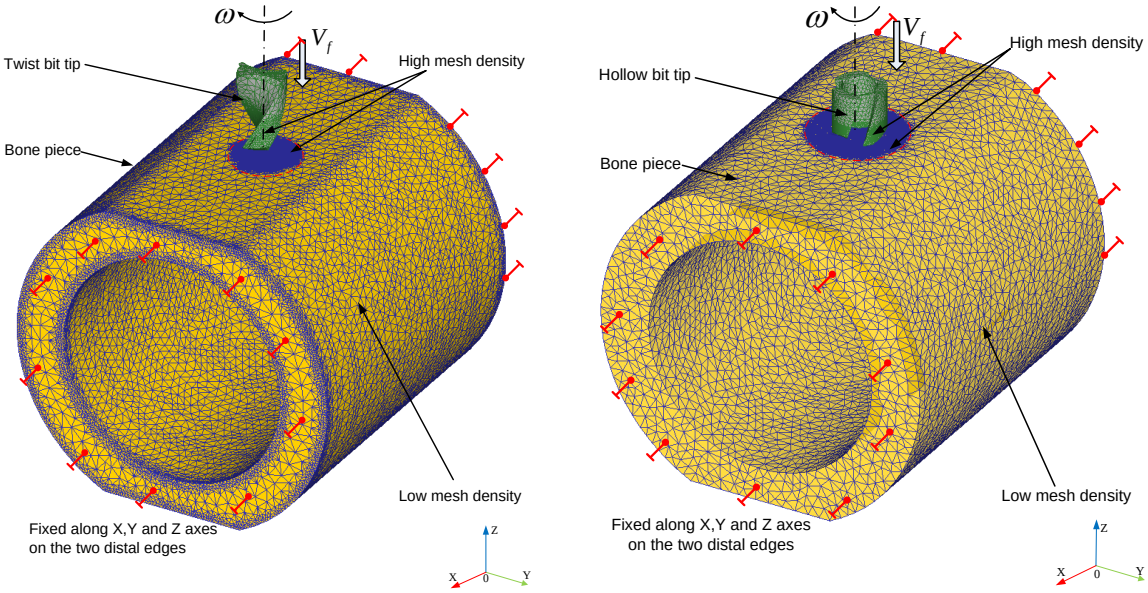

(a) (b)

Figure 5.25. Bone is modeled as hollow cylinder with plastic material. (a) and (b) show the movement of twist- and hollow-bit tip and boundary configuration on distal end of bone model.

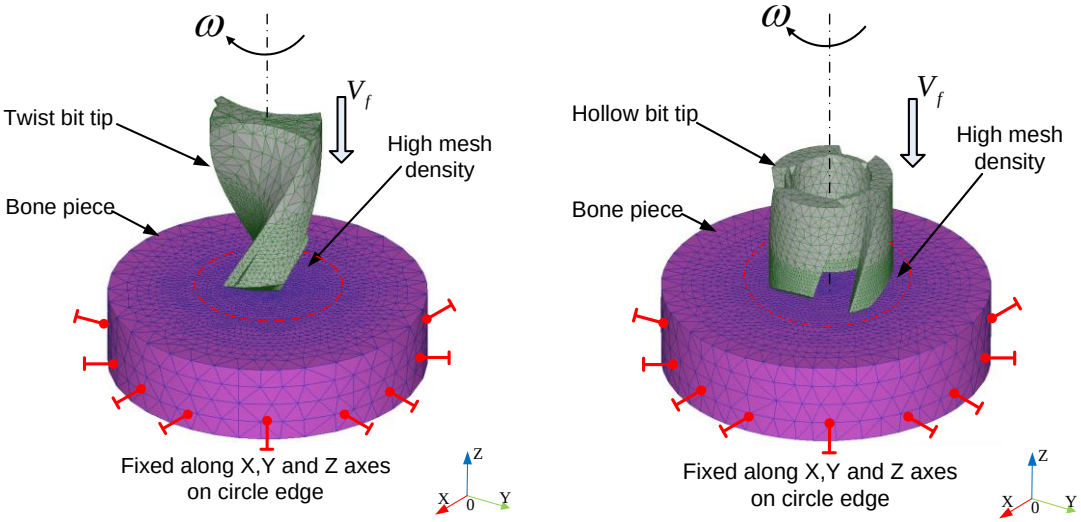

(a) (b)

Figure 5.26. Bone is modeled as piece of cylinder with plastic material. (a) and (b) show the movement of twist- and hollow-bit and boundary configuration on circle edge of bone model.

During drilling process, the friction between drill bit and bone can be modeled as the shear friction with simply linear relation as

$$f_s = m \cdot k \tag{5-25}$$

where f_s is the frictional stress, k is the shear yield stress and m is the friction factor. In the finite element simulation, the friction factor is set as constant value 0.3.

Nalla,et al [130] reported that mechanistic fracture of human cortical bone was consistent with strain-controlled failure which could be taken as ductile damage. The normalized Cockroft and Latham fracture criterion is adopted to predict and determine the time and site of ductile damage initiation and propagation according to the accumulation law

$$D_f = \int_0^{\varepsilon_{\text{eff}}} (\frac{\sigma_{\max}}{\sigma_{\text{eff}}}) d\bar{\varepsilon} \tag{5-26}$$

where D_f is the damage value of the material, σ_{eff} is the effective stress, $\sigma_{\max}$ is maximum stress, ε_{eff} is effective strain of fracture and $d\bar{\varepsilon}$ is effective strain increment. Fracture factor depends on deformation and tensile stress and describes accumulated equivalent strain modified by maximum principal stress which is normalized by effective stress[131].

According to criterion(5-26), when the damage value D_f reaches the critical value, the material failure occurs which causes element deletion and separation from the object in the simulation, then chip will generate while drilling.

5.5.2.4 Experiment Setup for Drilling bone

The mechanical property of bone is dependent on its composition and geometry, as well as size and shape of the test specimens. In validation experiment, we choose porcine femur specimens for study. Since Aerssens,et al [132] reported that porcine bone best resembled human's bone on density, geometry size, and biomechanics from *in vitro* experiment. As can be seen from Table 5–3, porcine bone shows a good likeness with of human. The detail mechanical properties of human, horse, bovine, and porcine femur cortical bone are listed in Table 5–3 [126].

Table 5–3. List of mechanical property of human, equine, bovine, and porcine femur cortical bone.

	Specimens			
Mechanical Property	Human	Horse	Cattle	Pig
Ultimate tensile strength (MPa)	124	121	113	88

Ultimate extension (%)	1.41	0.75	0.88	0.68
Elastic modulus in tension (GPa)	17.6	25.5	25	14.9
Ultimate compressive strength (MPa)	170	145	147	100
Ultimate contraction (%)	1.85	2.4	1.7	1.9
Ultimate shear strength (MPa)	54	99	91	65
Elastic modulus in torsion (GPa)	3.2	16.3	16.8	13.5

Figure 5.27 shows experimental setup for surgical drilling on porcine femur. Before experiment, muscle and fat of the femurs are cleaned off, and then 12 holes are drilled on the femurs.

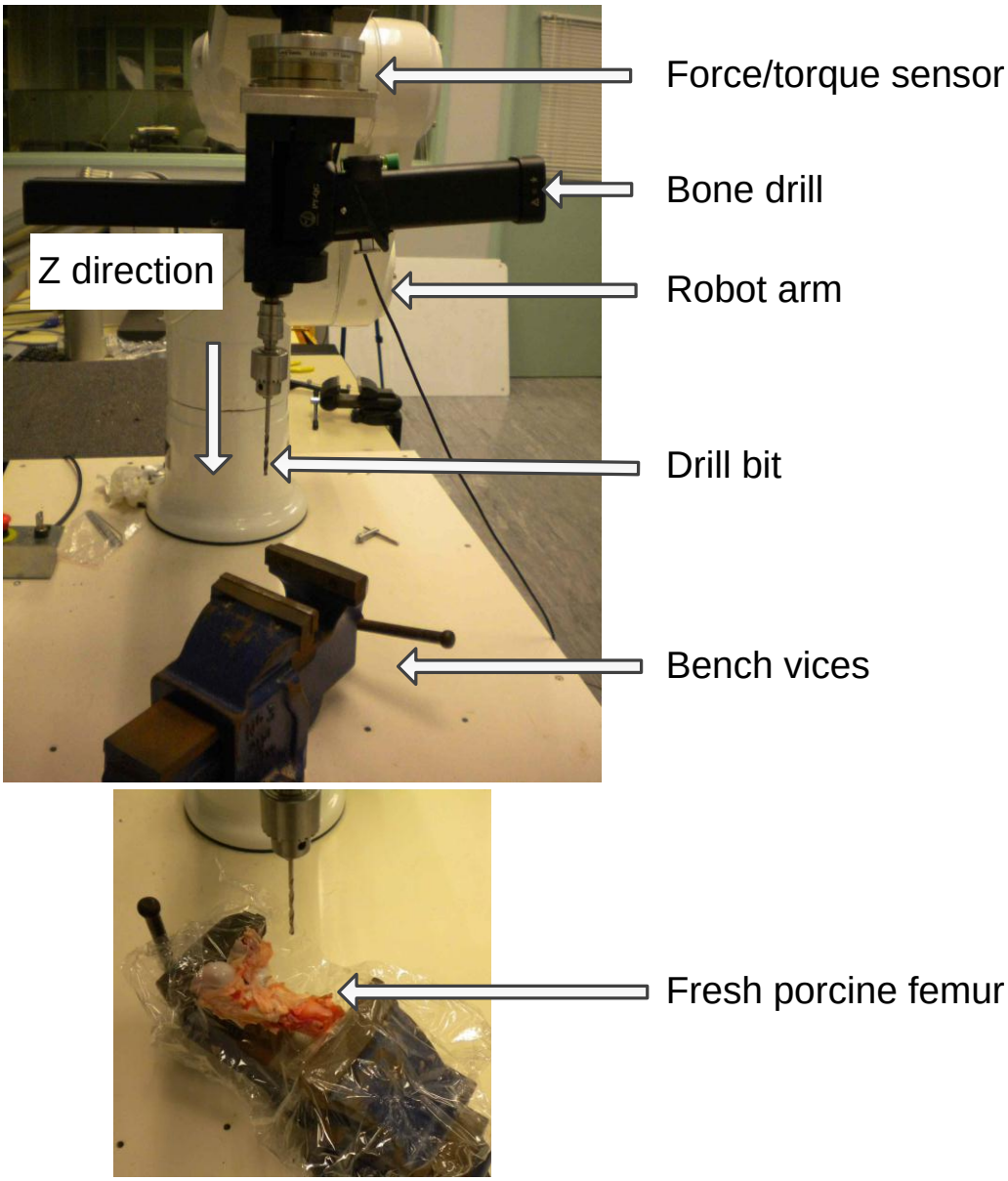

Figure 5.27. Experiment setup for drilling porcine femur.

5.5.2.5 Evaluation of results from experiment and FEA

Because it is difficult to place strain gauges either inside the drilled object or on the surface of drill bit, that is a hard task to directly measure the dynamic stress distribution through experiment.

In addition, the magnitude and dynamic variation of drilling force are the principle information during bone surgery. For finite element analysis, the drilling force is the volume integral of shear stress between drill bit and bone. The drilling force from FEA was compared with the experimental measurement.

Mean stress (or hydrostatic stress) σ_{mean}, responsible for volumetric changes, is also evaluated for the mechanical performance from FEA. The σ_{mean} indicates negative value of the compressive stress and positive value of tensile stress.

5.5.3 Results and Discussion

5.5.3.1 Simulation with Rigid-Plastic Bone Model

When bone is set as rigid-plastic material, the number of tetrahedral elements on bone model after mesh generation is 273,374.

Figure 5.28 shows the three-dimensional twist-bit tip drilling result while penetrating into the bone model. The chip generation is shown in Figure 5.28 (a). Because the twist bit drilling is equivalent to orthogonal cutting, the main stress distribution is inside and around drilled hole. From Figure 5.25 (b), the largest stress distributes on the contact surface between drill-bit tip and bone.

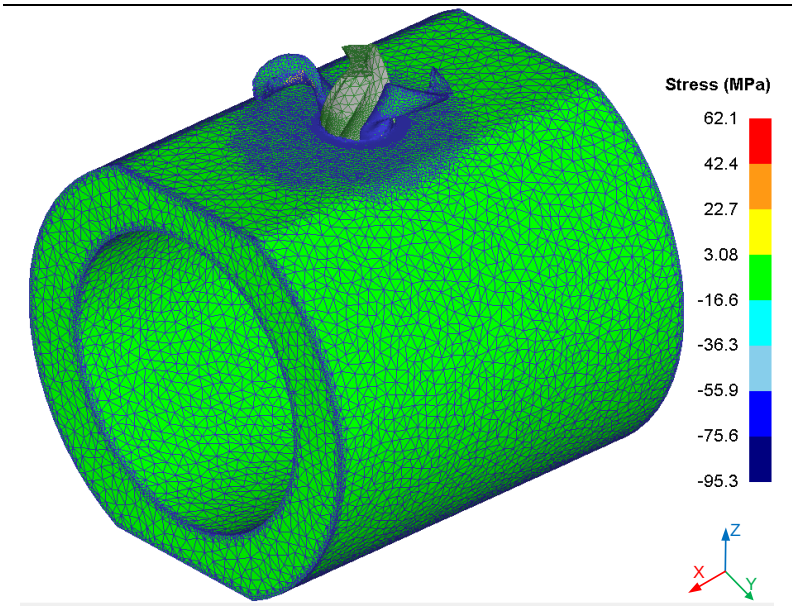

(a) Chip generation of drilling in simulation

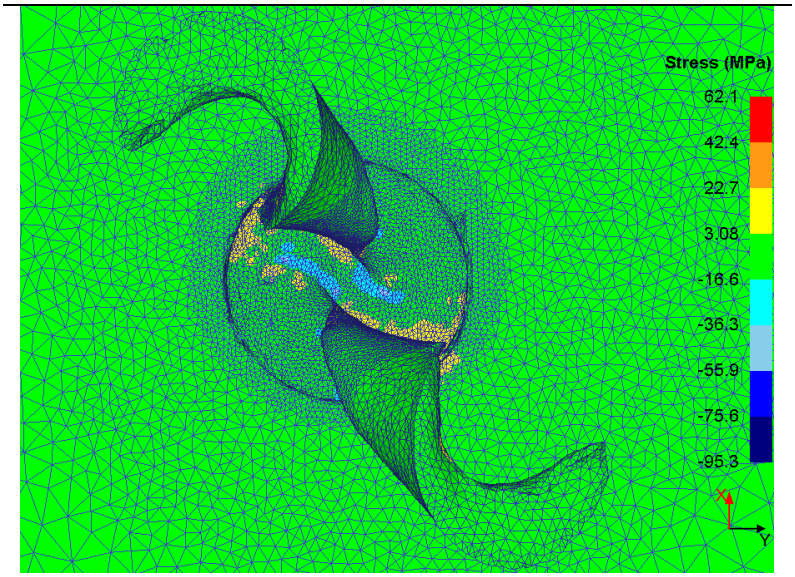

(b) Stress distribution inside and around the drilled hole from the top view, negative value on the color bar indicates compressive stress and positive value indicates tensile stress.

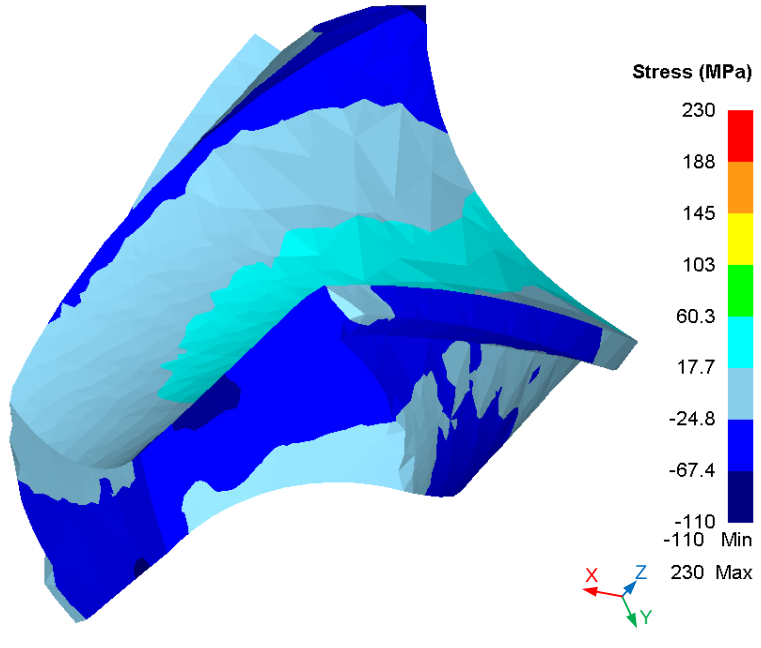

(c) Stress distribution on twist-bit tip

Figure 5.28. Chip generation and stress distribution of twist-bit tip drilling simulation from FEA. The feed rate is 12.5 mm/s and rotation speed is 600 rpm.

The stress distribution (shown in Figure 5.28) is the mean stress (or hydrostatic stress) σ_{mean} defined as

$$\sigma_{\text{mean}} = \frac{1}{3}(\sigma_x + \sigma_y + \sigma_z) \tag{5-27}$$

which is responsible for volumetric changes. The negative value of σ_{mean} indicates the compressive stress and positive value indicates tensile stress.

In Figure 5.28 (c), the main stress of the twist-bit tip distributes on the cutting lip and chisel edge with range from -110 to 230 MPa.

Figure 5.29 and Figure 5.30 (a) illustrate the recorded drilling force on twist-bit tip *in vitro* experiment, while Figure 5.29 and Figure 5.30 (b) show force on the twist-bit tip from FEA result under feed rate 12.5 mm/s and 1.25 mm/s with rotation speed 600 rpm. The FEA result shows the load increased while contact and penetration and decreased while break-through. The maximum experimental drilling force on twist-bit tip is 220 ± 30N, while maximum forces of FEA are 150 to 170 N with 12.5 mm/s feed rate. The maximum experimental drilling force by twist-bit tip is 20 ± 5N, while maximum forces of FEA are 15 to 20 N with 1.25 mm/s feed rate. The fluctuations on force profile of FEA results are caused by remeshing and interpolation by finite element solver.

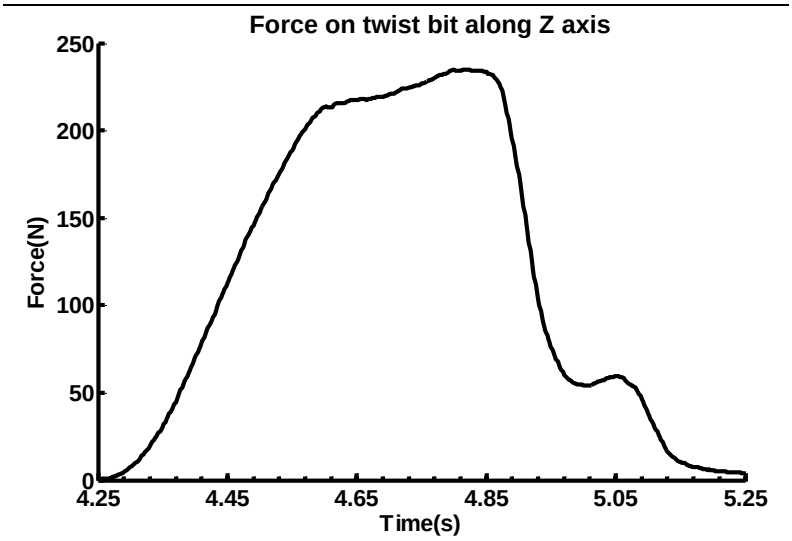

(a) Recorded drilling force data on twist bit along Z axis in experiment (enlarged time axis).

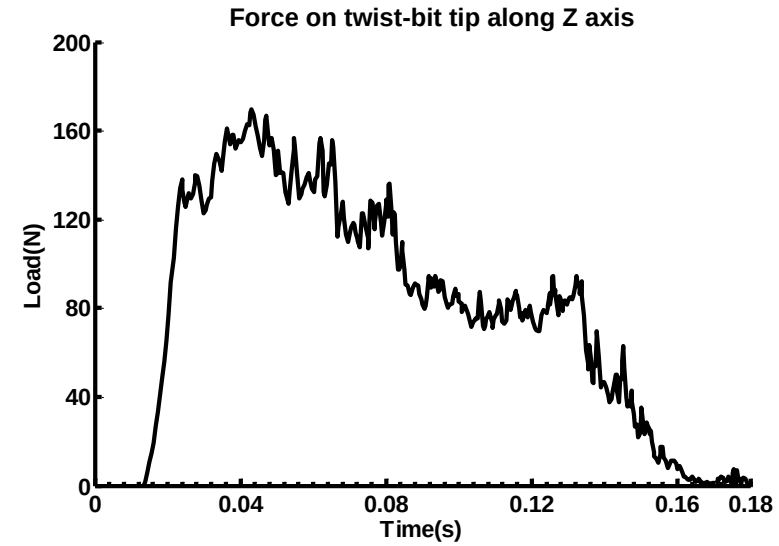

(b) Drilling force on twist-bit tip along Z axis from FEA

Figure 5.29. Comparison of recorded drilling force and FEA result with feed rate = 12.5 mm/s, rotation speed = 600 rpm.

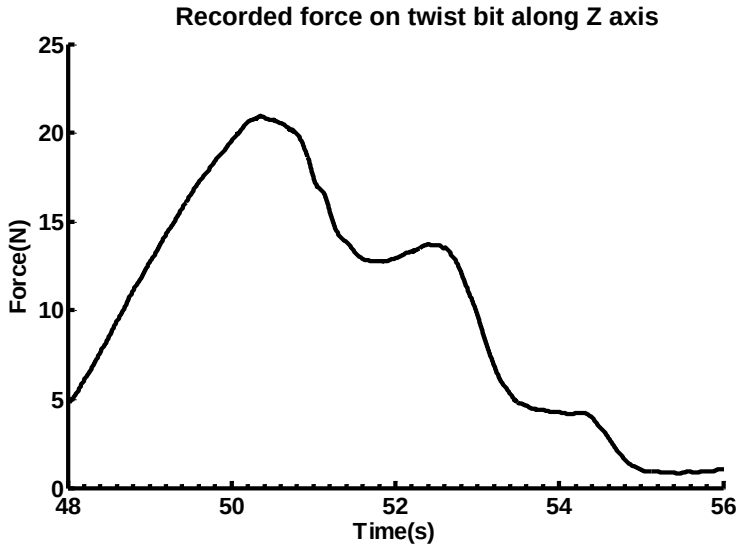

(a) Recorded drilling force data on twist bit along Z axis in experiment (enlarged time axis).

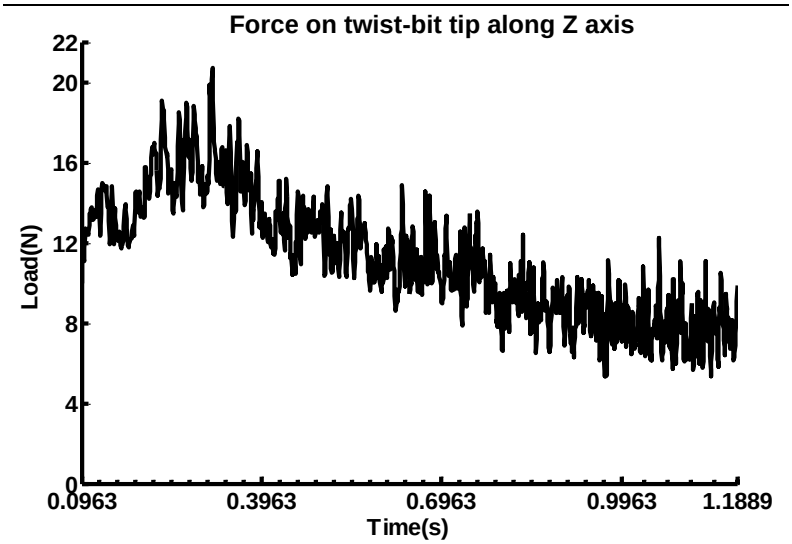

(b) Drilling force on twist-bit tip along Z axis from FEA

Figure 5.30. Comparison of recorded drilling force and FEA result with feed rate = 1.25 mm/s, rotation speed = 600 rpm.

Figure 5.31 shows three-dimensional hollow-bit tip drilling while penetrating into the bone model. The chip generation is shown in Figure 5.31 (a). Because the hollow-bit tip drilling process consists of cutting, milling and punching operation, the main stress distributes not only inside the drilled hole but on the surface of the bone segment with a range from -2620 to 11700 MPa. The green stress on surface is tensile stress while the light blue stress is compressive stress. The differential stress distribution can cause the "*bending*" effect on the distal fixed hollow beam-like object.

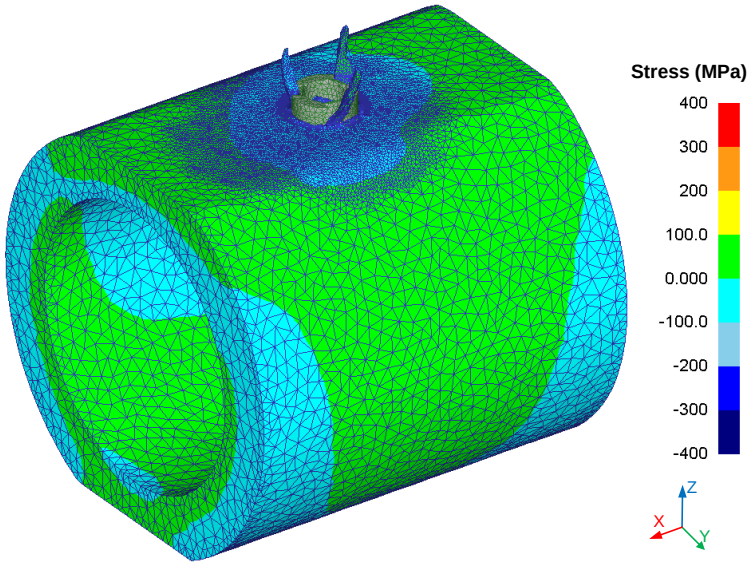

(a) Chip generation of drilling in simulation

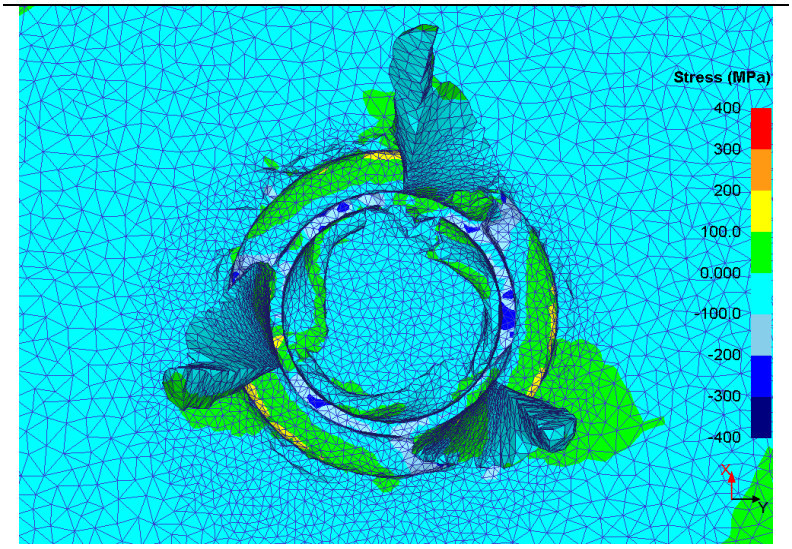

(b) Stress distribution inside and around the drilled hole from the top view, negative value on the color bar indicates compressive stress and positive value indicates tensile stress.

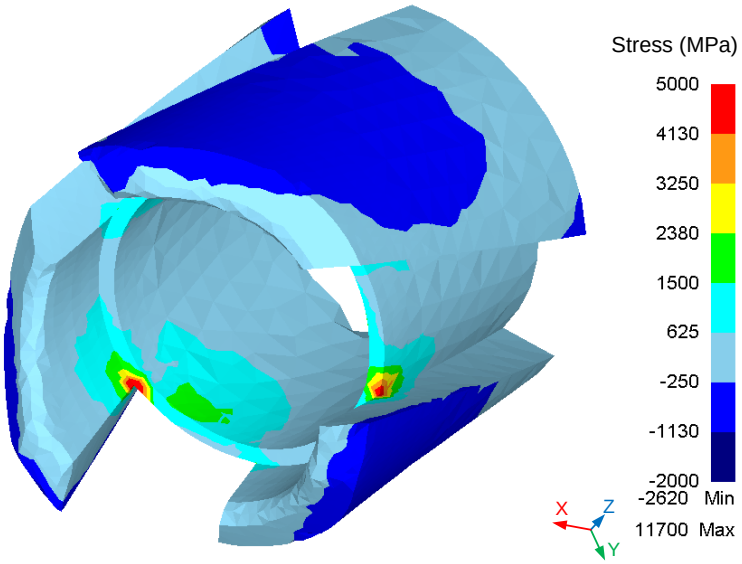

(c) Stress distribution on hollow-bit tip

Figure 5.31. Chip generation and stress distribution of hollow-bit tip drilling in FEA with feed rate = 1.25 mm/s and rotation speed = 600 rpm.

Figure 5.32 (a) shows the recorded drilling force on hollow-bit tip *in vitro* experiment, while Figure 5.32 (b) shows force on the hollow-bit tip from FEA result under feed rate 12.5 mm/s with rotation speed 600 rpm. Because hollow-bit tip has much more contact area with bone, the magnitude of force profile of hollow-bit tip is much larger than of twist-bit tip. The maximum experimental drilling force by hol-

low-bit tip is 420±40N, while maximum forces of the FEA are 500 to 550 N with 12.5 mm/s feed rate.

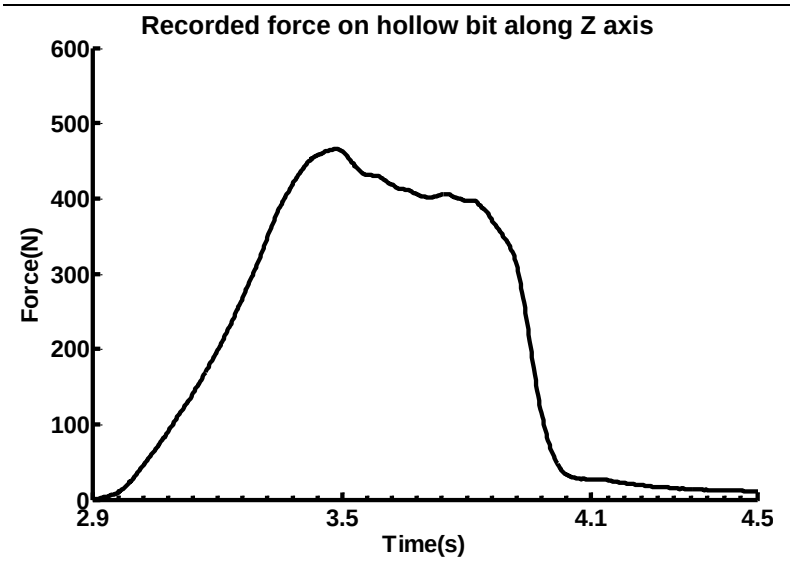

(a) Recorded drilling force data on hollow bit along Z axis in experiment (enlarged time axis).

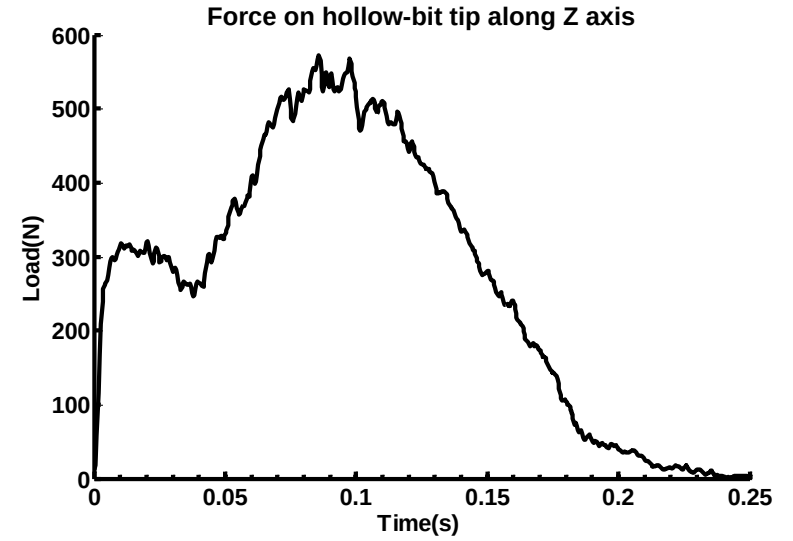

(b) Drilling force on hollow-bit tip along Z axis from FEA

Figure 5.32. Comparison of measured force and FEA result, feed rate = 12.5 mm/s, rotation speed = 600 rpm.

5.5.3.2 Simulation with Elasto-Plastic Bone Model

When the bone model is set as elasto-plastic material, the number of tetrahedral elements on bone model after mesh generation is 25,407.

Figure 5.33 shows three-dimensional twist-bit tip drilling result. The chip generation is shown in Figure 5.33 (a). From Figure 5.25 and Figure 5.33 (b), the main stress distributions are similar for two types of material.

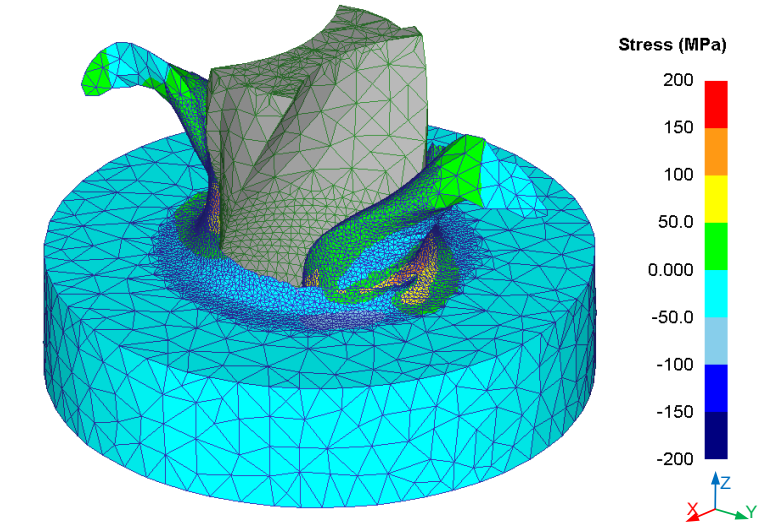

(a) Chip generation of twist-bit drilling in simulation

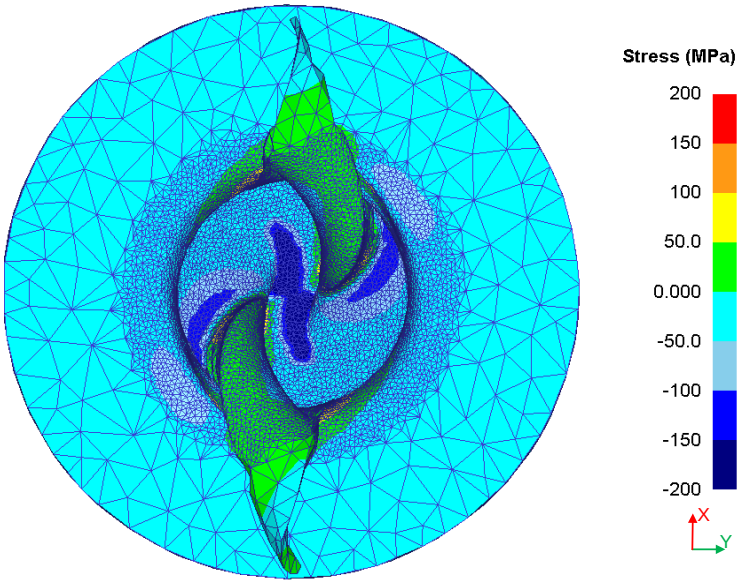

(b) Stress distribution inside and around the drilled hole from the top view, negative value on the color bar indicates compressive stress and positive value indicates tensile stress.

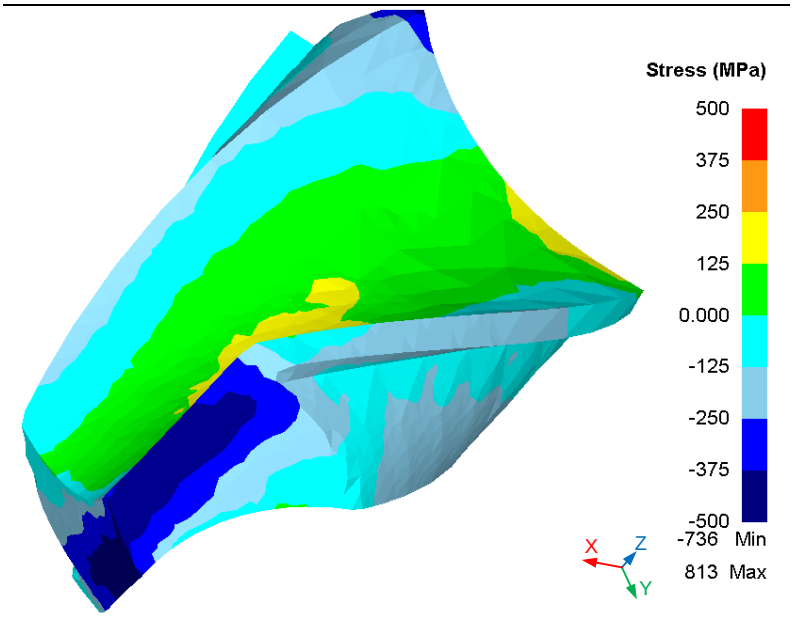

(c) Stress distribution on twist-bit tip

Figure 5.33. Chip generation and stress distribution of twist-bit tip drilling simulation from FEA with feed rate = 12.5 mm/s and rotation speed = 600 rpm.

Figure 5.34 shows force profile on the twist-bit tip from FEA result under feed rate 12.5 mm/s and rotation speed 600 rpm. In the beginning of drilling, the bone undergoes elastic deformation with smooth force curve. While the bone undergoes plastic deformation, large force fluctuations are caused by remeshing and interpolation.

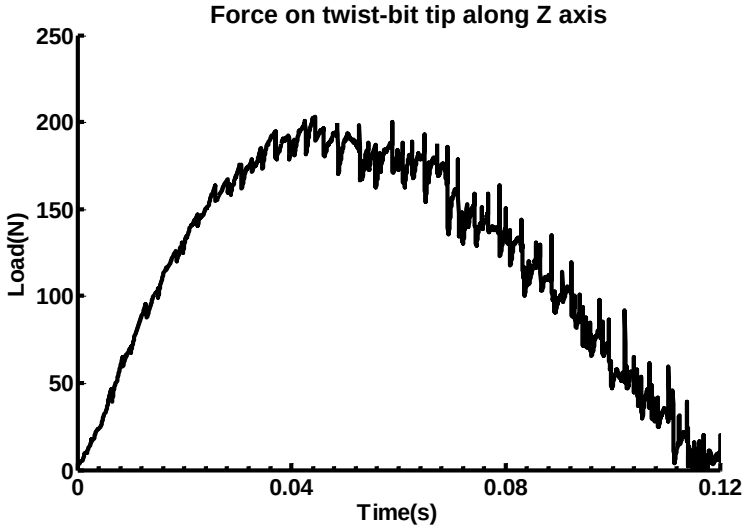

Figure 5.34. Drilling force on twist-bit tip along Z axis from FEA.

Figure 5.35 shows the three-dimensional hollow-bit tip drilling result. The chip generation is shown in Figure 5.35 (a). Figure 5.36 shows force on the hollow-bit tip from FEA result under feed rate 12.5 mm/s and rotation speed 600 rpm. For elasto-plastic model, sparse solver engine is always applied for FEM formulation to improve

solving speed and accordingly the simulation process is more sensitive to time-step. The entire simulation requires extreme long time and large memory allocation for remeshing and interpolation. Figure 5.36 shows highly frequent remeshing with small time-step while the hollow-bit penetrates more deeply into the bone model.

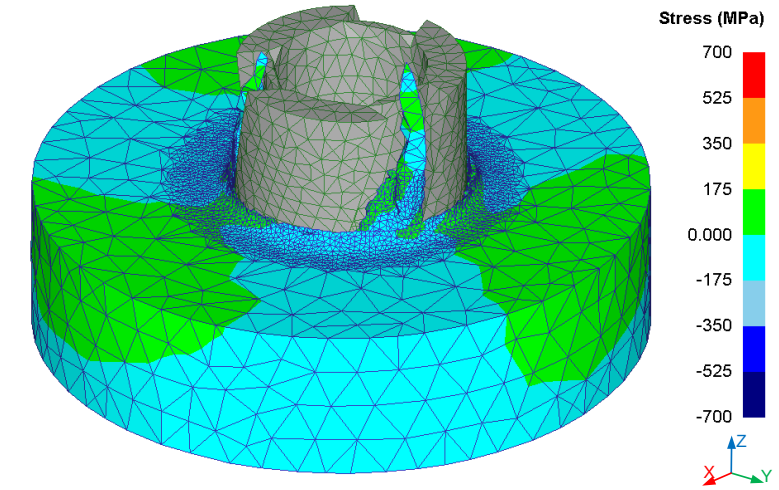

(a) Chip generation of hollow-bit drilling in simulation

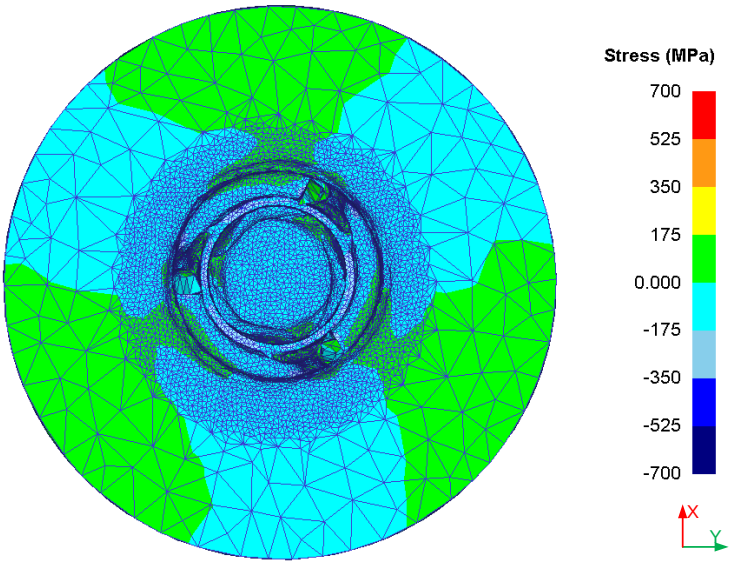

(b) Stress distribution inside and around the drilled hole from the top view, negative value on the color bar indicates compressive stress and positive value indicates tensile stress.

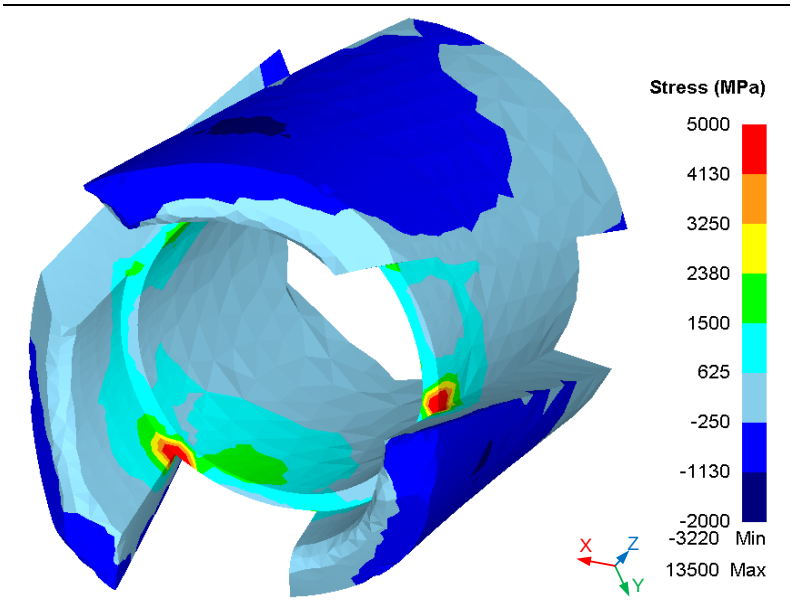

(c) Stress distribution on hollow-bit tip

Figure 5.35. Chip generation and stress distribution of hollow-bit tip drilling simulation from FEA with feed rate = 12.5 mm/s and rotation speed = 600 rpm.

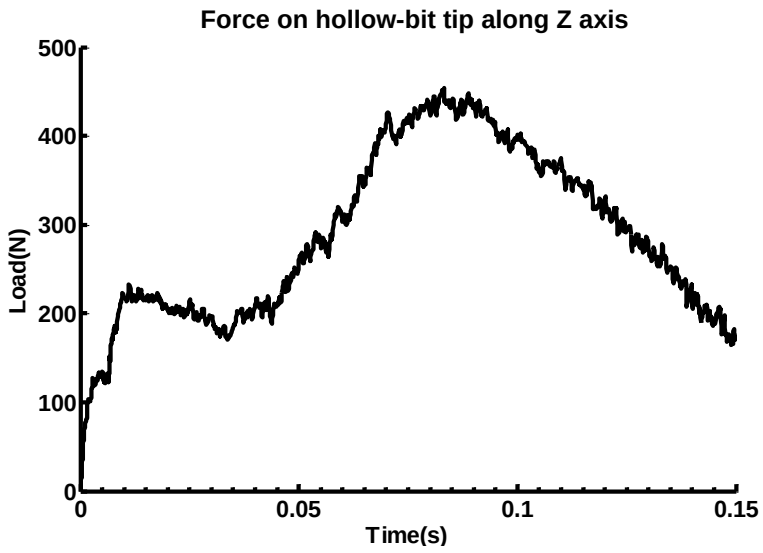

Figure 5.36. Drilling force on hollow-bit tip along Z axis from FEA.

Chapter 6. Conclusion and Future Work

In this dissertation, a robotic assisted cooperative system for orthopedic surgery is described. The robot is manipulated by surgeon manually as so-called human-robot cooperative system. The robot conducts the pre-planned surgical task with holding the surgical tool under the direct control of the surgeon. That will improve the accurate positioning due to the precise control system of the robot. Through the force amplification control, the surgeon can move the robot easily with low physical energy.

Force/torque sensor is mounted on the end-effector of robot arm to transfer the guiding force to the control system. To simulate such cooperative manipulation, control strategy based on virtual fixture for admittance control was discussed. This control strategy was designed to make robot's movement under direct manipulation by surgeon, meanwhile improving the accuracy and safety of operation. Analytical form of dynamic inverse Jacobian issue for manipulating robot was also derived for low-level control. However, this work is implemented on the haptic device. Control algorithm implementation on robotic arm for real-time application is the future work.

Force information of drilling bone is assistive for surgeon's sense. Detection algorithm of drill bit break-through femur was designed based on wavelet theory, because of complexity of bone structure, drilling force performed many disturbance which will cause fault detection only by signal processing method. However, additional sensors can be involved for more information, such as navigation system which can track the trajectory of drill bit. Multi-sensor fusion technology can be used to improve the accuracy of detection.

Finite element based simulation of drilling on femur under different surgical tools was implemented in DEFORM-3D™ software. In finite element model, material of bone is considered as plastic and elasto-plastic, the geometry of bone is simplified as hollow cylinder. Simulation gives the visual display of stress and strain distribution of the drilling process. Forces on drill bit from FEA are compared with results *in vitro* experiment to verify the FE method. The FEM provides versatile method for instrument design and process analysis as substitute of complex analytical computation.

In current work, bone is assumed as homogenous and isotropic material for modeling, besides, the thermal effect is omitted. However in practice, bone structure consists of multi-layer osseous tissue such as cortical bone and cancellous bone, the

actual stress distribution of bone varies along different directions. The micro-structure of bone performs porous property which is compressible rigid-viscoplastic.

In future work, complex model with thermal effect should be considered for simulation of the real process. This work will cost huge computation time and more experiment verification by phantom material. Phantom material, taken as the substitute of bone with similar biomechanical properties, can be machined and shaped through computer-aided manufacturing (CAM). Using phantom material will set up an ideal experiment environment for verification with FEA model. Compare with *in vitro* experiment, it will remove extra interference in the phantom test.

APPENDICES

A. Inverse Kinematics of Stäubli TX60 robot

In the last section of Chapter 3, we derive the forward kinematics of the Stäubli TX60 as

$$T_6^0 = T_1^0(\theta_1)T_2^1(\theta_2)T_3^2(\theta_3)T_4^3(\theta_4)T_5^4(\theta_5)T_6^5(\theta_6) = \begin{bmatrix} n_x & o_x & a_x & p_x \\ n_y & o_y & a_y & p_y \\ n_z & o_z & a_z & p_z \\ 0 & 0 & 0 & 1 \end{bmatrix} \quad \text{(A-1)}$$

where the entries of the matrix are

$$\begin{aligned} n_x &= c_1\left[c_{23}(c_4c_5c_6 - s_4s_6) - s_{23}s_5c_6\right] + s_1\left(s_4c_5c_6 + c_4s_6\right) \\ n_y &= s_1\left[c_{23}(c_4c_5c_6 - s_4s_6) - s_{23}s_5c_6\right] - c_1\left(s_4c_5c_6 + c_4s_6\right) \\ n_z &= -s_{23}\left(c_4c_5c_6 - s_4s_6\right) - c_{23}s_5c_6 \end{aligned} \quad \text{(A-2)}$$

$$\begin{aligned} o_x &= c_1\left[c_{23}(-c_4c_5c_6 - s_4c_6) + s_{23}s_5s_6\right] + s_1\ \ c_4c_6 - s_4c_5s_6 \\ o_y &= s_1\left[c_{23}(-c_4c_5c_6 - s_4c_6) + s_{23}s_5c_6\right] - c_1\ \ c_4c_6 - s_4c_5s_6 \\ o_z &= -s_{23}\ \ -c_4c_5s_6 - s_4c_6\ \ + c_{23}s_5s_6 \end{aligned} \quad \text{(A-4)}$$

$$\begin{aligned} a_x &= -c_1\left[c_{23}c_4s_5 + s_{23}c_5\right] - s_1s_4s_5 \\ a_y &= -s_1\left[c_{23}c_4s_5 + s_{23}c_5\right] + c_1s_4s_5 \\ a_z &= s_{23}c_4s_5 - c_{23}c_5 \end{aligned} \quad \text{(A-5)}$$

$$\begin{aligned} p_x &= a_2c_1c_2 - d_3s_1 - d_4c_1s_{23} \\ p_y &= a_2s_1c_2 + d_3c_1 - d_4s_1s_{23} \\ p_z &= -d_4c_{23} - a_2s_2 \end{aligned} \quad \text{(A-6)}$$

Thus, variable separation method is used to get

$$[T_1^0(\theta_1)]^{-1}T_6^0 = T_2^1(\theta_2)T_3^2(\theta_3)T_4^3(\theta_4)T_5^4(\theta_5)T_6^5(\theta_6)$$

Because $T_1^0(\theta_1)$ is orthogonal matrix which is $[T_1^0(\theta_1)]^{-1} = [T_1^0(\theta_1)]^T$

$$[T_1^0(\theta_1)]^{-1}T_6^0 = [T_1^0(\theta_1)]^T T_6^0 = T_6^1$$

s_{23} and c_2 are eliminated from (A-6) through $-s_1p_x + c_1p_y$ substitution, then we can get

$$-s_1p_x + c_1p_y = d_3$$

Therefore, θ_1 can be easily derived as

$$\theta_1 = atan2(\frac{p_x}{p_y}) - atan2(\pm\frac{\sqrt{p_x^2 + p_y^2 - d_3^2}}{d_3}) \tag{A-7}$$

Because $atan2(x/y) \in [-\pi, \pi]$, then θ_1 has two possible solutions.

From equation(A-6), we can get

$$p_x^2 + p_y^2 + p_z^2 = a_2^2 + d_3^2 + d_4^2 - 2a_2 \cdot d_4 \cdot s_3$$

Then θ_3 can be derived as

$$\theta_3 = sin^{-1}(K) \tag{A-8}$$

Because $sin^{-1}(x) \in [-\pi\ /\ 2, \pi\ /\ 2]$, θ_3 has two possible solutions

$$\theta_3^{'} = \pi - \theta_3 = \begin{cases} \pi - sin^{-1}(K) & if\ 1 \geq K \geq 0 \\ -(\pi + sin^{-1}(K)) & if\ -1 \leq K < 0 \end{cases} \tag{A-9}$$

where the K is

$$K = -\frac{p_x^2 + p_y^2 + p_z^2 - a_2^2 - d_3^2 - d_4^2}{2 \cdot d_4 \cdot a_2} \tag{A-10}$$

During the solving θ_1 and θ_3, there exist two conditions to determine whether the robot approaches outside of the workspace:

1) From equation(A-7), $d_3^2 - (p_x^2 + p_y^2) > 0$ has to be satisfied.

2) From equation(A-10), $\left|p_x^2 + p_y^2 + p_z^2 - a_2^2 - d_3^2 - d_4^2\right| - 2 \cdot d_4 \cdot a_2 > 0$ has to be satisfied.

Since θ_1 and θ_3 are solved, then we can get

$$\theta_{23} = atan2(\frac{(a_2 s_3 - d_4) \cdot p_z + a_2 c_3 \cdot (c_1 p_x + s_1 p_y)}{-a_2 c_3 p_z + (c_1 p_x + s_1 p_y) \cdot (a_2 s_3 - d_4)}) \tag{A-11}$$

Then $\theta_2 = \theta_{23} - \theta_3$.

Because of multiple solutions of θ_1 and θ_3, θ_2 has four possible solutions.

$$\theta_4 = atan2(\frac{-a_x c_1 c_{23} - a_y s_1 c_{23} + a_z s_{23}}{-a_x s_1 + a_y c_1}) \tag{A-12}$$

$$\theta_5 = atan2(\frac{B_1}{A_1}) \tag{A-13}$$

If $\theta_5 = 0$, the wrist singularity occurs. θ_4 can be arbitrarily chosen, and θ_6 can be chosen due to the value of θ_4, where A_1 and B_1 are

$$A_1 = -a_x(c_1c_{23}c_4 + s_1s_4) - a_y(s_1c_{23}c_4 - c_1s_4) + a_z(s_{23}c_4)$$
$$B_1 = -a_xc_1s_{23} - a_ys_1s_{23} - a_zc_{23}$$

$$\theta_6 = atan2(\frac{B_2}{A_2})$$

where A_2 and B_2 are

$$A_2 = -n_x(c_1c_{23}s_4 - s_1c_4) - n_y(s_1c_{23}s_4 + c_1c_4) + n_z(s_{23}s_4)$$
$$B_2 = n_x[(c_1c_{23}c_4 + s_1s_4)c_5 - c_1s_{23}s_5] + n_y[(s_1c_{23}c_4 - c_1s_4)c_5 - s_1s_{23}s_5] - n_z(s_{23}c_4c_5 + c_{23}s_5)$$

Considering the wrist's flip, there will be other equivalent solutions.

$$\theta_4^{'} = \theta_4 + \pi$$
$$\theta_5^{'} = -\theta_5$$
$$\theta_6^{'} = \theta_6 + \pi$$

For the real robot joint angle

$$\theta_{1r} = \theta_1,\ \theta_{2r} = \theta_2 + \frac{\pi}{2},\ \theta_{3r} = \theta_3 + \frac{\pi}{2},\ \theta_{4r} = \theta_4,\ \theta_{5r} = \theta_5,\ \theta_{6r} = \theta_6 - \pi$$

Singularity Cases through Inverse Kinematics Solution

In the regular case, the Stäubli TX60 has eight solutions for the inverse kinematics. By examining the inverse kinematics solutions of the Stäubli TX60, it can be observed that the robot has the following singularity positions:

- **Shoulder singularity**: this occurs when the intersection of joint 4, 5 and 6 lies on the Z-axis of the base frame. In this case, $d_4\sin(\theta_{2r} + \theta_{3r}) + a_2\sin(\theta_{2r}) = 0$.

  If $d_4\sin(\theta_{2r} + \theta_{3r}) + a_2\sin(\theta_{2r}) < 0$, the shoulder configuration is called *'righty'*, otherwise for $d_4\sin(\theta_{2r} + \theta_{3r}) + a_2\sin(\theta_{2r}) > 0$ called *'lefty'*.

- **Elbow singularity**: this occurs when $c_3 = 0$. If the shoulder configuration is *'righty'* and $\theta_{3r} < 0$ or if the shoulder configuration is *'lefty'* and $\theta_{3r} > 0$, the elbow configuration is called *'above'*. Otherwise, the elbow configuration is called *'below'*.

- **Wrist singularity**: this occurs when $\theta_{5r} = 0$. The wrist configuration is called *'negative'*, if $\theta_{5r} < 0$, otherwise if $\theta_{5r} \geq 0$, it is called *'positive'*.

In practice of resolving inverse kinematics, appropriate one in the eight possible solutions can be chosen according to above cases for a specific robot arm configuration. Therefore, for the TX60 robot, there are maximum eight solutions for the inverse kinematics problem.

B. Force Guidance

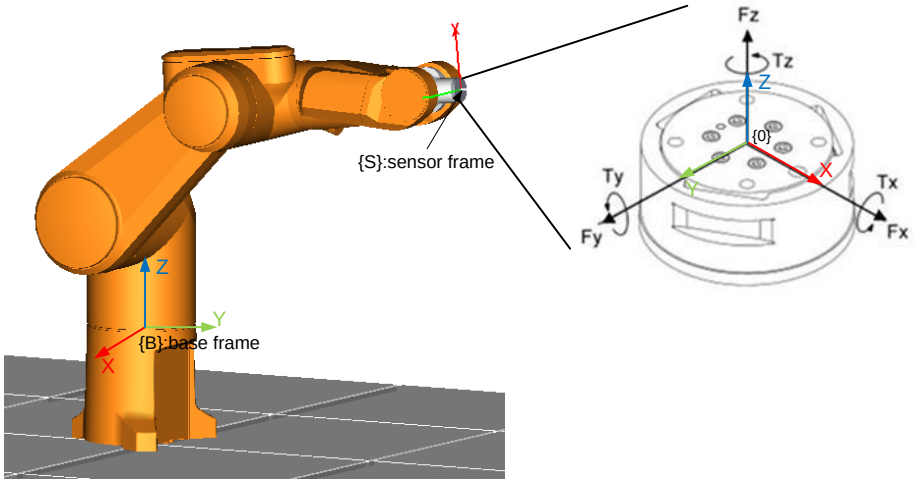

Figure B.1. Base frame of TX60 and 3-axis force and torque in sensor frame

B.1 Type 1: Force Guidance in Base Frame

$$ {}^{B}T_{S} = \begin{bmatrix} {}^{B}R_{S} & {}^{B}P_{S} \\ 0 & 1 \end{bmatrix} \tag{B-1} $$

where {S} is sensor frame, {B} is base frame.

$$ F_{B} = \begin{bmatrix} {}^{B}R_{S} & 0_{3\times3} \\ 0_{3\times3} & {}^{B}R_{S} \end{bmatrix} \cdot F_{S} \tag{B-2} $$

where $\begin{bmatrix} f_{B} \\ \tau_{B} \end{bmatrix} = \begin{bmatrix} {}^{B}R_{S} & 0_{3\times3} \\ 0_{3\times3} & {}^{B}R_{S} \end{bmatrix} \cdot \begin{bmatrix} f_{S} \\ \tau_{S} \end{bmatrix}$.

$F_{S} = [f_{S}, \tau_{S}]^{T}$: force f_{S} and torque τ_{S} directly measured in sensor frame,

$F_{B} = [f_{B}, \tau_{B}]^{T}$: F_{S} transformed in base frame

B.2 Type 2: Force Guidance in Sensor Frame

$$F_B = \begin{bmatrix} {}^B R_S & 0_{3\times3} \\ {}^B P_S \times {}^B R_S & {}^B R_S \end{bmatrix} \cdot F_S \tag{B-3}$$

$$\begin{bmatrix} f_B \\ \tau_B \end{bmatrix} = \begin{bmatrix} {}^B R_S & 0_{3\times3} \\ {}^B P_S \times {}^B R_S & {}^B R_S \end{bmatrix} \cdot \begin{bmatrix} f_S \\ \tau_S \end{bmatrix} \tag{B-4}$$

This is called Pluecker Transform, f_S will affect τ_B in the base frame.

REFERENCES

1. Medical Robotic Database. http://meroda.uni-hd.de. Accessed:[May 2009].
2. R. H. Taylor, *A perspective on medical robotics.* Proceedings of the IEEE, 2006. **94**(9): pp. 1652-1664.
3. N. Nathoo, et al., *In touch with robotics: Neurosurgery for the future.* Neurosurgery, 2005. **56**(3): pp. 421-431.
4. A. R. Lanfranco, et al., *Robotic surgery - A current perspective.* Annals of Surgery, 2004. **239**(1): pp. 14-21.
5. K.S. Leung, et al., *Robotic arm in orthopaedic trauma surgery–early clinical experience and a review.* Spinal Surgery, 2008. **1**(2): pp. 3-4.
6. T. Peters and K. Cleary, *Image-guided interventions: technology and applications*, 2008, Springer. pp. 336-337.
7. Medtech Insight, *U.S. Surgical Process Volumes 2007*.
8. N. Sugano, *Computer-assisted orthopedic surgery.* Journal of Orthopaedic Science, 2003. **8**(3): pp. 442-448.
9. E.M. Kanlić, F. Delarosa, and M. Pirela-Cruz, *Computer assisted orthopaedic surgery--CAOS.* Bosn J Basic Med Sci, 2006. **6**(1): pp. 7-13.
10. J.B. Stiehl, et al., *Navigation and MIS in orthopedic surgery*, 2006, Springer. p. Page: 4.
11. P. Kazanzides, et al., *Surgical and interventional robotics - Core concepts, technology, and design.* IEEE Robotics & Automation Magazine, 2008. **15**(2): pp. 122-130.
12. G. Fichtinger, et al., *Surgical and interventional robotics: Part II - Surgical CAD-CAM systems.* IEEE Robotics & Automation Magazine, 2008. **15**(3): pp. 94-102.
13. G. D. Hager, et al., *Surgical and Interventional Robotics: Part III Surgical Assistance Systems.* IEEE Robotics & Automation Magazine, 2008. **15**(4): pp. 84-93.
14. Y.S. Kwoh, et al., *A robot with improved absolute positioning accuracy for CT guided stereotactic brain surgery.* Biomedical Engineering, IEEE Transactions on, 1988. **35**(2): pp. 153-160.
15. B. Davies, *A review of robotics in surgery.* Proceedings of the Institution of Mechanical Engineers, Part H: Journal of Engineering in Medicine, 2000. **214**(1): pp. 129-140.
16. O. Schneider and J. Troccaz, *A six‐degree‐of‐freedom passive arm with dynamic constraints (PADyC) for cardiac surgery application: Preliminary experiments.* Computer Aided Surgery, 2001. **6**(6): pp. 340-351.
17. R. H. Taylor and D. Stoianovici, *Medical robotics in computer-integrated surgery.* IEEE Transactions on Robotics and Automation, 2003. **19**(5): pp. 765-781.
18. R.A. Beasley, *Medical Robots: Current Systems and Research Directions*. Journal of Robotics, 2012. **2012**.
19. K. Cleary and C. Nguyen, *State of the art in surgical robotics: clinical applications and technology challenges.* Computer Aided Surgery, 2001. **6**(6): pp. 312-328.
20. Trk Varma and P. Eldridge, *Use of the NeuroMate stereotactic robot in a frameless mode for functional neurosurgery*. The International Journal of Medical Robotics and Computer Assisted Surgery, 2006. **2**(2): pp. 107-113.
21. P.S. Morgan, et al. *The application accuracy of the Pathfinder neurosurgical robot*. in *International Congress Series*. 2003. Elsevier.

22. Paul Ha Taylor Rh, Mittelstadt Bd, Hanson W, Kazanzides P, Zuhars Jf, Glassmann E, Musits Bl, Bargar Wl, Williamson W, *An Image-Based Roboitc System for Hip Replacement Surgery*. Journal of the Robotics Society of Japan, 1990: pp. 111-116.
23. A. Paul, *Surgical robot in endoprosthetics. How CASPAR assists on the hip.* MMW Fortschritte der Medizin, 1999. **141**(33): p. 18.
24. P. Ritschl, F. Machacek, and R. Fuiko. *Computer assisted ligament balancing in TKR using the Galileo system*. in *Computer assisted orthopaedic surgery-Proceedings of the 3rd Annual Meeting of CAOS-International. Darmstadt: Steinkopff*. 2003.
25. M. Shoham, et al., *Bone-mounted miniature robot for surgical processes: Concept and clinical applications.* Robotics and Automation, IEEE Transactions on, 2003. **19**(5): pp. 893-901.
26. F. Shi, et al., *A hand-eye robotic model for total knee replacement surgery.* Medical Image Computing and Computer-Assisted Intervention–MICCAI 2005, 2005: pp. 122-130.
27. M. Roche, *Changing the way surgeons plan and execute minimally invasive unicompartmental knee surgery.* Orthopaedic Product News, 2006.
28. C.N. Riviere, W.T. Ang, and P.K. Khosla, *Toward active tremor canceling in handheld microsurgical instruments.* Robotics and Automation, IEEE Transactions on, 2003. **19**(5): pp. 793-800.
29. K. Yesin, et al., *Design and control of in-vivo magnetic microrobots.* Medical Image Computing and Computer-Assisted Intervention–MICCAI 2005, 2005: pp. 819-826.
30. G.T. Sung and I.S. Gill, *Robotic laparoscopic surgery: a comparison of the DA Vinci and Zeus systems.* Urology, 2001. **58**(6): p. 893.
31. S. Zangos, et al., *MR-compatible assistance system for biopsy in a high-field-strength system: initial results in patients with suspicious prostate lesions.* Radiology, 2011. **259**(3): pp. 903-910.
32. S. Ernst, *Robotic approach to catheter ablation.* Current Opinion in Cardiology, 2008. **23**(1): pp. 28-31.
33. S.D. Chang, et al., *An analysis of the accuracy of the CyberKnife: a robotic frameless stereotactic radiosurgical system.* Neurosurgery, 2003. **52**(1): pp. 140-147.
34. J.P. Rock, et al., *The evolving role of stereotactic radiosurgery and stereotactic radiation therapy for patients with spine tumors.* Journal of neuro-oncology, 2004. **69**(1): pp. 319-334.
35. R.E. Wurm, et al., *Novalis frameless image-guided noninvasive radiosurgery: initial experience.* Neurosurgery, 2008. **62**(5): p. A11.
36. H.R. Halperin, et al., *Cardiopulmonary resuscitation with a novel chest compression device in a porcine model of cardiac arrest: improved hemodynamics and mechanisms.* Journal of the American College of Cardiology, 2004. **44**(11): pp. 2214-2220.
37. S. Fisher, *Use of Autoambulator for Mobility Improve ment in Patients With Central Nervous System (CNS) Injury or Disease.* Neurorehabilitation and Neural Re pair, 2008. **22**: p. 556.
38. K. Suzuki, et al. *Intention-based walking support for paraplegia patient*. in *Systems, Man and Cybernetics, 2005 IEEE International Conference on*. 2005. IEEE.

39. C. Plaskos, et al., *Praxiteles: a miniature bone - mounted robot for minimal access total knee arthroplasty.* The International Journal of Medical Robotics and Computer Assisted Surgery, 2005. **1**(4): pp. 67-79.
40. P. Maillet, et al. *BRIGIT, a Robotized Tool Guide for Orthopedic Surgery*. in *Proceedings of the IEEE International Conference on Robotics and Automation.* 2005.
41. W.L. Bargar, A. Bauer, and M. Börner, *Primary and revision total hip replacement using the Robodoc (R) system.* Clinical Orthopaedics and Related Research, 1998. **354**: p. 82.
42. A.P. Schulz, et al., *Results of total hip replacement using the Robodoc surgical assistant system: clinical outcome and evaluation of complications for 97 processes.* The International Journal of Medical Robotics and Computer Assisted Surgery, 2007. **3**(4): pp. 301-306.
43. R. H. Taylor, et al., *An Image-Directed Robotic System for Precise Orthopedic-Surgery.* Ieee Transactions on Robotics and Automation, 1994. **10**(3): pp. 261-275.
44. P. Kazanzides. *Robot Assisted Surgery: The ROBODOC® Experience*. in *INTERNATIONAL SYMPOSIUM ON ROBOTICS*. 1999. unknown.
45. R.D. Howe and Y. Matsuoka, *Robotics for surgery.* Annual Review of Biomedical Engineering, 1999. **1**(1): pp. 211-240.
46. J. Petermann, et al., *Computer-assisted planning and robot-assisted surgery in anterior cruciate ligament reconstruction.* Operative techniques in Orthopaedics, 2000. **10**(1): pp. 50-55.
47. J. Perrier, *Computer and Robotic ACL Replacement with Caspar System.* Presentation at the 1st Summer School in Surgical Robotics, Montpellier, 2003.
48. J.H. Chung, et al., *Robot-assisted femoral stem implantation using an intramedulla gauge.* Robotics and Automation, IEEE Transactions on, 2003. **19**(5): pp. 885-892.
49. B. Davies. *Synergistic robots in surgery-surgeons and robots working cooperatively*. 1998. Springer-Verlag, London Ltd.
50. F. R. Y. Baena and B. Davies, *Robotic surgery: from autonomous systems to intelligent tools.* Robotica, 2010. **28**: pp. 163-170.
51. A.D. Pearle, et al., *Perioperative management of unicompartmental knee arthroplasty using the MAKO robotic arm system (MAKOplasty).* Am J Orthop (Belle Mead NJ), 2009. **38**: pp. 16-19.
52. B. Hagag, et al., *RIO: Robotic-Arm Interactive Orthopedic System MAKOplasty: User Interactive Haptic Orthopedic Robotics.* Surgical Robotics: Systems Applications and Visions, 2010: p. 219.
53. Trk Varma, et al., *Use of the NeuroMate stereotactic robot in a frameless mode for movement disorder surgery.* Stereotactic and functional neurosurgery, 2003. **80**(1-4): pp. 132-135.
54. T. Xia, et al., *An integrated system for planning, navigation and robotic assistance for skull base surgery.* The International Journal of Medical Robotics and Computer Assisted Surgery, 2008. **4**(4): pp. 321-330.
55. G. T. Sung and I. S. Gill, *Robotic laparoscopic surgery: A comparison of the da Vinci and Zeus Systems.* Urology, 2001. **58**(6): pp. 893-898.
56. J. Marescaux, et al., *Transatlantic robot-assisted telesurgery.* Nature, 2001. **413**(6854): pp. 379-380.
57. D. Holt, et al., *Telesurgery: Advances and Trends.* University of Toronto Medical Journal, 2004. **82**(1): pp. 52-55.

58. *"OPERATION LINDBERGH" A World First in TeleSurgery: The Surgical Act Crosses the Atlantic!* , in *New York -Strasbourg Press Conference* September 2001: Espace Multimedia, Paris France.
59. Jacob Rosen, *Surgical robotics: systems, applications, and visions*, 2011, Springer Science& Business Media. p. 26.
60. G.S. Guthart and J.K. Salisbury Jr. *The Intuitive™ telesurgery system: overview and application*. in *Proceedings of IEEE International Conference onRobotics and Automation*. 2000. IEEE.
61. A. Tewari, A. Srivasatava, and M. Menon, *A prospective comparison of radical retropubic and robot‐assisted prostatectomy: experience in one institution.* BJU international, 2003. **92**(3): pp. 205-210.
62. J. Rosen, B. Hannaford, and R.M. Satava, *Surgical Robotics: Systems Applications and Visions*2010: Springer.
63. C. Bolenz, et al., *Cost comparison of robotic, laparoscopic, and open radical prostatectomy for prostate cancer.* European Urology, 2010. **57**(3): p. 453.
64. H.R.H. Patel, A. Linares, and J.V. Joseph, *Robotic and laparoscopic surgery: cost and training.* Surgical Oncology, 2009. **18**(3): pp. 242-246.
65. H. Ren, et al. *A technical review on the orthopedic compliant robotic arms*. in *Information and Automation, 2009. ICIA'09. International Conference on*. 2009. IEEE.
66. F. Pertin and Jm Bonnet-Des-Tuves. *Real time robot controller abstraction layer*. in *Proceedings of the International Symposium on Robotics 2004*. 2004.
67. J.B. Stiehl, et al., *Navigation and MIS in orthopedic surgery*, 2006, Springer. pp. Pages: 2-8.
68. K. Gary, et al., *IGSTK: an open source software toolkit for image-guided surgery.* Computer, 2006. **39**(4): pp. 46-53.
69. A. Enquobahrie, et al., *The image-guided surgery toolkit IGSTK: an open source C++ software toolkit.* Journal of Digital Imaging, 2007. **20**: pp. 21-33.
70. S. Pieper, M. Halle, and R. Kikinis. *3D Slicer*. in *Biomedical Imaging: Nano to Macro, 2004. IEEE International Symposium on*. 2004. IEEE.
71. J. Tokuda, et al., *OpenIGTLink: an open network protocol for image‐guided therapy environment.* The International Journal of Medical Robotics and Computer Assisted Surgery, 2009. **5**(4): pp. 423-434.
72. D. Zhi-Jiang, et al. *A Novel Fluoroscopy-Guided Robot-Assisted Orthopaedic Surgery System*. in *IEEE International Conference on Robotics and Biomimetics, 2006.* . 2006. IEEE.
73. Omega.6. Force Dimension Corp. Accessed:[2009] Available from: http://www.forcedimension.com/omega6-overview.
74. CHAI3D. Force Dimesion Corp. Accessed:[2009] Available from: http://www.forcedimension.com/chai3d-overview.
75. J.J. Craig, *Introduction to robotics: mechanics and control*, 2005, Prentice Hall, Englewood Cliffs, NJ. pp. 65-77.
76. J.J. Craig, *Introduction to robotics: mechanics and control, 2005*, Prentice Hall, Englewood Cliffs, NJ.
77. R.H. Taylor, *Planning and execution of straight line manipulator trajectories.* Ibm Journal of Research and Development, 1979. **23**(4): pp. 424-436.
78. P. Hsu, J. Mauser, and S. Sastry, *Dynamic control of redundant manipulators.* Journal of Robotic Systems, 2007. **6**(2): pp. 133-148.

79. Rv Mayorga and Akc Wong. *A singularities avoidance approach for the optimal local path generation of redundant manipulators*. in *Proceedings IEEE International Conference on Robotics and Automation.* 1988. IEEE.
80. Samuel R Buss, *Introduction to inverse kinematics with jacobian transpose, pseudoinverse and damped least squares methods.* University of California, San Diego, Typeset manuscript, available from http://math.ucsd.edu/~sbuss/ResearchWeb, 2004.
81. Yoshihiko Nakamura, *Advanced robotics: redundancy and optimization.*1990: Addison-Wesley Longman Publishing Co., Inc.
82. L.B. Rosenberg. *Virtual fixtures: Perceptual tools for telerobotic manipulation*. in *Virtual Reality Annual International Symposium.* 1993. IEEE.
83. J. Funda, et al., *Constrained Cartesian motion control for teleoperated surgical robots.* IEEE Transactions on Robotics and Automation, 1996. **12**(3): pp. 453-465.
84. M. Li and R. H. Taylor. *Optimum robot control for 3D virtual fixture in constrained ENT surgery*. in *6th International Conference on Medical Imaging Computing and Computer-Assisted Intervention*. 2003. Montreal, Canada: Springer-Verlag Berlin.
85. A. Bettini, et al. *Vision assisted control for manipulation using virtual fixtures: Experiments at macro and micro scales*. in *19th IEEE International Conference on Robotics and Automation (ICRA)*. 2002. Washington, Dc: Ieee.
86. P. Marayong, et al. *Spatial motion constraints: Theory and demonstrations for robot guidance using virtual fixtures*. in *Proceedings of IEEE International Conference on Robotics and Automation*. 2003. IEEE.
87. Ra Cruces and J. Wahrburg, *Improving robot arm control for safe and robust haptic cooperation in orthopaedic processes.* The International Journal of Medical Robotics and Computer Assisted Surgery, 2007. **3**(4): pp. 316-322.
88. Roman A. Prokopenko. MATLAB interface to Sensable Phantom 3D haptic robot. Accessed:[2009] Available from: http://prokopenko.org/phantom.html.
89. P. Corke, *MATLAB toolboxes: robotics and vision for students and teachers.* Robotics & Automation Magazine, IEEE, 2007. **14**(4): pp. 16-17.
90. Technologies Sensable. Specifications for the PHANTOM Desktop™ haptic device. Accessed:[2009] Available from: http://www.sensable.com/haptic-phantom-desktop.htm.
91. G. Strang, *Linear Algebra and Its Applications Academic*. New York, 1976. **19802**.
92. C. H. Jacobs, et al., *A study of the bone machining process—Orthogonal cutting.* Journal of Biomechanics, 1974. **7**(2): pp. 131-136.
93. C. H. Jacob, et al., *A study of the bone machining process—Drilling.* Journal of Biomechanics, 1976. **9**(5): pp. 343-349.
94. Margareta Nordin and Victor Hirsch Frankel, *Basic biomechanics of the musculoskeletal system*, 2001, Lippincott Williams & Wilkins. pp. 25-31.
95. Femur shaft. Accessed:[2012] Available from: http://www.scoopweb.com/Periosteum.
96. B. Allotta, G. Giacalone, and L. Rinaldi, *A hand-held drilling tool for orthopedic surgery.* IEEE/ASME Transactions on Mechatronics., 1997. **2**(4): pp. 218-229.
97. F. R. Ong and K. Bouazza-Marouf, *The detection of drill bit break-through for the enhancement of safety in mechatronic assisted orthopaedic drilling.* Mechatronics, 1999. **9**(6): pp. 565-588.

98. Stäubli International Ag, *Stäubli Robotic Arm - TX series 60 family - Instruction Manual*2007: STÄUBLI INTERNATIONAL AG.
99. Stäubli International Ag, *Stäubli VAL3 REFERENCE MANUAL*2008: STÄUBLI INTERNATIONAL AG.
100. Ati Industrial Automation Inc, *Net F/T Network Force/Torque Sensor System Compilation of Manuals*August, 2010: ATI Industrial Automation Inc.
101. Pn Brett, et al., *An automatic technique for micro-drilling a stapedotomy in the flexible stapes footplate.* Proceedings of the Institution of Mechanical Engineers, Part H: Journal of Engineering in Medicine, 1995. **209**(4): pp. 255-262.
102. Valentina Colla and Benedetto Allotta. *Wavelet-based control of penetration in a mechatronic drill for orthopaedic surgery*. in *Robotics and Automation, 1998. Proceedings. 1998 IEEE International Conference on*. 1998. IEEE.
103. I. Daubechies, *The Wavelet Transform, Time-Frequency Localization and Signal Analysis.* IEEE Transactions on Information Theory, 1990. **36**(5): pp. 961-1005.
104. S. G. Mallat, *Multiresolution Approximations and Wavelet Orthonormal Bases of $L^2(R)$.* Transactions of the American Mathematical Society, 1989. **315**(1): pp. 69-87.
105. M Paul, *C algorithm for real-time DSP*, 1995, Prentice Hall. pp. 132-135.
106. Michel Misiti, et al., *MATLAB Wavelet Toolbox User's Guide. Version 3.* 2004.
107. S. Mallat and W. L. Hwang, *Singularity Detection and Processing with Wavelets.* IEEE Transactions on Information Theory, 1992. **38**(2): pp. 617-643.
108. S. Mallat, *Zero-Crossings of a Wavelet Transform.* Ieee Transactions on Information Theory, 1991. **37**(4): pp. 1019-1033.
109. S. Mallat and S. F. Zhong, *Wavelet Maxima Representation.* Wavelets and Applications, 1991. **20**: pp. 207-284.
110. E. Erkmen, et al., *Comparison of biomechanical behaviour of maxilla following Le Fort I osteotomy with 2- versus 4-plate fixation using 3D-FEA: Part 3: Inferior and anterior repositioning surgery.* International Journal of Oral and Maxillofacial Surgery, 2009. **38**(2): pp. 173-179.
111. M. S. Ataç, et al., *Comparison of biomechanical behaviour of maxilla following Le Fort I osteotomy with 2- versus 4-plate fixation using 3D-FEA. Part 1: Advancement surgery.* International Journal of Oral and Maxillofacial Surgery, 2008. **37**(12): pp. 1117-1124.
112. M. S. Ataç, et al., *Comparison of biomechanical behaviour of maxilla following Le Fort I osteotomy with 2- versus 4-plate fixation using 3D-FEA: Part 2: Impaction surgery.* International Journal of Oral and Maxillofacial Surgery, 2009. **38**(1): pp. 58-63.
113. P. C. Chang, N. P. Lang, and W. V. Giannobile, *Evaluation of functional dynamics during osseointegration and regeneration associated with oral implants.* Clinical Oral Implants Research, 2010. **21**(1): pp. 1-12.
114. Suneel Ranga Sai Battula. Experimental and numerical evaluation of the pullout strength of self-tapping bone screws in normal and osteoporotic bone. 2007. PhD. Dissertation. University of Akron.
115. Joyce H. Keyak and Stephen A. Rossi, *Prediction of femoral fracture load using finite element models: an examination of stress- and strain-based failure theories.* Journal of Biomechanics, 2000. **33**(2): pp. 209-214.
116. J. H. Keyak, *Improved prediction of proximal femoral fracture load using nonlinear finite element models.* Medical Engineering & Physics, 2001. **23**(3): pp. 165-173.

117. Y.K. Tu, Y.Y. Hong, and Y.C. Chen, *Finite element modeling of kirschner pin and bone thermal contact during drilling.* Life Science Journal, 2009. **6**(4): pp. 23-27.
118. Z Paszenda and M Basiaga, *FEM analysis of drills used in bone surgery.* Archives of Materials Science and Engineering, 2009. **36**(2): pp. 103-109.
119. Khurshid Alam, Av Mitrofanov, and Vadim V Silberschmidt, *Finite element analysis of forces of plane cutting of cortical bone.* Computational Materials Science, 2009. **46**(3): pp. 738-743.
120. Shirō Kobayashi and Soo-Ik Oh, *Metal forming and the finite-element method*. Vol. 4. 1989: Oxford University Press on Demand.
121. O.C. Zienkiewicz and R.L. Taylor, *The Finite Element Method for Solid and Structural Mechanics*, 2005, Elsevier Butterworth-Heinemann. pp. 9-15.
122. *DEFORM-3D User's Manual, Version 6.1*, 2008: Scientific Forming Technologies Corporation, Columbus,OH.
123. Ae Melnis and Iv Knets, *Effect of the rate of deformation on the mechanical properties of compact bone tissue.* Mechanics of Composite Materials, 1982. **18**(3): pp. 358-363.
124. A Borzacchiello, et al., *Comparison between the polymerization behavior of a new bone cement and a commercial one: modeling and in vitro analysis.* Journal of Materials Science: Materials in Medicine, 1998. **9**(12): pp. 835-838.
125. Human Compact Bone, Haversian System. 2012 Accessed:[2012] Available from: http://www.matweb.com/search/datasheet.aspx?MatGUID=2a359e5beadb43d48c1cc3fdf04ba865.
126. Yuehuei H An and Robert A Draughn, *Mechanical testing of bone and the bone-implant interface*, 2000, CRC Press. pp. 68-70.
127. V Mann, et al., *The influence of mechanical stimulation on osteocyte apoptosis and bone viability in human trabecular bone.* Journal of musculoskeletal & neuronal interactions, 2006. **6**(4): p. 408.
128. B. Von Rechenberg, et al., *The use of photooxidized, mushroom-structured osteochondral grafts for cartilage resurfacing – a comparison to photooxidized cylindrical grafts in an experimental study in sheep.* Osteoarthritis and Cartilage, 2004. **12**(3): pp. 201-216.
129. Nicky Bertollo and William Robert Walsh, *Drilling of Bone: Practicality, Limitations and Complications Associated with Surgical Drill-Bits.* Biomech Appl, 2011.
130. R. K. Nalla, J. H. Kinney, and R. O. Ritchie, *Mechanistic fracture criteria for the failure of human cortical bone.* Nat Mater, 2003. **2**(3): pp. 164-168.
131. T. Wierzbicki, et al., *Calibration and evaluation of seven fracture models.* International Journal of Mechanical Sciences, 2005. **47**(4-5 SPEC. ISS.): pp. 719-743.
132. Jeroen Aerssens, et al., *Interspecies differences in bone composition, density, and quality: potential implications for in vivo bone research.* Endocrinology, 1998. **139**(2): pp. 663-670.